Studies on behavioral abnormalities and proinflammatory cytokine upregulation under neuroinflammation: Focus on glial cells

神経炎症下における行動異常と炎症性サイトカイン発現亢進に関する研究

―グリア細胞に焦点を当てて

Kohei Morimoto

Contents

Abbreviations

ACM	astrocyte conditioned medium
ACSF	artificial cerebrospinal fluid
AR	adrenoceptor
BBB	blood-brain barrier
CCL2	C-C motif chemokine ligand 2
CNS	central nervous system
CREB	cAMP response element binding protein
DAMP	damage-associated molecular pattern
ELISA	enzyme-linked immunosorbent assay
ERK	extracellular signal-regulated kinase
EU	endotoxin unit
GAPDH	glyceraldehyde-3-phosphate dehydrogenase
GFAP	glial fibrillary acidic protein
i.p.	intraperitoneal
IL-1ß	interleukin 1 beta
IL-6	interleukin 6
JNK	c-Jun N-terminal kinase
LPS	lipopolysaccharide
MAPK	mitogen-activated protein kinase
NF-κB	nuclear factor-kappa B
NORT	novel object recognition test
OLRT	object location recognition test
PBS	phosphate-buffered saline
PC	principal component
PFA	paraformaldehyde
PKA	protein kinase A
PKC	protein kinase C
RT	room temperature
STAT3	signal transducer and activator of transcription 3
TLR4	toll-like receptor 4
TNF-α	tumor necrosis factor-α

Notes

Contents of the thesis were partially published in the following article list.

List of published articles

Chapter I

1. Morimoto K., Watanuki S., Eguchi R., Kitano T., and Otsuguro K. (2023). Short-term memory impairment following recovery from systemic inflammation induced by lipopolysaccharide in mice. *Frontiers in Neuroscience,* **17**: 1273039.

Chapter II

2. Morimoto K., Kitano T., Eguchi R., and Otsuguro K. (2020). Bidirectional modulation of TNF-α transcription via α- and ß-adrenoceptors in cultured astrocytes from rat spinal cord. *Biochemical and Biophysical Research Communications,* **528**: 78–84.

3. Morimoto K., Eguchi R., Kitano T., and Otsuguro K. (2021). Alpha and beta adrenoceptors activate interleukin-6 transcription through different pathways in cultured astrocytes from rat spinal cord. *Cytokine,* **142**: 155497.

4. Morimoto K., Ouchi M., Kitano T., Eguchi R., and Otsuguro K. (2022). Dopamine regulates astrocytic IL-6 expression and process formation via dopamine receptors and adrenoceptors. *European Journal of Pharmacology,* **928**: 175110.

Preface

Mental disorders have become a major public health burden in many countries and are estimated to cause a loss of US $16 trillion over 20 years in the global economy (Patel *et al.*, 2018). The monoamine hypothesis has been considered to be an underlying mechanism of mental disorders for more than half a century (Hirschfeld, 2000). The monoamine hypothesis is a theory that proposes a link between the levels of certain neurotransmitters called monoamines (including serotonin, dopamine, and noradrenaline) that control basic emotions (O'Connor *et al.*, 2014), and mental disorders, such as depression, bipolar disorder, anxiety disorder, and schizophrenia (Hindmarch, 2002; Lee *et al.*, 2010). Antidepressants and antipsychotics have been developed based on this hypothesis, but many patients are refractory to treatments targeting this regulatory mechanism, supporting the likelihood of other regulatory mechanisms such as the neuroinflammation, neuroplasticity, and neurogenesis hypotheses (O'Connor *et al.*, 2014; Boku *et al.*, 2018). However, it's important to note that each hypothesis can not completely explain the complex etiology of mental disorders, and comprehensive investigations of these different aspects are needed to understand the mechanisms underlying mental disorders.

In recent years, it has been suggested that neuroinflammation and monoamine are related to each other in terms of the etiology of mental disorders. It is becoming increasingly evident that neuroinflammation causes monoamine deficiencies: proinflammatory mediators released from activated glial cells cause neurodegeneration and/or neuronal death, leading to impaired monoamine-mediated neurotransmission (Nakamura, 2022; Jellinger, 2023). Whereas, even mild and acute neuroinflammation that does not cause neurodegeneration induces behavioral abnormalities in some mouse models (He *et al.*, 2013; Bambico *et al.*, 2015; Qu *et al.*, 2022), suggesting the existence of mechanisms that cause abnormal monoaminergic transmission without neurodegeneration. Although some studies have shown that neuroinflammation alters the expression of monoamine metabolic enzymes or transporters that lead to behavioral abnormalities (Murdaca *et al.*, 2022; Bellavite, 2023), these reports fail to explain the pathogenesis in patients who are refractory to antidepressants that are assumed to work by increasing the concentration of monoamines in the synaptic cleft.

In the present study, I focus on proinflammatory cytokine production and cell morphology in glial cells as elements linking the monoamine and neuroinflammation hypotheses in terms of the pathogenesis of mental disorders. Proinflammatory cytokines

released by glial cells act not only as immune factors, but also can directly regulate neuronal firing, like neurotransmitters and gliotransmitters (Lawrence *et al.*, 2023). Glial cell processes regulate the levels of releasing factors in the extracellular space including neurotransmitters and cytokines in a spatiotemporal manner via rapid elongation and retraction of their processes in response to stimuli (Augusto-Oliveira *et al.*, 2019; Woodburn *et al.*, 2021; Lawrence *et al.*, 2023). Furthermore, the enhanced cytokine production and changes in the process morphology of glial cells are characteristic features of neuroinflammation, and are dependent on the degree and progression of inflammation (Augusto-Oliveira *et al.*, 2019; Woodburn *et al.*, 2021; Lawrence *et al.*, 2023). Thus, proinflammatory cytokines and process morphology of glial cells may regulate the neurotransmission. However, it remains unclear how the pathological characteristics of glial cells in neuroinflammation, especially cytokine production and morphology, progress over time and how they are associated with behavioral abnormalities. Furthermore, many studies have not considered the possibility that changes in monoamine levels may affect neuroinflammation, and the mechanisms by which cytokine production and their morphology are regulated, particularly the involvement of monoamines, is also unclear.

In Chapter I, I aimed to elucidate behavioral abnormalities and the pathophysiology of neuroinflammation using the lipopolysaccharide (LPS)-injected mouse model, which is often used as a model for the neuroinflammation hypothesis. In particular, to clarify the pathophysiology following acute inflammatory responses induced by LPS, I focused on the expression of proinflammatory cytokines and morphological features in glial cells while recovering systemic symptoms. In Chapter II, the primary cultured astrocytes were used to elucidate the mechanisms by which monoamines regulate proinflammatory cytokine interleukin-6 (IL-6) expression and process formation. In particular, the receptors and intracellular mechanisms involved in their regulation were pharmacologically investigated. Elucidating these problems can lead to novel understandings of the pathophysiology of mental disorders which demonstrates the relationship between the monoamine hypothesis and the neuroinflammation hypothesis. In addition, the findings may provide a basis for the development of new therapies.

Chapter I:
Short-term memory impairment following recovery from systemic inflammation induced by lipopolysaccharide in mice

I -1 Introduction

The relationship between neuroinflammation and mental disorders has been recognized and investigated for over 30 years (Maes *et al.*, 1992; Roohi *et al.*, 2021). Clinical studies have demonstrated that patients with systemic or peripheral inflammatory diseases such as sepsis, enteritis, periodontitis, and infection are at increased risk for mental disorders such as major depressive disorder, dementia, schizophrenia, and Alzheimer's disease (Arias *et al.*, 2012; Davydow *et al.*, 2013; Choi *et al.*, 2019; Sharma *et al.*, 2021). In addition, meta-analyses have revealed that brain and blood levels of inflammatory factors are increased in patients with mental disorders (Yuan *et al.*, 2019; Dunn *et al.*, 2020).

To elucidate the pathogenesis of these debilitating diseases, several rodent models of inflammation-induced mental disorders have been developed (Nazem *et al.*, 2015; Na and Krishnamoorthy, 2021; Tamura *et al.*, 2022). Among these models, systemic administration of LPS, a bacterial toxin, is often used, and LPS-injected mice exhibit abnormalities such as depression-, anxiety-, and cognitive disorder-like behavior with neuroinflammation in some contexts (Song and Wang, 2011; Hoogland *et al.*, 2015). Acute glial cell activation with morphological changes is observed within 24 hours of LPS injection (Bowyer *et al.*, 2020), and plays a central role in neuroinflammation. Several studies reveal that microglia, the brain's resident innate immune cells, are activated by LPS, resulting in increased production of proinflammatory cytokines and enhanced phagocytosis (Fricker *et al.*, 2012; Lively and Schlichter, 2018; Jiang *et al.*, 2022). Additionally, reactive astrocytic response to LPS increases the permeability of blood-brain barrier (BBB) triggering more drastic neuroinflammation, and changes the balance between the release and uptake of neurotransmitters in tripartite synapses (Pascual *et al.*, 2012; Peng *et al.*, 2021). Activated glial cells can accelerate neurodegeneration, resulting in functional impairment via disturbed synaptic plasticity, neural connectivity, and neurotransmitter balance (Almeida *et al.*, 2020; Bennett and Viaene, 2021). Therefore, it is important to elucidate and control the pathogenesis of LPS-induced neuroinflammation, especially glial cell activation, for the treatment development.

However, these studies using the LPS model are unlikely to recapitulate the clinical pathophysiology of human patients, as most studies focus on the acute inflammatory response occurring within 24 hours of LPS injection (Yin *et al.*, 2023). This compromises clinical relevance for two reasons: the timepoint of previous studies using the LPS model is unlikely to be consistent with human disease progression; for example, clinical sepsis and peritonitis patients develop cognitive dysfunction after recovery from acute symptoms (Hernandez-Ruiz *et al.*, 2022; Li *et al.*, 2022). Secondly, the results of behavioral tests conducted within 24 hours after LPS injection could be affected by both aberrations in brain function and systemic deficits, as significant systemic symptoms can occur in these rodent models. Therefore, behavioral tests should be conducted at least a few days following LPS challenge, after recovery from systemic and acute symptoms, and the time course of neuroinflammatory conditions during the period should also be investigated.

In the present study, I conducted several behavioral tests for the purpose of elucidating behavioral abnormalities in LPS-injected mice following recovery from systemic and acute symptoms. I subsequently investigated the hippocampal CA1 region, which is associated with short-term memory, and comprehensively investigated the pathological sequalae of neurons, astrocytes, and microglia to elucidate the underlying regulatory mechanisms for the pathogenesis.

I -2 Materials and methods

2.1 Animals

Prior to initiating studies, all animal care and experimental protocols were approved by the Committee on Animal Experimentation, Faculty of Veterinary Medicine, Hokkaido University (No. 19-0079), which was awarded Accreditation Status by the Association for Assessment and Accreditation of Laboratory Animal Care International (AAALAC International). C57BL/6N mice were obtained from CLEA Japan (Tokyo, Japan). All mice were maintained at 22 ± 4°C under a 12/12 hour light/dark cycle (7 am–7 pm) with *ad libitum* food and water access. Male mice (11–14 weeks) were used for experiments.

2.2 LPS treatment

LPS (#L2630, Escherichia coli O111:B4) was purchased from Sigma-Aldrich (St. Louis, MO, USA). A stock solution (10 mg/mL) was prepared in distilled water and stored at -20°C until injection. Mice received a single-dose intraperitoneal (*i.p.*) injection of LPS (1 or 3 mg/kg body weight) in saline (10 mL/kg body weight) at 7 pm (at the end of the light cycle). Mice were used for each experiment after the recovery periods outlined for specific experiments described as on days 0–7.

2.3 Behavioral tests

All behavioral tests and measurements of body weight and water intake were conducted at 7 pm. I selected seven behavioral tests commonly used in LPS-injected mouse models to evaluate brain functions and abnormalities such as spontaneous activity, anhedonia, anxiety-, depression-like behavior, and memory (Yin *et al.*, 2023). In all behavioral tests, all apparatuses were wiped with 70% ethanol after each mouse use to prevent smell from affecting animal behavior.

- **Open field test**

Mice were placed in the center of an open field apparatus (45 cm × 45 cm × 45 cm) and allowed to explore freely for 10 minutes. All areas of the open field were recorded using a digital camera and behavioral analysis was performed automatically using the Mouse Behavioral Analysis Toolbox (MouBeAT) as described (Bello-Arroyo *et al.*, 2018). Total distance traveled was used as an evaluation of spontaneous activity, and total freezing time and time spent in the center (27 cm × 27 cm) were used as an evaluation

of anxiety-like behavior (Sestakova *et al.*, 2013).

- **Sucrose preference test**

Two drinking water bottles were placed in the home cages and made freely accessible to the mice. For a 3 day habituation period, both bottles were filled with 1% sucrose for the first day, and for the subsequent 2 days, one bottle was filled with 1% sucrose and the other with distilled water. LPS was injected after the 3 day habituation, and intakes of 1% sucrose and distilled water were measured every 24 hours. Bottle locations were switched daily to avoid intake depending on the position. The percentage of 1% sucrose intake relative to total water intake was used as an indicator of anhedonia (Liu *et al.*, 2018).

- **Y-maze test**

Mice were placed in a Y-shape apparatus consisting of three arms (length 30 cm, width 6 cm) and allowed to freely move among the three arms. Alternation scores were measured as described previously (Miedel *et al.*, 2017), using the number of total arm entries and the number of three consecutive entries into different arms. Alternation scores were evaluated automatically using MouBeAT software and considered an indicator of working memory (Kraeuter *et al.*, 2019).

- **Forced swimming test**

A 3,000 mL plastic beaker (diameter 15 cm) was filled with water (25°C, height 23 cm) to a level that prevented mice from touching the bottom. Mice were placed in the beaker for 6 minutes. Immobility time, defined as the time that the mouse's head and limbs did not move, was used as an indicator of depression-like behavior (Yankelevitch-Yahav *et al.*, 2015). Immobility time was measured visually by human scorers during the last 5 minutes of the test.

- **Elevated plus maze test**

Mice were placed in the center of an apparatus consisting of two open arms (length 30 cm, width 6 cm), a central platform (6 cm × 6 cm), and two closed arms (30 cm × 6 cm). The closed arms were enclosed by walls (height 30 cm) and located 63 cm above the floor. Mice were allowed to move freely for 10 minutes. All areas of the maze were recorded using a digital camera and behavioral analysis was performed automatically using MouBeAT. The time spent in each arm was measured, and the time spent in the

closed arm was used as an indicator of anxiety-like behavior (Sestakova *et al.*, 2013).

- **Novel object recognition test**

The novel object recognition test (NORT) consisted of three stages: habituation, training, and testing, and was conducted 5, 6, and 7 days after LPS injection. An open field (30 cm × 30 cm) with no objects in the habituation section, a field with two identical objects in the training section, and a field with one of the objects replaced by a novel object in the test section, as described previously (Leger *et al.*, 2013). Mice were allowed to move freely in these fields for 10 minutes. A T25 flask was used as the original object and a 50 mL tube was used as the novel object. Mice were tested to ensure that there was no difference in potential preference between the two objects (Figure 4A). The time that the mouse spent actively exploring each object, defined as having its nose pointed at the object, was used as the exploration time. In the test section, the time difference was determined from the time the mouse was placed in the field to the time it first explored each object (original object - novel object (s)). The exploration time and the time difference were evaluated automatically using the MouBeAT and used as an indicator of short-term memory (Chesworth *et al.*, 2018).

- **Object location recognition test**

The object location recognition test (OLRT) was identical to NORT until the training section, in which one of the objects is moved to a new location (opposite corner) instead of being replaced by a novel object in the test section. The exploration time and the time difference were evaluated automatically using the MouBeAT and used as an indicator of short-term memory (Chesworth *et al.*, 2018).

2.4 Endotoxin assay

A ToxinSensor™ Chromogenic LAL Endotoxin Assay Kit (GenScript, NJ, USA) was used to quantify endotoxin levels of the plasma and brain. Mice were anesthetized by inhalation of isoflurane (Pfizer, New York, NY, USA). Blood samples were taken from anesthetized animals by direct cardiac stick and mixed with EDTA. After perfusion with 10 mL saline, the whole brain was isolated, weighed, and homogenized in 1 mL distilled water. Blood and brain samples were centrifuged at 1,500 × g, and supernatants were used as samples. Endotoxin levels were quantified according to manufacturer's instructions. All equipment used for the experiment was endotoxin-free. Endotoxin levels were quantified as endotoxin unit (EU) in plasma volume (EU/mL) and as EU per

brain wet weight (EU/g).

2.5 Evaluation of blood-brain barrier permeability

BBB permeability was evaluated using Evans blue dye, which binds to albumin in blood, as described (Manaenko *et al.*, 2011). Evans blue (2% w/v) was injected *i.p.* (4 mL/kg body weight), and 3 hours later, mice were anesthetized by inhalation of isoflurane and perfused with 10 mL saline. Then, the whole brain was isolated, weighed, and homogenized in 100% trichloroacetic acid. The brain sample was incubated at 4°C for at least 12 hours and then centrifuged at 500 × g, and the supernatants were used for measurement of absorbance at 610 nm using a microplate reader (SH-1000; Corona Electric, Hitachinaka, Japan). Brain Evans blue amounts were calculated using a standard curve and normalized to brain wet weight (g Evans blue/g wet brain weight). Brain dry weight was measured after the wet brain was incubated at 60°C for at least 12 hours. The water content (%) was determined from the difference in the wet and dry weights divided by the wet weight.

2.6 Immunohistochemistry

Mice were anesthetized by inhalation of isoflurane and perfused with 4% paraformaldehyde (PFA) in phosphate-buffered saline (PBS). Whole brains were isolated and fixed with 4% PFA overnight at 4°C. Brains were then glued to a slicer stage (LinearSlicer Pro7, Dosaka EM, Kyoto, Japan), flooded in PBS, and cut into 50 µm coronal slices. Slices were blocked with a blocking buffer composed of 10% goat serum, 0.5% Triton X-100, and 0.05% sodium azide in PBS at room temperature (RT) for 2 hours. Slices were incubated with primary antibodies (Table 1) at 4°C for at least 12 hours, and then with Alexa Fluor 488- (#A11008, 1:500, Thermo Fisher Scientific, MA, USA) and/or 555- (#A21422, 1:500) conjugated goat anti-rabbit or mouse antibody at RT for 90 minutes. Slices were mounted onto glass slides with DAPI-Fluoromount G (SouthernBiotech, Birmingham, AL, USA). Images were captured using a laser scanning confocal microscope (LSM 700, Carl Zeiss, Oberkochen, Germany) with a 40 × lens objective. The images were comprised of 30 µm Z-stacks consisting of 31 optical slices of 1 µm thickness by maximum intensity projection. The mean intensity or areas of glial fibrillary acidic protein (GFAP), Iba-1, and CD68 were analyzed by ImageJ software (National Institutes of Health, MD, USA) and normalized to the control, which was arbitrarily set to a value of "1.0".

2.7 Staining of degenerating neurons

PathoGreen™ Histofluorescent Stain (Biotium, CA, USA) was used to detect neuronal degeneration. Experiments were performed according to manufacturer's instructions. Briefly, the brain was perfused and fixed with 4% PFA overnight at 4°C. Then, the brain was cut into 50 µm coronal slices, which were dried at 60°C for 30 minutes. Slices were incubated with 0.06% $KMnO_4$ and 1000 × PathoGreen™ stock solution at RT for 10 minutes each. After air drying, slices were incubated with xylene and mounted onto glass slides. Images were captured using a laser scanning confocal microscope with a 40 × lens objective.

2.8 Golgi-Cox staining

Golgi-Cox staining was performed as described previously, but with partial modification (Bayram-Weston *et al.*, 2016). The brain was perfused and fixed with 4% PFA overnight at 4°C, and incubated with a solution consisting of 1.04% Hg_2Cl_2, 1.04% $K_2Cr_2O_7$, and 0.83% K_2CrO_4 in distilled water at RT for 2 weeks. The brain was incubated with 25% sucrose at RT for 6 hours and subsequently cut into 100 µm coronal slices. After air drying, slices were incubated with 28% ammonia for 10 minutes. Slices were then incubated with xylene and mounted onto glass slides. Images were captured using a fluorescence microscope (BZ-9000, KEYENCE, Osaka, Japan) with a 100 × lens objective. Morphological evaluation of dendritic spines was conducted automatically using the application "Reconstruction" (https://synapseweb.clm.utexas.edu/) as described (Risher *et al.*, 2014). Five neurons were randomly selected from slices obtained from one mouse, and one dendrite > 30 µm was measured per neuron. The average of the dendritic spine values per mouse was used as an independent data point.

2.9 Evaluation of glial cell morphology

Morphological features of astrocytes and microglia were assessed using confocal Z-stack images of GFAP and Iba-1 staining. Astrocytes were analyzed using SMorph as described previously (Sethi *et al.*, 2021), and microglia were analyzed using ImageJ software as described (Young and Morrison, 2018). All glial cells in one image (approximately 60 cells) per mouse were analyzed. Principal component (PC) analysis was performed using the statistical analysis software JMP® 17 (SAS Institute, Inc., Cary, NC, USA) for astrocytic and microglial morphology using the morphological parameters (Astrocyte: number of -primary branches, -secondary branches, -tertiary branches, -quaternary branches, -terminal branches, average length of -primary branches, -

secondary branches, -tertiary branches, -quaternary branches, -terminal branches, total branch length, projected area, territory, ramification number, average branch width, maximum radius. Microglia: number of -branches, -junctions, -triple points, -quadruple points, average length of branches, maximum length of branches.).

2.10 RNA extraction and RT-qPCR analyses

Total RNA was extracted from whole hippocampi using RNAiso Plus (Takara Bio, Tokyo, Japan). To remove genomic DNA and synthesize cDNA, RNA samples were then incubated with qPCR RT Master Mix with gDNA Remover (TOYOBO, Osaka, Japan). Real-time PCR was performed using Thunderbird SYBR qPCR Mix (TOYOBO), oligonucleotides, and the cDNA reaction solution. Primer sequences are provided in Table 2. Thermal cycles were performed using an Eco Real-Time PCR System (Illumina, San Diego, CA, USA). Cycling conditions were 95 °C for 1 minute (initial denaturation), followed by 40 cycles of denaturation (95°C, 15 seconds), annealing, and extension (63°C, 30 seconds). RNAs without reverse transcription were used as negative controls to determine if DNA contamination was present, as indicated by lack of amplification by real-time PCR. Melt curve analysis confirmed that only one amplicon was produced by each reaction. The expression levels of factors relative to *glyceraldehyde-3-phosphate dehydrogenase* (*Gapdh*) were calculated using the ΔΔCq method and experimental results were normalized to the control, which was arbitrarily set to a value of "1.0".

2.11 Data and statistical analysis

All studies were designed to generate groups of equal size using randomization and blinded analysis. Data are expressed as means ± S.E.M. (n = number of independent measurements) of at least five independent experiments (biological replicates). Statistical comparisons between two groups were conducted using the unpaired Student's t-tests. For multiple comparisons, one-way ANOVAs followed by the Dunnett's test or Tukey's test were used. Post-hoc tests were performed only if F achieved $p < 0.05$ and there was no significant inhomogeneity of variance. $p < 0.05$ was considered statistically significant. All statistical analysis was performed using the statistical analysis software JMP® 17.

I -3 Results

3.1 LPS caused systemic symptoms and behavioral abnormalities 24 hours after injection

I first conducted behavioral tests in mice 24 hours after LPS injection, as reported in many previous studies. LPS injection (1 mg/kg, *i.p.*) decreased time spent in center, increased total freezing time in the open field test, and increased total immobility time in the forced swimming test (Figures 1A, B). In addition, sucrose preference decreased during the first 24 hours following LPS injection (Figure 1C), but notably, body weight and water intake decreased significantly (Figures 1D, E). Total distance traveled in the open field test, an indicator of spontaneous activity, also decreased (Figure 1A). These results were indicative that the anxiety- and depression-like behavior observed in these behavioral tests could reflect the effects of systemic symptoms.

3.2 LPS caused short-term memory impairment after recovery from systemic symptoms 7 days after injection

Next, I examined whether mice had recovered from systemic symptoms 7 days after LPS injection (3 mg/kg, *i.p.*). Body weight and water intake decreased after LPS injection, which was lowest on day 1 or 2 but recovered by day 7 (Figures 2A, B), and LPS did not affect the total distance traveled in any behavioral tests on day 7 (Figures 3B-D, 4D, 5C). These results suggested that LPS-injected mice recovered from systemic symptoms on day 7. I then conducted multiple behavioral tests on day 7. LPS did not affect the sucrose preference test, forced swimming test, open field test, or elevated plus maze test, which were conducted to evaluate anhedonia-, depression-, and anxiety-behaviors (Figures 3A-C). LPS also did not affect the results of the Y-maze test, which was conducted to evaluate working memory (Figure 3D). Next, NORT and OLRT were conducted to evaluate short-term memory. In NORT, the control group exhibited a significant increase in the percentage of exploration time of the novel object in the test section, compared with that of the original object in the training section (Figure 4B). Meanwhile, the LPS group exhibited no increase in the percentage between original and novel objects. There was also a significant difference in the percentage between the control and LPS groups in the test section. Furthermore, I measured the time difference between the first exploration of the novel object and the original object by mice in the test section. The control group explored the novel object earlier than the original object, but the LPS group hardly exhibited any difference between the time to explore each

object (Figure 4C). In OLRT, the percentage of exploration time increased for the moved object in the control group, but not in the LPS group (Figure 5A). There was no difference in object recognition time between the two groups (Figure 5B). These results suggest that short-term memory impairment was present on day 7 following LPS injection, after recovery from systemic symptoms.

3.3 LPS suppressed neuronal activity accompanied by increased hippocampal immature dendritic spines

As short-term memory impairment was detected on day 7 post-LPS, multiple pathologies were investigated. Plasma LPS level increased to 1.5 ± 0.1 EU/mL 24 hours after LPS *i.p.* injection (Figure 6A). Brain LPS levels were also significantly increased 24 hours after LPS injection. Because this finding was suggestive of BBB breakdown, I evaluated BBB permeability by measuring migration of Evans blue into the brain and measuring brain water content as an indicator of cerebral edema. Neither index changed significantly on days 0, 1, 3, or 7 post-LPS injection (Figures 6B, C), suggesting that permeability of the BBB did not change. To evaluate neuronal survival in the CA1 area of the hippocampus, which is associated with short-term memory, the density of NeuN-positive cells was quantified, and neuronal cell death was detected by PathoGreen™ staining. The densities of live and dead neurons were not changed on days 0, 1, 3, and 7 post-LPS injection (Figures 6D, E). Based on these results, the experimental conditions of LPS injection used in this study increased the amount of toxin in the blood and brain, but did not affect the BBB or neuronal survival.

Subsequently, I examined whether LPS affected CA1 neuronal activity. The density of cells positive for c-Fos, a measure of neuronal activity, was significantly decreased on day 7 (Figure 7A). The density and morphology of dendritic spines, which are composed of synapses, affect neuronal circuits and plasticity, contributing to memory and learning (Runge *et al.*, 2020). Golgi-Cox staining revealed that spine density did not change on day 7 (Figure 7B, C), but spine morphology was altered, which was characterized by elongated spines (Figure 7D). Because immature spines have an elongated morphology, spines were classified according to their morphology. The percentage of immature spines (long thin and thin) increased and the percentage of mature spines (mushroom and branched) decreased on day 7 (Figure 7E). Taken together, these findings suggest that LPS caused suppression of neuronal activity accompanied by increased immature CA1 dendritic spines on day 7.

3.4 LPS transiently activated glial cells, resulting in morphological changes

Spine density tended to decrease transiently on day 3 (Figure 7C). Because activated glial cells potentially phagocytose spines, leading to decreased spine density (Stein and Zito, 2019), I investigated glial cell activation. GFAP and Iba-1, indicators of astrocyte and microglial activation, respectively, were detected by immunostaining (Figure 8A). In astrocytes, the density of GFAP-positive cells and mean GFAP fluorescence intensity increased on day 3 and recovered to baseline levels by day 7 (Figures 8B, C). Because astrocytic activation is strongly associated with morphological changes, I evaluated process morphology with the SMorph application, and performed PC analysis of 16 parameters. The first two PCs described approximately 56% of the observed variability in the data. PC1 was increased on day 7, which significantly correlated with projected area and total branch length, and PC2 was increased on day 3, which was significantly correlated with average length of terminal branches and average branch width (Figure 9A, C). According to these parameters, process widths and lengths increased on day 3, and process number and total length increased on day 7 (Figure 9B). In microglia, like in astrocytes, the density of Iba-1-positive cells and the mean fluorescence intensity of Iba-1 increased on day 3 and recovered to baseline levels on day 7 (Figures 8D, E). I also performed PC analysis using six parameters for microglia. The first two PCs accounted for approximately 85% of the observed variability in the data. PC1 was increased on days 1 and 3, which was significantly correlated with the number of branches and junctions, and PC2 was increased on days 1 and 7, which was significantly correlated with average and maximum length of branches (Figure 10A, C). According to these parameters, the number of processes increased on day 3, and process length significantly increased on days 1–7 in microglia (Figure 10B). The soma size of microglia increased significantly on days 1 and 3, which is characteristic of activated microglia (Figure 10D).

3.5 LPS transiently increased microglial inflammatory factors and phagocytosis

Next, I measured mRNA levels in the hippocampus for several factors considered to be indicators of glial cell activation (Ikeshima-Kataoka, 2016; Jurga *et al.*, 2020; Escartin *et al.*, 2021; Guo *et al.*, 2022). For the seven factors (*Gfap*, *Aqp4*, *Thbs1*, *Maob*, *Sox9*, *Slc1a2*, and *Slc1a3*) that are indicators of reactive astrocytes, RT-qPCR analysis revealed that only *Gfap* significantly increased on day 1, and *Aqp4* non-

significantly increased on day 3 (Figure 11A). No significant differences between groups were detected for any of the astrocytic activation factors on day 7. For the six microglial M1 markers (*Aif1*, *Il1b*, *Ccl2*, *Tnf*, *Fcgr3*, and *Cd86*), there were significant increases in all the factors on day 1 and no factors significantly differed between groups on day 7 (Figure 11B). The M1 markers *Aifi*, *Fcgr3,* and *Cd86* were also significantly increased on day 3. For the five M2 markers, four factors (*Chil3/4*, *Il10*, *Ccl22*, and *Mrc1*) were significantly increased on days 1 or 3 (Figure 11C). *Mrc1* remained significantly increased on day 7. Contrastingly, *Retnla* significantly decreased on days 1, 3, and 7. These data suggest that the robust LPS-induced inflammation peaked on days 1–3 and approximately recovered to baseline levels by day 7. The decrease in dendritic spine density and glial cell inflammation were both maximal on days 1–3. I thus hypothesized that activated microglia phagocytosed the spines, and performed immunostaining for CD68, the microglia-specific phagocytic marker. CD68-positive cells did not express the astrocyte marker GFAP or the neuronal marker NeuN (Figure 12A). The mean CD68 fluorescence intensity and area of CD68 increased significantly on day 3 (Figures 12B-D). It is likely that microglia phagocytosed spines on days 1–3, resulting in an increase in immature spines on day 7.

3.6 LPS induced different inflammatory responses depending on brain region

Finally, I also examined the inflammatory responses to LPS in other brain regions, such as the dentate gyrus, perirhinal cortex, entorhinal cortex, basolateral amygdala, and paraventricular hypothalamic nucleus, which include the regions involved in short-term memory. Glial cells were activated in all regions examined on day 3 (Figure 13A). Meanwhile, CD68 fluorescence intensity was increased in the hippocampal dentate gyrus without significant changes in the other regions on day 3 (Figure 13B). c-Fos expression was decreased in the hippocampal dentate gyrus on day 7, while no difference was observed in the perirhinal cortex or entorhinal cortex (Figure 13C). Contrastingly, LPS increased c-Fos expression in the basolateral amygdala and paraventricular nucleus (Figure 13C). These results suggest that glial cell activation occurred throughout the brain, but that there were regional differences in microglial phagocytosis and neuronal activity in response to LPS challenge.

I -4 Discussion

In the present study, I identified that 7 days after LPS injection, mice with recovery of systemic symptoms exhibited short-term memory impairment in behavioral tests. Suppression of hippocampal CA1 neuronal activity and decreased synaptic strength due to immature spines likely contribute to short-term memory impairment in this context. Decreased spine density due to enhanced phagocytosis of activated microglia could be responsible for increased immature spines (Figure 14).

At the commonly used dose of 1 mg/kg LPS, the behavioral testing parameters for depression, anxiety, and anhedonia were affected in experiments conducted within 24 hours following LPS injection, consistent with previous studies (Moraes *et al.*, 2017; Yu *et al.*, 2021; Song *et al.*, 2022). However, significant systemic symptoms following LPS challenge were observed, with decreased spontaneous activity, body weight, and water intake. Therefore, it is possible that indicators of depression in previously reported behavioral tests, especially freezing and immobility time, are due in part to systemic symptoms. I also suggest that the apparent decrease in sucrose preference is due to decreased total water intake, as distilled water intake did not change.

Under acute pathological conditions evoked by LPS, the proinflammatory cytokine C-C motif chemokine ligand 2 (CCL2) secreted by blood vessel cells promotes excitatory synaptic transmission in glutamatergic neurons of the hippocampus (Duan *et al.*, 2018). α_1-Adrenoceptor (AR)-induced downregulation of membrane GluR1 is involved in LPS-induced depression-like behavior (Sekio and Seki, 2015). Unlike these acute responses, the transient decrease in spines followed by the increase in immature spines, as observed in the present study, required several days, indicating distinct pathogenesis from the acute response.

The LPS dose of 3 mg/kg used in the present study produced LPS blood levels similar to those in patients with sepsis (Casey *et al.*, 1993). At this dose of LPS, BBB permeability was not affected, and none of the mice died within 7 days following administration of this dose. Meanwhile, the BBB was disrupted in mice 18 hours after high-dose LPS injection (18 mg/kg, *i.p.*) (Kikuchi *et al.*, 2019). Further, administration of 10 mg/kg LPS *i.p.* causes 100% mortality within 72 h (Ahn *et al.*, 2017). Therefore, the LPS doses required to induce BBB disruption result in a high mortality rate in mice, while the dose used in the present study (3 mg/kg) did not cause mortality with 7 days of injection, and acute systemic effects were mild.

I evaluated the pathogenesis of the LPS inflammatory response, focusing

primarily on the hippocampus, as in this context LPS affected behaviors associated with short-term memory deficits, as identified by NORT and OLRT testing. OLRT is a primarily hippocampus-dependent test, while NORT is dependent on multiple brain regions, but is not affected by hippocampal injury or inactivation in mice (Barker and Warburton, 2011; Denninger *et al.*, 2018). Contrary to these reports, some studies have reported that NORT is affected by the hippocampus (Broadbent *et al.*, 2010; Cohen and Stackman, 2015; Cinalli *et al.*, 2020). Involvement of the hippocampus in NORT is likely to depend on the latency between the training and test sections of a study. At short latencies, only the perirhinal cortex and entorhinal cortex are involved, while for latencies > 10 minutes, the hippocampus is also involved (Cohen and Stackman, 2015). In the present study, OLRT and NORT exploration times were decreased in LPS-injected mice subjected to conditioning with long latency periods (24 hours), suggesting that the hippocampus was involved in the short-term memory impairment detected in these tests. Meanwhile, in the present study, it was not possible to identify which memory processes were impaired, for example, formation, maintenance, or recall of memory (Josselyn and Tonegawa, 2020). Changes in dendritic spine morphology and number are involved in memory formation (Basu and Lamprecht, 2018). Further mechanisms of memory impairment need to be elucidated by measuring neuronal activity before and after training and testing sections.

Seven days after LPS injection, glial cell activation had returned nearly to baseline levels, together with recovery of systemic symptoms. Meanwhile, some parameters remained altered in both astrocytes and microglia, including both the morphology and expressions of glial activation markers 7 days after LPS injection. It is thus possible that LPS subsequently caused longer-duration changes in glial cell properties. Especially, the processes of both astrocytes and microglia remained elongated 7 days after LPS injection. The processes are likely to remain longer to be more sensitive to abnormalities, serving as an alert system. This is consistent with the two-hit hypothesis in mental disorders (Cao *et al.*, 2021). When microglia are activated by inflammation in early life, the threshold for activation is lowered, pathologically increasing microglial sensitivity to stress in later life. Because the present study injected LPS into adult mice, brain pathology should be investigated over a longer period after LPS injection in future studies.

Furthermore, changes in the morphology (activation) of glial cells could be responsible for short-term memory impairment. Astrocyte process elongation interferes physically with spine maturation and expansion, impairing memory formation (Zorec *et*

al., 2015). Moreover, fine astrocyte and microglial processes cover synapses. Astrocytes affect neuronal plasticity via the uptake and release of glutamate and D-serine, while microglia release proinflammatory cytokines, such as tumor necrosis factor-α (TNF-α), IL-6, and IL-1ß, which affect neuronal excitability by modulating the activities of many classes of voltage-gated channels and receptors (Sancho *et al.*, 2021). Similar to these findings, in the present study, increased coverage of the synapse via glial process elongation could affect neuronal activity and plasticity.

The time course of decreased spine density coincided with that of increased CD68, and increased CD68 concomitant with decreased density of c-Fos positive cells occurred in the hippocampus. I thus postulate that M1-like phagocytic microglia phagocytosed the spines. Meanwhile, I have not identified whether the pathology observed in the present study is the cause of short-term memory impairment. Microglial phagocytosis of spines is involved in the pathogenesis of obesity-associated memory impairment (Cope *et al.*, 2018). There are also microglia-independent mechanisms in spine disappearance, such as astrocytic phagocytosis and spine retraction accomplished in only neurons (not involving other cells) (Stein and Zito, 2019). It is necessary to investigate whether inhibition of microglial phagocytosis prevents spine morphological abnormalities and short-term memory impairment caused by neuroinflammation.

The mechanism by which glial cells are activated by *i.p.* LPS injection remains unclear. Multiple regulatory mechanisms could be responsible for LPS-induced hippocampal gliosis. First, LPS in the blood crosses the BBB and enters the brain parenchyma, activating toll-like receptor 4 (TLR4) in glial cells (Vargas-Caraveo *et al.*, 2017). Second, damage-associated molecular patterns (DAMPs) generated by neurons in response to heat, stress, or excitotoxicity activate TLR4 in glial cells (Afridi and Suk, 2023). Third, increased blood cytokines activate vascular endothelial cells and release inflammatory factors into the brain parenchyma (Bowyer *et al.*, 2020). TLR4-deficient mice are hyporesponsive to LPS (Hoshino *et al.*, 1999). LPS injection increased brain endotoxin levels in the present study, suggesting that LPS did cross BBB. Therefore, in our system, LPS was likely to directly activate TLR4 expressed on microglia and/or astrocytes. Although LPS is not thought to pass through the intact BBB (Banks and Robinson, 2010), a conflicting study reported that LPS in fact enters the brain in physiological conditions via a lipoprotein-mediated transport mechanism (Vargas-Caraveo *et al.*, 2017). Further investigation is needed to assess the contribution of these processes.

LPS caused different responses depending on the brain region. Glial cell

activation was detected in all regions examined, but regional differences were observed in neuronal activity and phagocytotic phenotype of microglia. Notably, LPS suppressed neuronal activity only in the hippocampus. Consistent with the present study, the limbic system including the hippocampus is more susceptible to inflammation in mouse models of inflammatory diseases of peripheral organs such as colitis, gastritis, and cystitis (Sun *et al.*, 2022). Furthermore, the hippocampus is more vulnerable to stress, ischemia, trauma, and aging than other brain regions (Bartsch and Wulff, 2015). Although several hypotheses have been proposed, it is unclear that the mechanism underlying increased susceptibility to inflammation in specific brain regions (Sun *et al.*, 2022). Interestingly, there were regional differences in the microglial phagocytosis, even though morphological activation of microglia occurred in all regions examined in the present study. Elucidation of the mechanisms of these regional differences can provide novel therapeutic targets. In addition, consistent with the present study, *i.p.* LPS injection has previously been reported to increase neuronal activation in the paraventricular nucleus and amygdala (Araki *et al.*, 2016). Activation of the paraventricular nucleus increases blood corticosterone levels via corticotropin-releasing hormone, and corticosterone activates the amygdala. LPS injection increases blood corticosterone levels (Haskó *et al.*, 1995), suggesting potential involvement of these pathways. In the present study, limited types of behavioral tests were performed, and several brain regions were observed. Therefore, I cannot deny that there are no brain abnormalities other than hippocampus-dependent short-term memory impairment following recovery from systemic symptoms caused by LPS.

Finally, the elucidation of pathogenic mechanisms in rodent models is an urgent issue, with the goal of clinical application for humans to the treatment of mental disorders caused by peripheral inflammatory diseases. Furthermore, in dogs and cats, canine cognitive dysfunction syndrome is also an established condition (Mihevc and Majdič, 2019; Sordo and Gunn-Moore, 2021), and various behavioral changes resulting from peripheral- or neuro-inflammation have been reported (Piotti *et al.,* 2023). Cell types, receptors, and factors associated with the identified mechanisms can be potential therapeutic targets. The pathological evaluation following recovery from systemic and acute symptoms, which was the focus of the present study, provides novel perspectives for studies using the LPS-induced inflammation model.

I -5 Summary

The relationship between neuroinflammation and mental disorders has been recognized and investigated for over 30 years. Diseases of systemic or peripheral inflammation, such as sepsis, peritonitis, and infection, are associated with increased risk of mental disorders with neuroinflammation. To elucidate the pathogenesis, systemic administration of LPS in mice is often used. LPS-injected mice exhibit behavioral abnormalities with glial activation. However, these studies are unlikely to recapitulate the clinical pathophysiology of human patients, as most studies focus on the acute inflammatory response with systemic symptoms occurring within 24 h of LPS injection. I focus on the effects of LPS on behavioral abnormalities following recovery from systemic symptoms and investigate the mechanisms of pathogenesis. Several behavioral tests were performed in LPS-injected mice, and to assess neuroinflammation, the time course of the morphological change and expression of inflammatory factors in neurons, astrocytes, and microglia were investigated. Body weight and water intake decreased after LPS injection, which was lowest on day 1 or 2 but recovered by day 7, and LPS did not affect the total distance traveled in any behavioral tests on day 7. LPS did not affect the sucrose preference test, forced swimming test, open field test, or elevated plus maze test on day 7. Meanwhile, the time spent exploring the new/moved object in the NORT or OLRT was decreased. Furthermore, the number of c-Fos positive cells, a marker of neuronal activation, decreased in the hippocampal CA1 region on day 7. The Golgi-Cox staining showed that spine density tended to decrease transiently on day 3, and the percentage of immature spines was increased on day 7. Expressions of GFAP and Iba-1, markers of astrocytic and microglial activation respectively, were increased on day 3. The gene expression of several inflammatory factors and CD68 expression, microglial phagocytic marker, peaked on days 1-3 days and recovered to pre-injection levels on day 7. In Chapter I, I identified that mice with recovery of systemic symptoms exhibited short-term memory impairment in behavioral tests. Suppression of CA1 neuronal activity and decreased synaptic strength due to immature spines likely contribute to short-term memory impairment. Decreased spine density due to enhanced phagocytosis of activated microglia could be responsible for increased immature spines. These findings provide novel insights for studies using the LPS-induced inflammation model and that will contribute to the development of treatments for mental disorders of this etiology.

I -6 Figures and tables

Table 1. Antibodies used for immunohistochemistry.

Target protein	Dilution	Host animal	Catalog number	Supplier
NeuN	1:200	Mouse	MAB377	Sigma-Aldrich, St. Louis, MO, USA
c-Fos	1:3000	Rabbit	ab190289	abcam, Cambridge, UK
GFAP	1:200	Mouse	11051	Immuno-Viological Laboratories, Gunma, Japan
Iba-1	1:1000	Rabbit	019-19741	FUJIFILM Wako, Osaka, Japan
CD68	1:500	Rabbit	ab125212	abcam, Cambridge, UK

Table 2. Primer sequences used for RT-qPCR.

Gene name	Gene symbol	Product size (bp)	Sequence (5'->3') (upper: forward; lower: reverse)
glial fibrillary acidic protein	*Gfap*	244	CACCAAACTGGCTGATGTCTAC AACCTTTCTCTCCAAATCCACAC
aquaporin 4	*Aqp4*	228	GCTGTGATTCCAAACGAACTGATG AGAAGACATACTCATAAAGGGCACC
thrombospondin 1	*Thbs1*	160	CTGGACTTGCTGTAGGTTATGATG TAGGACTGGGTGACTTGTTTCC
monoamine oxidase B	*Maob*	143	CCAAAGAAGAAAGACTGAGGAAAC AGGGAAGTAGGTTGTGTAGCAG
SRY (sex determining region Y)-box 9	*Sox9*	117	CAAGAAAGACCACCCCGATTAC AAGATAGCATTAGGAGAGATGTGAG
solute carrier family 1 (glial high affinity glutamate transporter), member 2	*Slc1a2*	113	GGAAGAAGAACGACGAGGTGTC CTTTGTCACTGTCTGAATCTGC
solute carrier family 1 (glial high affinity glutamate transporter), member 3	*Slc1a3*	216	AGGGAAGATTGTTGAGATGGAAGA GGTAGGGTGGCAGAACTTGAGG
allograft inflammatory factor 1	*Aif1*	94	CTGCCCTGATTGGAGGTGGATG CTCTGGCTCACGACTGTTTCTTTTT
interleukin 1 beta	*Il1b*	148	AGTTGACGGACCCCAAAAGA CAGCTTCTCCACAGCCACAA
C-C motif chemokine ligand 2	*Ccl2*	169	CTCTCTCTTCCTCCACCACCAT CTCTCCAGCCTACTCATTGGGA
tumor necrosis factor	*Tnf*	146	CCCCTTTACTCTGACCCCTTTATTG ACTGTCCCAGCATCTTGTGTTTC
Fc receptor, IgG, low affinity III	*Fcgr3*	184	ATTTCTCTATCCCAAAAGCCAACCA GCAAACAGGAGGCACATCACTA
CD86 antigen	*CD86*	240	GAGGAAGAAAGAGGAGCAAGCAG TTGTAAATGGGCACGGCAGATA
chitinase-like 3/4	*Chil3/4*	192	CTGAATGAAGGAGCCACTGAG GTGACAGAAAGAACCACTGAAG
interleukin 10	*Il10*	175	GTGAAAATAAGAGCAAGGCAGTGG GTCCAGCAGACTCAATACACAC
C-C motif chemokine ligand 22	*Ccl22*	173	GTCTTTTACTTTCTCTGCCCCAC ACTCTCCAGTTCGTCTATTTGGC
mannose receptor, C type 1	*Mrc1*	144	CTGACTGTGTAGTTGTGATTGGTG CATCTTTTGGAGTAGTGGTTGGAG
resistin like alpha	*Retnla*	211	CGTGGAGAATAAGGTCAAGGAAC AACGAGTAAGCACAGGCAGTTG
glyceraldehyde-3-phosphate dehydrogenase	*Gapdh*	74	GCAAGAGAGAGGCCCTCAG TGTGAGGGAGATGCTCAGTG

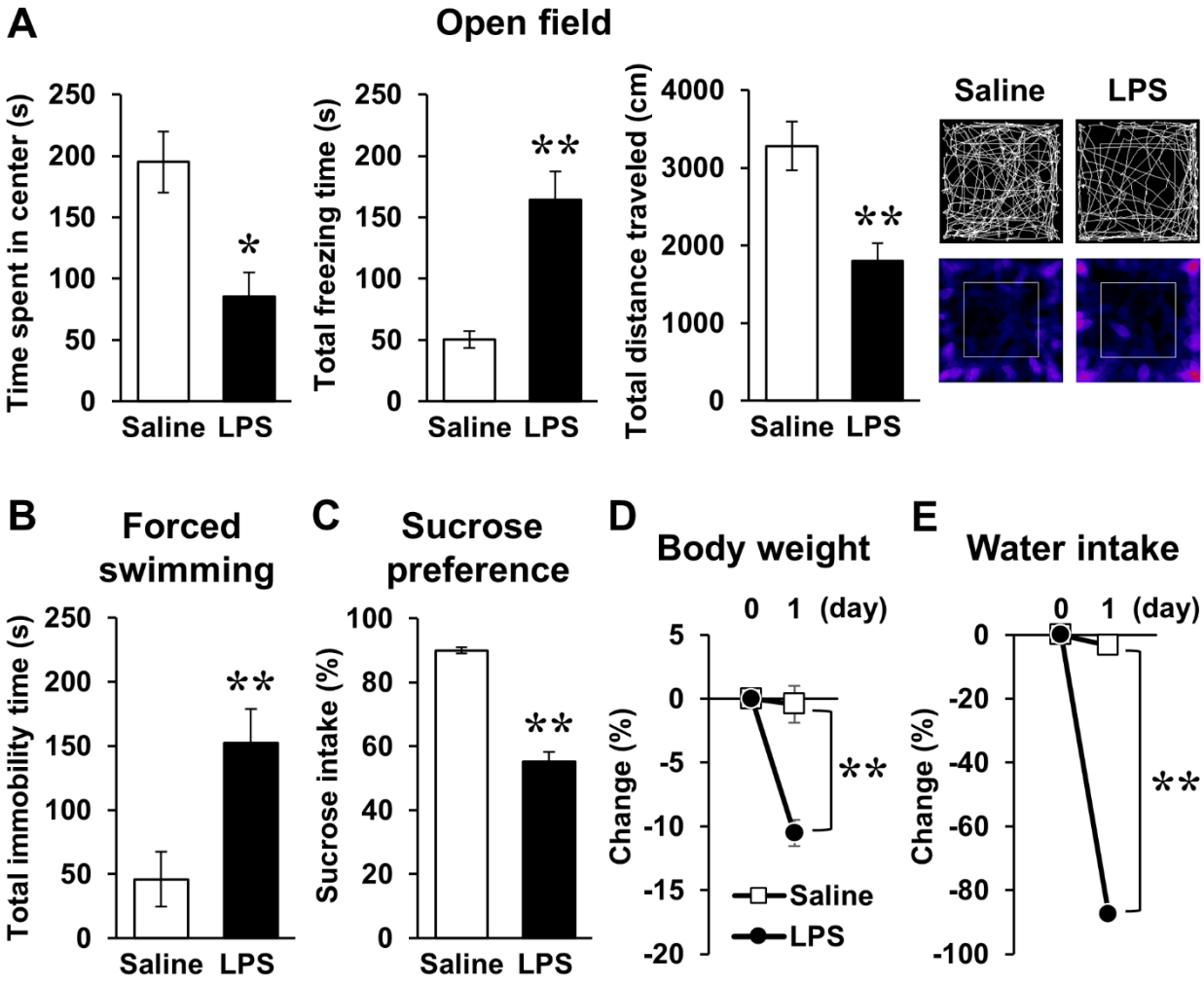

Figure 1. Systemic mouse symptoms and behavioral abnormalities 24 hours following LPS injection.

(A) Time spent in center (s), total freezing time (s), total distance traveled (cm), and representative image of mouse trace and heat map in open field test (10 min) with mice 24 hours following LPS injection (1 mg/kg, *i.p.,* single dose). n = 5 mice/group. (B) Total immobility time (s) in forced swimming test (5 min) in mice 24 hours after LPS injection. n = 5 mice/group. (C) Ratio of sucrose intake (%) over 24 hours following LPS injection in sucrose preference test. n = 6 mice/group. (D, E) Change ratio (%) of body weight (D) and water intake (E) in mice 24 hours after LPS injection. n = 6 mice/group. *$p < 0.05$, **$p < 0.01$ (unpaired Student's t-test). All data are expressed as means ± S.E.M.

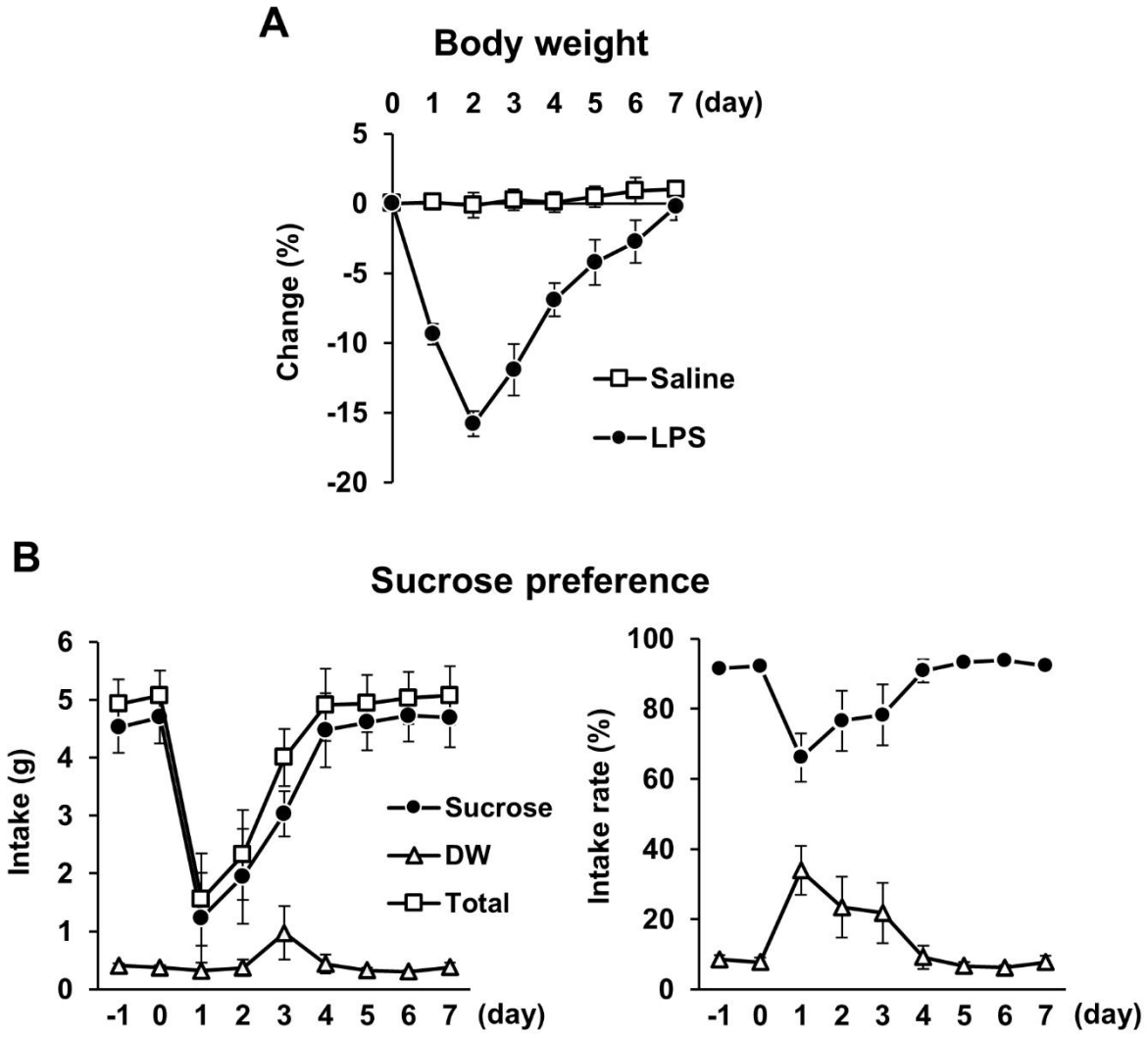

Figure 2. Body weight and water intake levels 7 days after LPS injection.

(A) Change ratio (%) of body weight 0–7 days after LPS injection (3 mg/kg, *i.p.*, single dose). n = 8 mice/group. (B) Weight (g, left) and ratio (%, right) of sucrose intake or distilled water every 24 hours with mice -1–7 days after LPS injection in sucrose preference test. n = 5 mice/group. All data are expressed as means ± S.E.M.

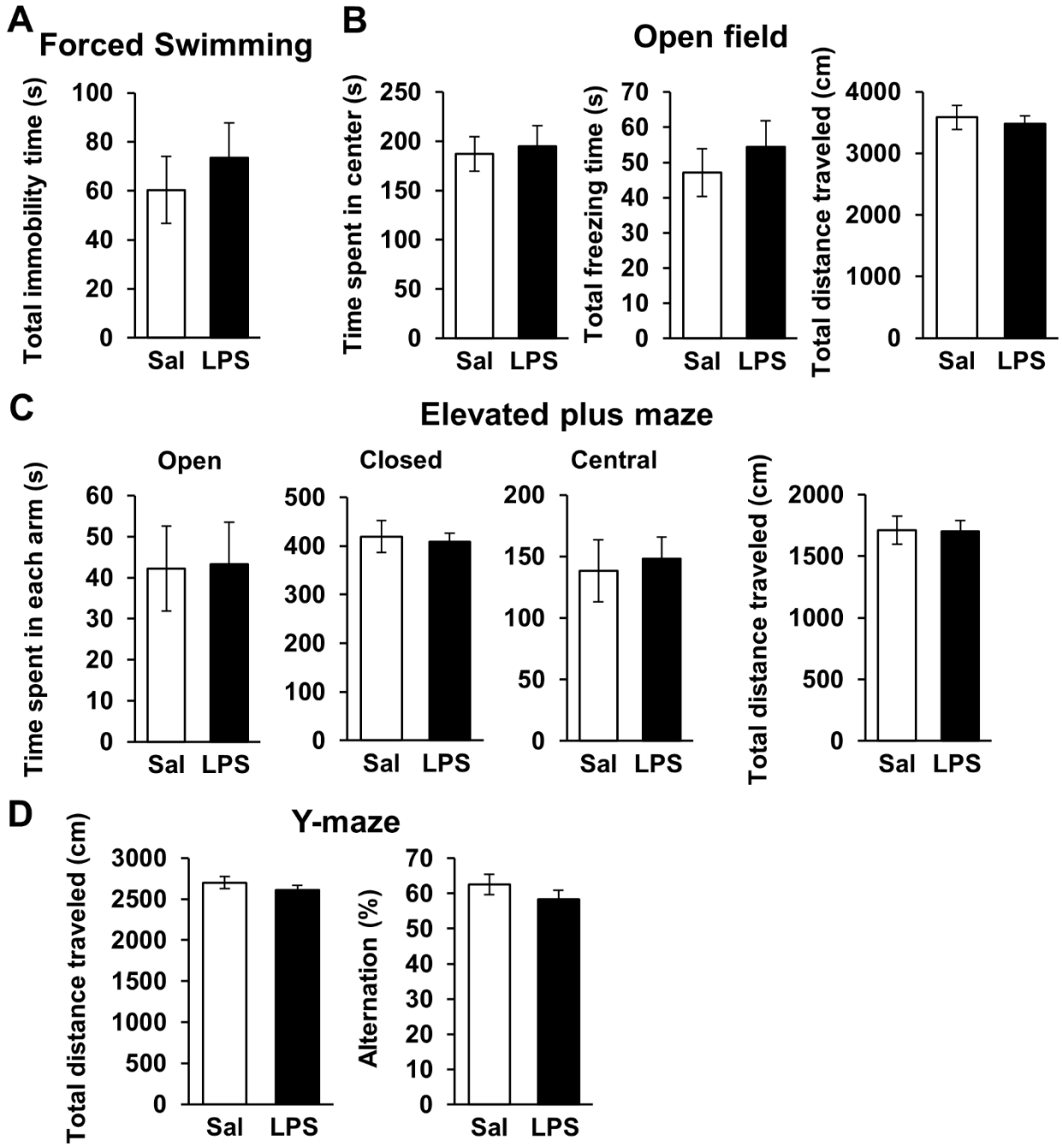

Figure 3. Behavioral tests for spontaneous locomotor activity, depression, anxiety, and working memory 7 days after LPS injection.

(A-D) Total immobility time (s) in forced swimming test (5 min, A), time spent in center (s), total freezing time (s), and total distance traveled (cm) in open field test (10 min, B), time spent in each arm (s) and total distance traveled (cm) in elevated plus maze test (10 min, C), and total distance traveled (cm) and alternation score (%) in Y-maze tests (8 min, D) 7 days after LPS injection (3 mg/kg, *i.p.,* single dose). Sal: saline. n = 6-8 mice/group. All data are expressed as means ± S.E.M.

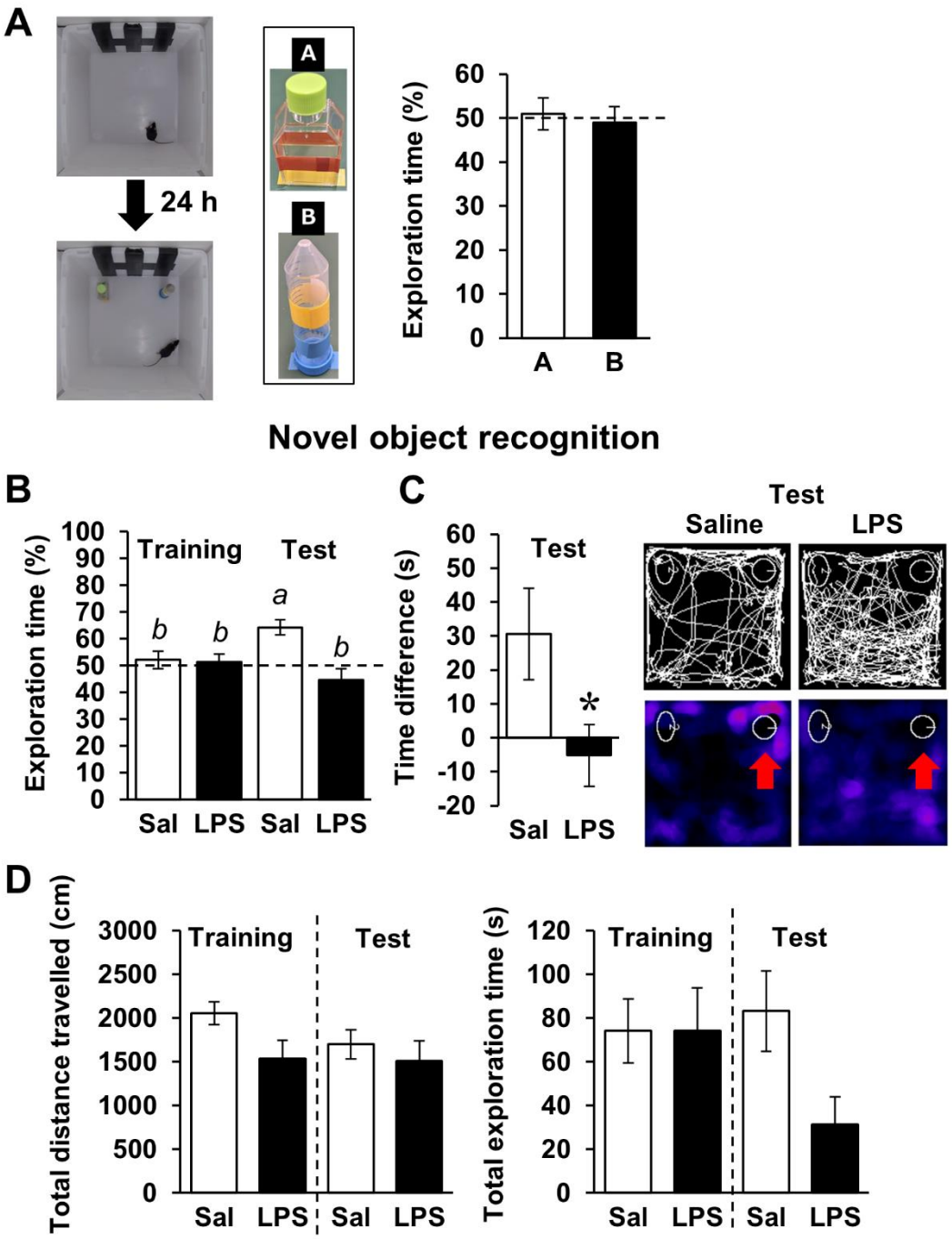

Figure 4. Novel object recognition test 7 days after LPS injection.

(A) The test section was conducted 24 hours after the habituation section in normal mice. (B-D) Exploration time of novel object (%, B), difference in first recognition time (s, C), representative images of mouse traces and heat maps (red arrow: novel object), total distance traveled (cm, D), and total exploration time (s) in novel object recognition test 7 days after LPS injection (3 mg/kg, *i.p.,* single dose). Sal: saline. n = 9–10 mice/group. Means with the different letter are significantly different and with the same letter are not significantly different from each other (Tukey's test, B), $*p < 0.05$ (unpaired Student's t-test, C). All data are expressed as means ± S.E.M.

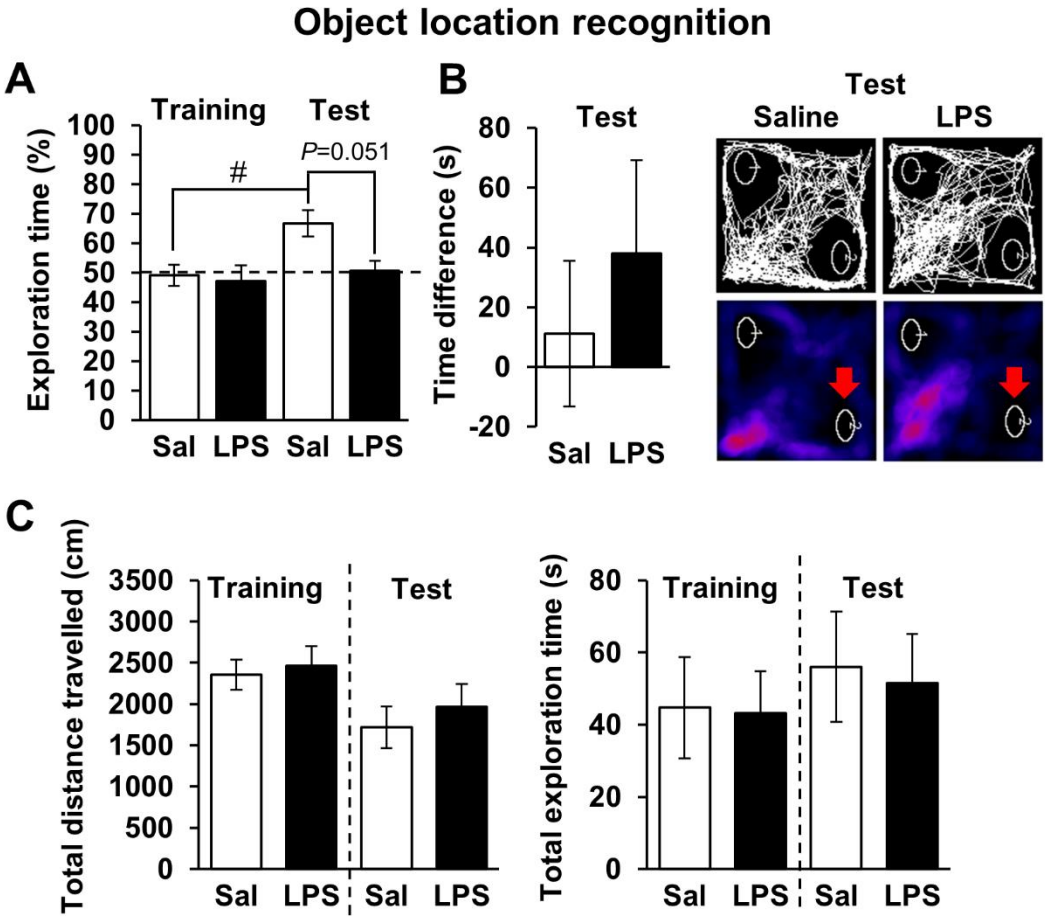

Figure 5. Object location recognition test 7 days after LPS injection.

(A-C) Exploration time of moved object (%, A), difference in first recognition time (s, B), representative images of mouse traces and heat maps (red arrow: moved object), total distance traveled (cm, C), and total exploration time (s) in object location recognition test 7 days after LPS injection (3 mg/kg, *i.p.,* single dose). Sal: saline. n = 10 mice/group. #$p < 0.05$ (Tukey's test, A). All data are expressed as means ± S.E.M.

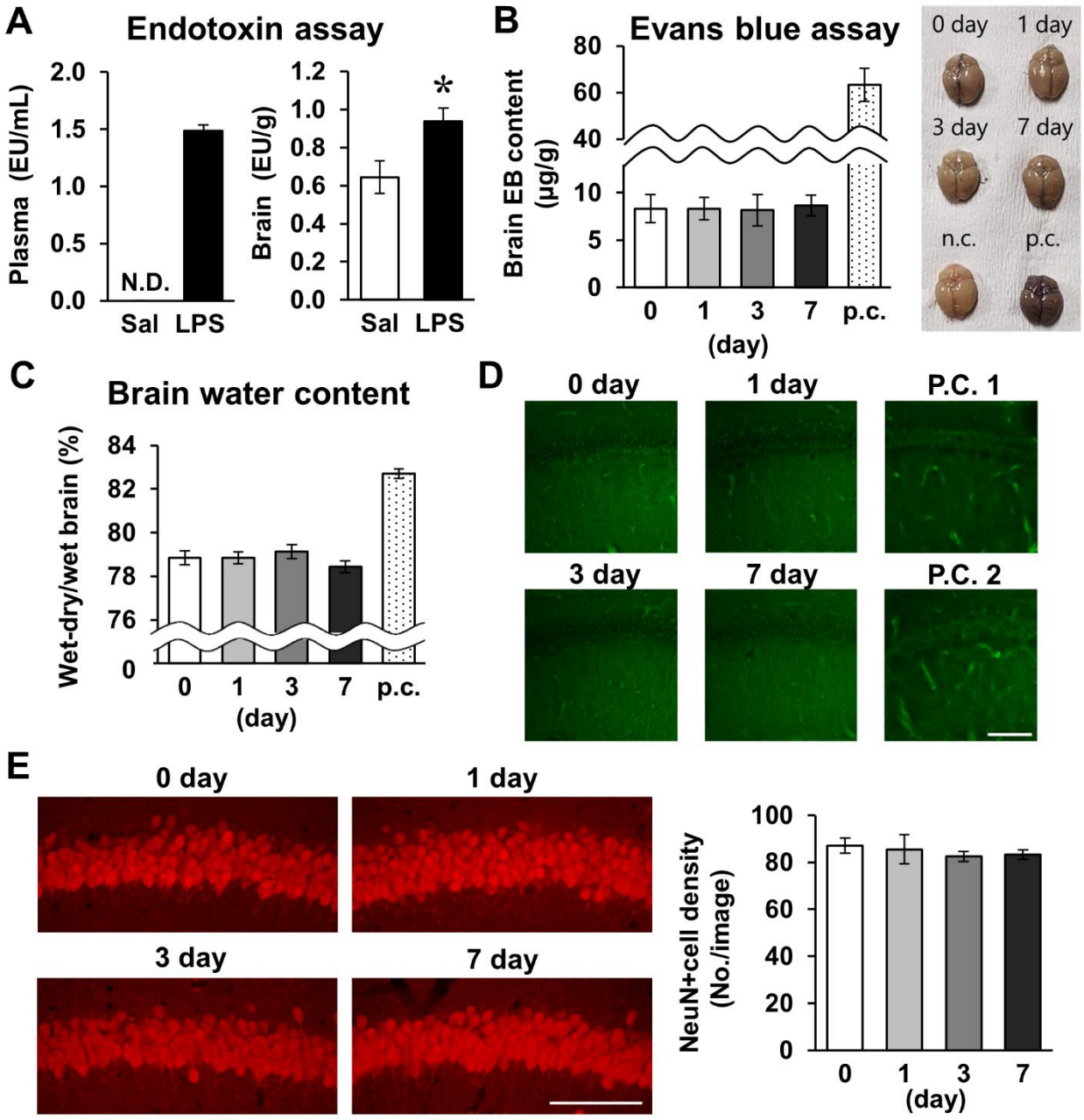

Figure 6. Effects of LPS on blood-brain barrier permeability and neuronal survival.
(A) Endotoxin level detected by endotoxin assay (LAL tests) of plasma (EU/mL, left) and brain (EU/g, right) tissues of mice 24 hours after LPS injection (3 mg/kg, *i.p.*, single dose). Sal: saline. n = 5 mice/group. *$p < 0.05$ (unpaired Student's t-test). (B, C) Evans blue content (μg/g) and brain representative images (B), and whole-brain water content (wet-dry/wet, %, C) 0–7 days after LPS injection. p.c.: positive control (LPS 18 mg/kg, *i.p.*, 18 h). n = 5 mice/group. (D) Representative images of the hippocampal CA1 region stained with PathoGreenTM. p.c.: positive control (LPS 18 mg/kg, *i.p.*, 18 h). Scale bar = 100 μm. (E) Representative NeuN-stained images of hippocampal CA1 regions 0–7 days after LPS injection (left) and NeuN-positive cell density (number of cells/image, right). n = 6 mice/group. Scale bar = 100 μm. All data are expressed as means ± S.E.M.

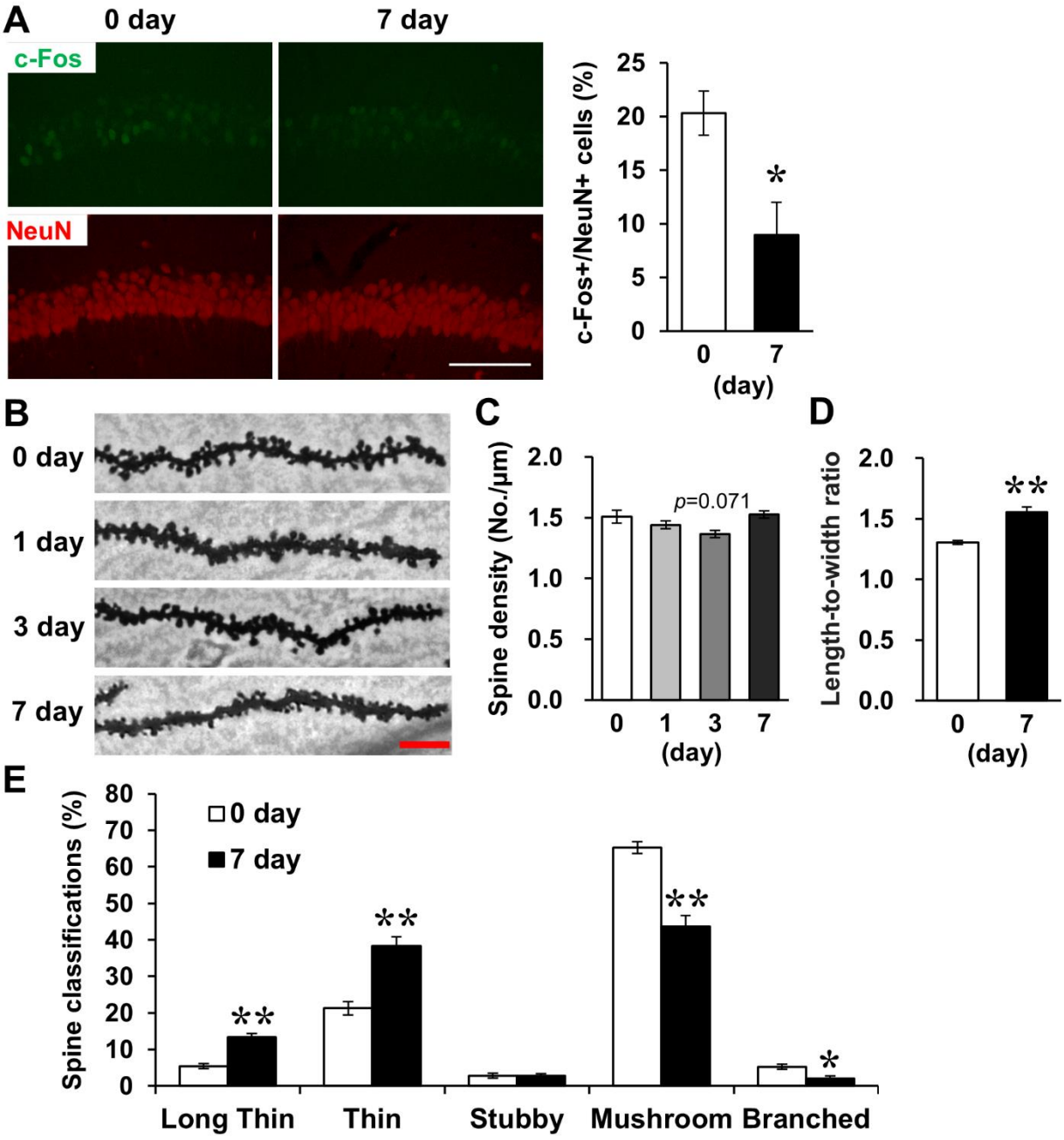

Figure 7. Effects of LPS on neuronal activity and dendritic spine properties.

(A) Representative c-Fos (green) and NeuN (red)-stained images in the hippocampal CA1 regions of mice 0 and 7 days after LPS injection (3 mg/kg, *i.p.,* single dose, left) and percentage of c-Fos-positive cells in NeuN-positive cells (right). Scale bar = 100 μm. n = 6 mice/group. (B) Representative images in the hippocampal CA1 region stained with Golgi-Cox staining of mice 0–7 days after LPS injection. Scale bar = 5 μm. (C) Quantification of spine density (number of spines/μm) in the hippocampal CA1 region of mice 0–7 days after LPS injection. n = 6 mice/group. (D, E) Quantification of length-to-width ratio (D) and classification (%, E) of the spines by morphology in the hippocampal CA1 region of mice 0 and 7 days after LPS injection using the Reconstruct application. n = 6 mice/group. *$p < 0.05$, **$p < 0.01$ (unpaired Student's t-test). All data are expressed as means ± S.E.M.

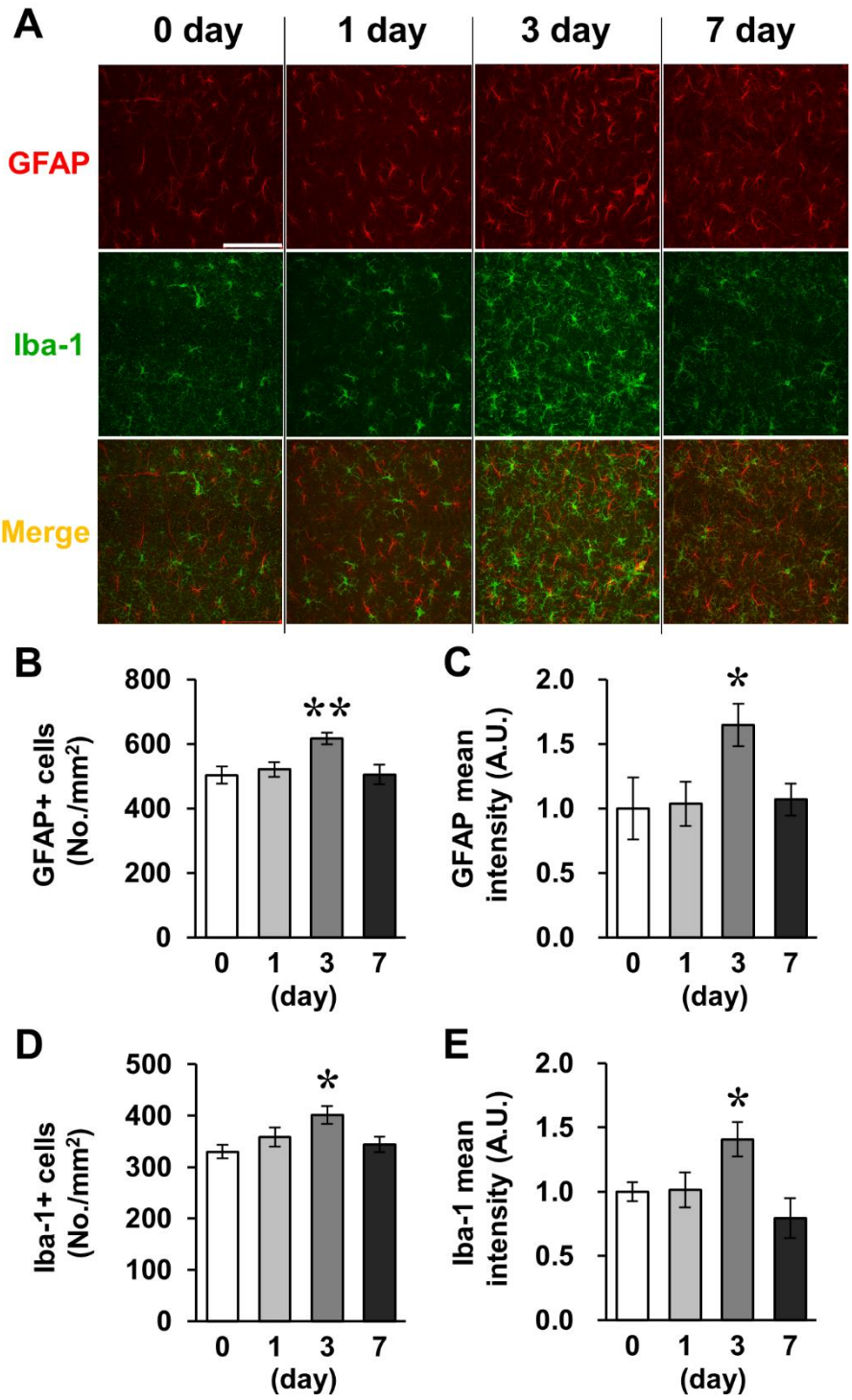

Figure 8. Effects of LPS on glial activation marker GFAP and Iba-1

(A) Representative GFAP (red), Iba-1 (green), and DAPI (blue)-stained images in the hippocampal CA1 region of mice 0–7 days after LPS injection (3 mg/kg, *i.p.*, single dose). Scale bar = 100 μm. (B-E) Density of GFAP- or Iba-1-positive cells (number of cells/mm^2, B, D) and GFAP or Iba-1 mean fluorescence intensity (A.U., C, E) in the hippocampal CA1 region of mice 0–7 days after LPS injection. n = 7 mice/group. *$p < 0.05$, **$p < 0.01$ vs. 0 day (Dunnett's test). All data are expressed as means ± S.E.M.

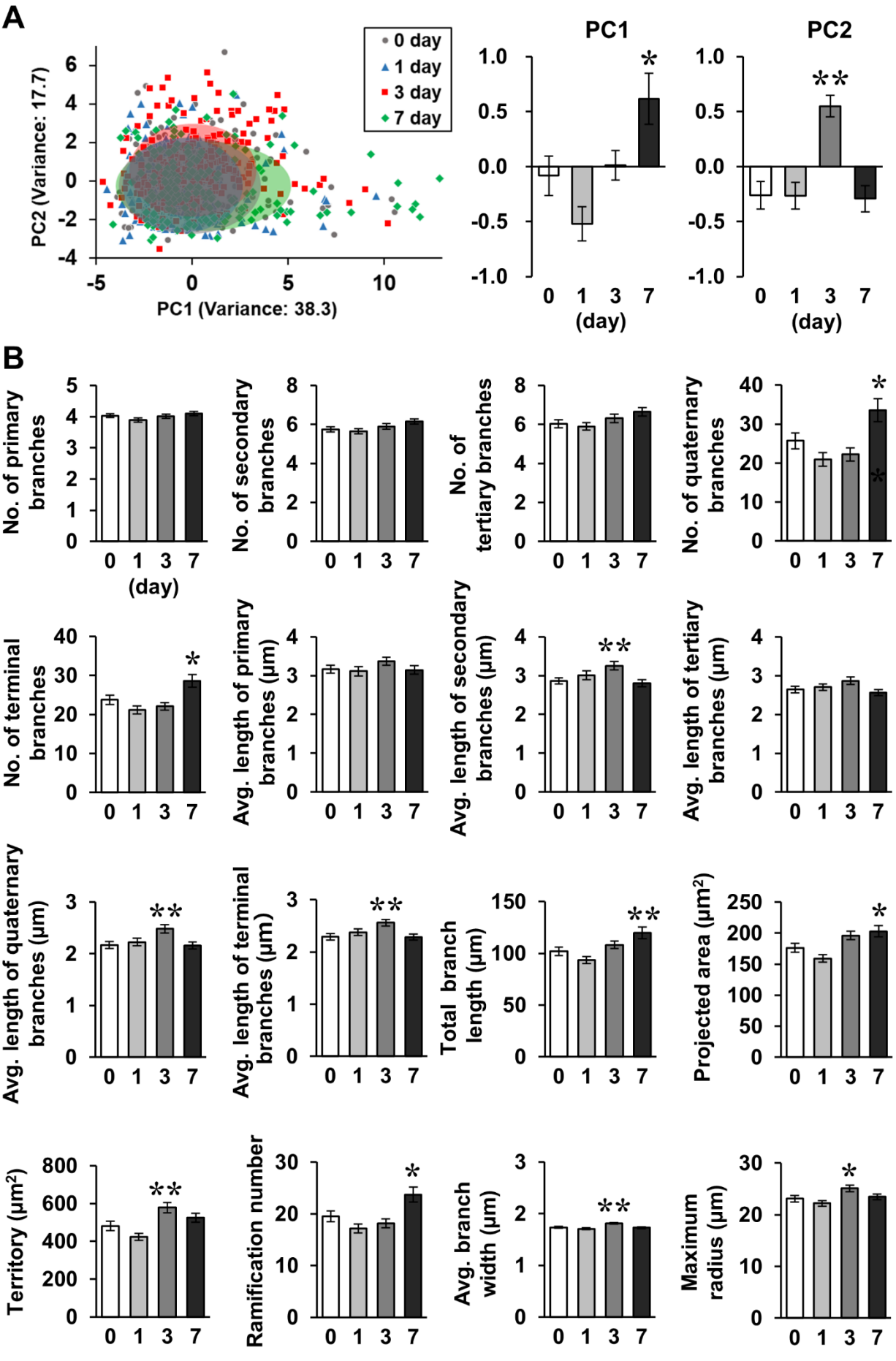
A
0 day
1 day
3 day
7 day
PC2 (Variance: 17.7)
PC1 (Variance: 38.3)
PC1
PC2
(day)
B
No. of primary branches
No. of secondary branches
No. of tertiary branches
No. of quaternary branches
No. of terminal branches
Avg. length of primary branches (μm)
Avg. length of secondary branches (μm)
Avg. length of tertiary branches (μm)
Avg. length of quaternary branches (μm)
Avg. length of terminal branches (μm)
Total branch length (μm)
Projected area (μm²)
Territory (μm²)
Ramification number
Avg. branch width (μm)
Maximum radius (μm)

C

Astrocyte	PC1	PC2
Total branch length	0.97	0.14
Ramification number	0.95	-0.19
No. of terminal branches	0.95	-0.21
No. of quaternary branches	0.92	-0.21
Projected area	0.91	0.34
Territory	0.80	0.47
Maximum radius	0.58	0.49
No. of tertiary branches	0.57	-0.02
Avg. length of terminal branches	-0.37	0.69
Avg. branch width	-0.14	0.65
Avg. length of secondary branches	-0.15	0.58
Avg. length of primary branches	-0.13	0.55
No. of secondary branches	0.41	0.00
No. of primary branches	0.16	-0.09
Ave. length of quaternary branches	0.03	0.52
Avg. length of tertiary branches	-0.06	0.54

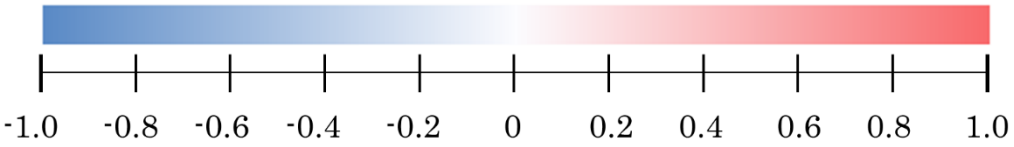

Figure 9. Effects of LPS on astrocytic morphology.

(A) Principal component (PC) analysis reduced the dimensionality of the feature space consisting of 16 morphological features extracted from GFAP-staining images in the hippocampal CA1 region of mice 0–7 days after LPS injection (3 mg/kg, *i.p.*, single dose). A two-dimensional PC analysis plot representing the first two PCs, overlaid with ellipses corresponding to three standard deviations centered on the mean. Graphs show PC1 and PC2 values. (B, C) Each parameter of astrocytic morphology of mice 0–7 days after LPS injection analyzed with SMorph (B) and contributions of each parameter to PCs (C). n = 172–192 cells (from 7 mice)/group. *$p < 0.05$, **$p < 0.01$ vs. 0 day (Dunnett's test). All data are expressed as means ± S.E.M.

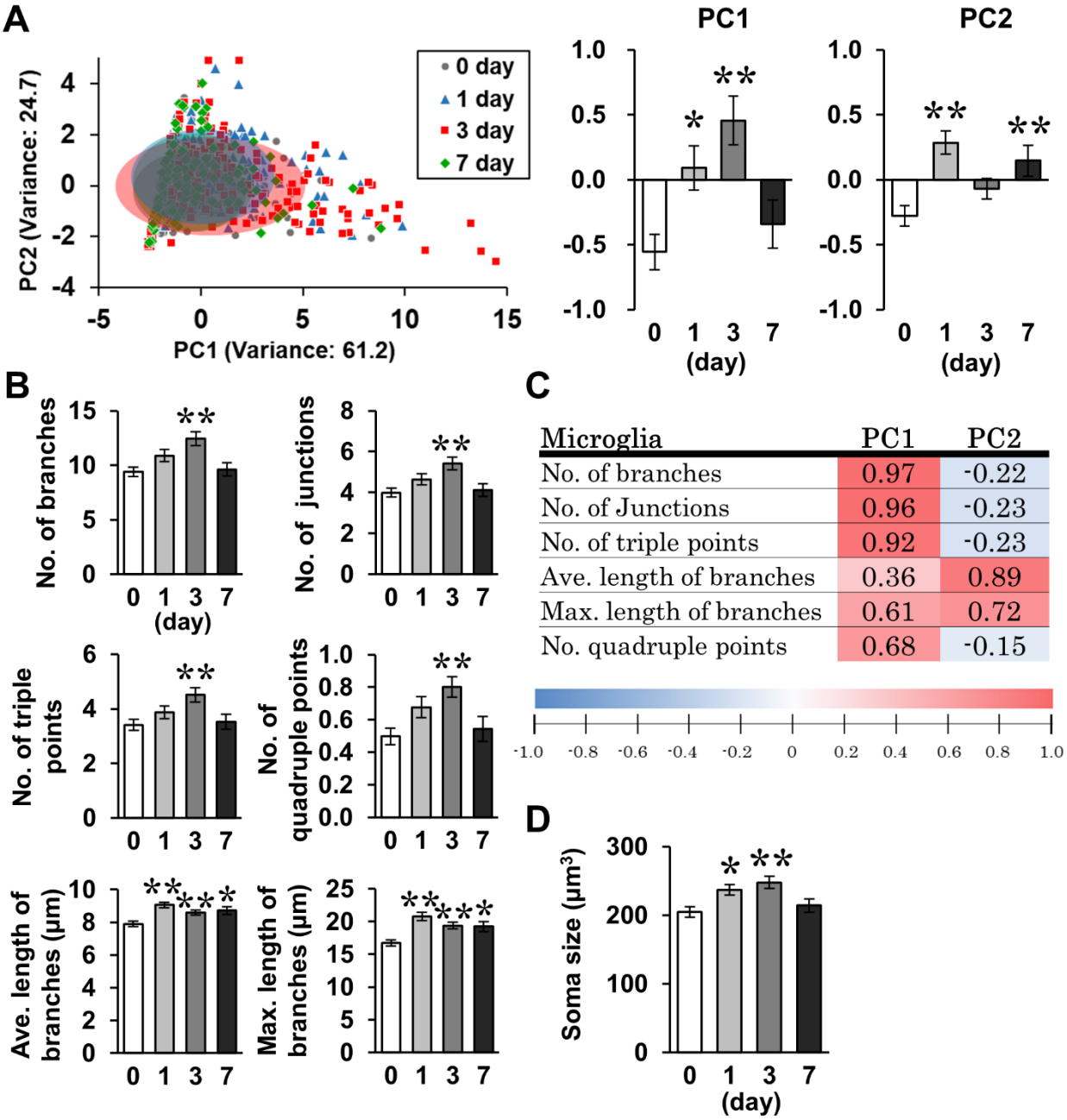

Figure 10. Effects of LPS on microglial morphology.

(A) Principal component (PC) analysis reduced the dimensionality of the feature space consisting of 6 morphological features extracted from Iba-1 staining images in the hippocampal CA1 region of mice 0–7 days after LPS injection (3 mg/kg, *i.p.*, single dose). A two-dimensional PC analysis plot representing the first two PCs, overlaid with ellipses corresponding to three standard deviations centered on the mean. Graphs show PC1 and PC2 values. (B, C) Each parameter of microglial morphology of mice 0–7 days after LPS injection analyzed with Image-J (B) and contributions of each parameter to PCs (C). n = 118–279 cells (from 7 mice)/group. (D) Mean soma size (μm^3) of Iba-1-positive cells of mice 0–7 days after LPS injection. n = 85–105 cells (from 7 mice)/group. $*p < 0.05$, $**p < 0.01$ vs. 0 day (Dunnett's test). All data are expressed as means ± S.E.M.

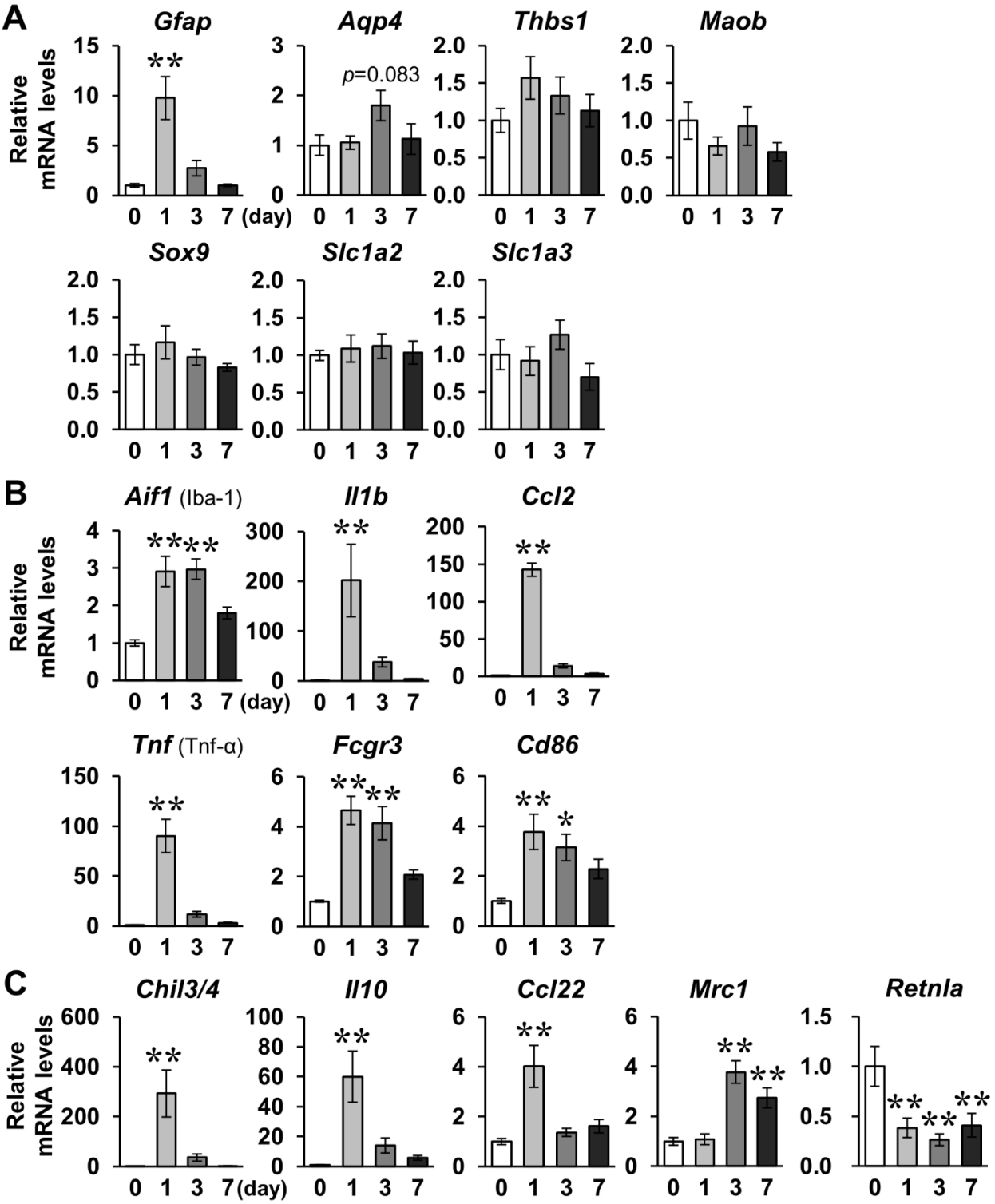

Figure 11. Effects of LPS on mRNA levels of glial activation markers.

(A-C) Whole hippocampus mRNA levels of the astrocytic activation markers *Gfap, Aqp4, Thbs1, Maob, Sox9, Slc1a2*, and *Slc1a3* (A); microglial M1 markers *Aif1, Il1b, Xcl2, Tnf, Fcgr3,* and *Cd86* (B); and M2 markers *Chil3/4, Il10, Ccl22, Mrc1*, and *Retnla* (C) of mice 0–7 days after LPS injection (3 mg/kg, *i.p.*, single dose). n = 8 mice/group. *$p < 0.05$, **$p < 0.01$ vs. 0 days (Dunnett's test). All data are expressed as means ± S.E.M.

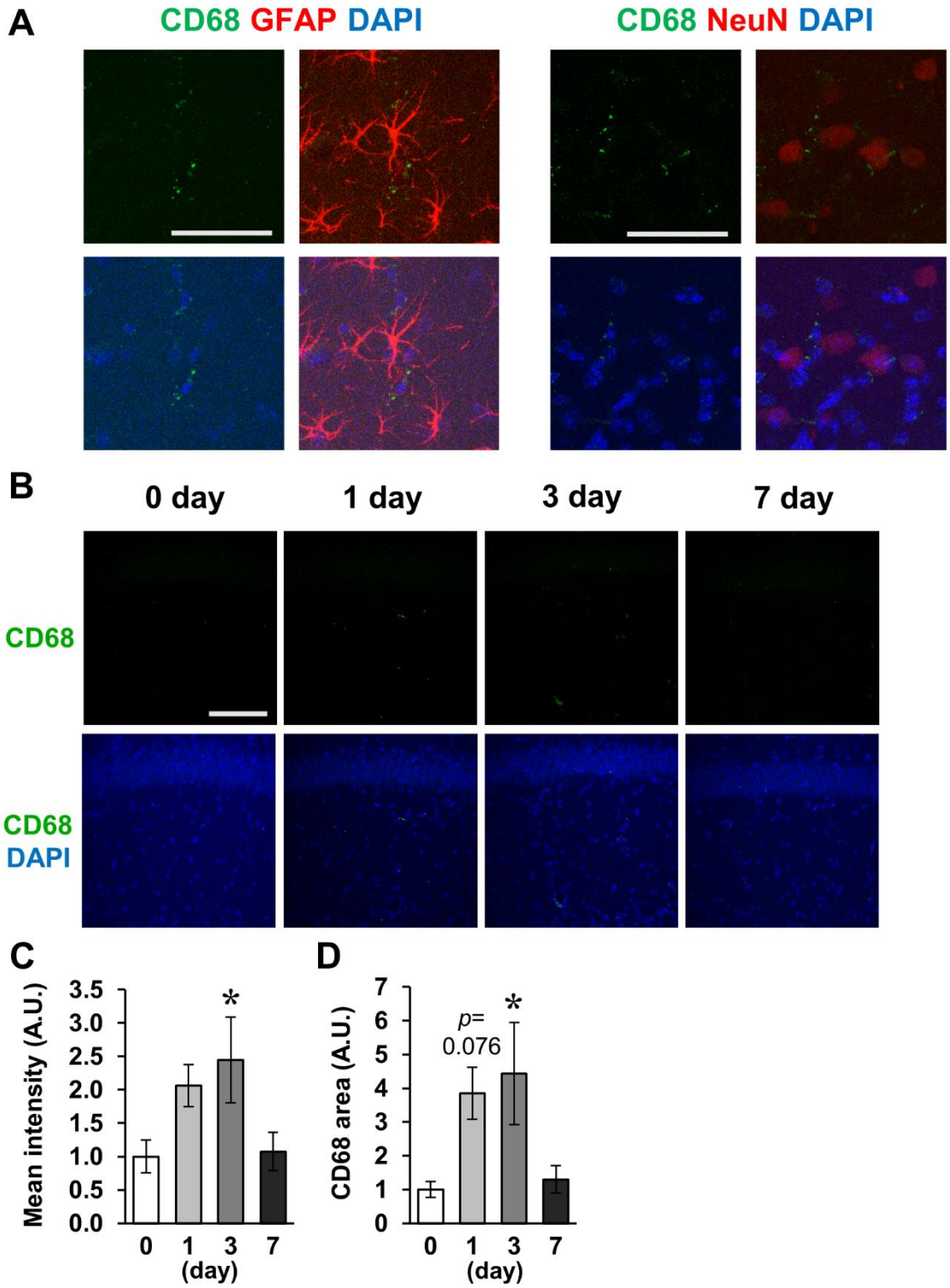

Figure 12. Effects of LPS on expression of microglial phagocytic marker CD68.

(A) Representative CD68 (green) and GFAP or NeuN (red)-stained images in the hippocampal CA1 region of mice 3 days after LPS injection (3 mg/kg, *i.p.*, single dose). (B) Representative CD68 (green) and DAPI (blue)-stained images in the hippocampal CA1 region of mice 0–7 days after LPS injection (C, D) Mean fluorescence intensity (C) and area (D) of CD68. n = 8 mice/group. $*p < 0.05$ vs. 0 days (Dunnett's test). Scale bar = 100 μm. All data are expressed as means ± S.E.M.

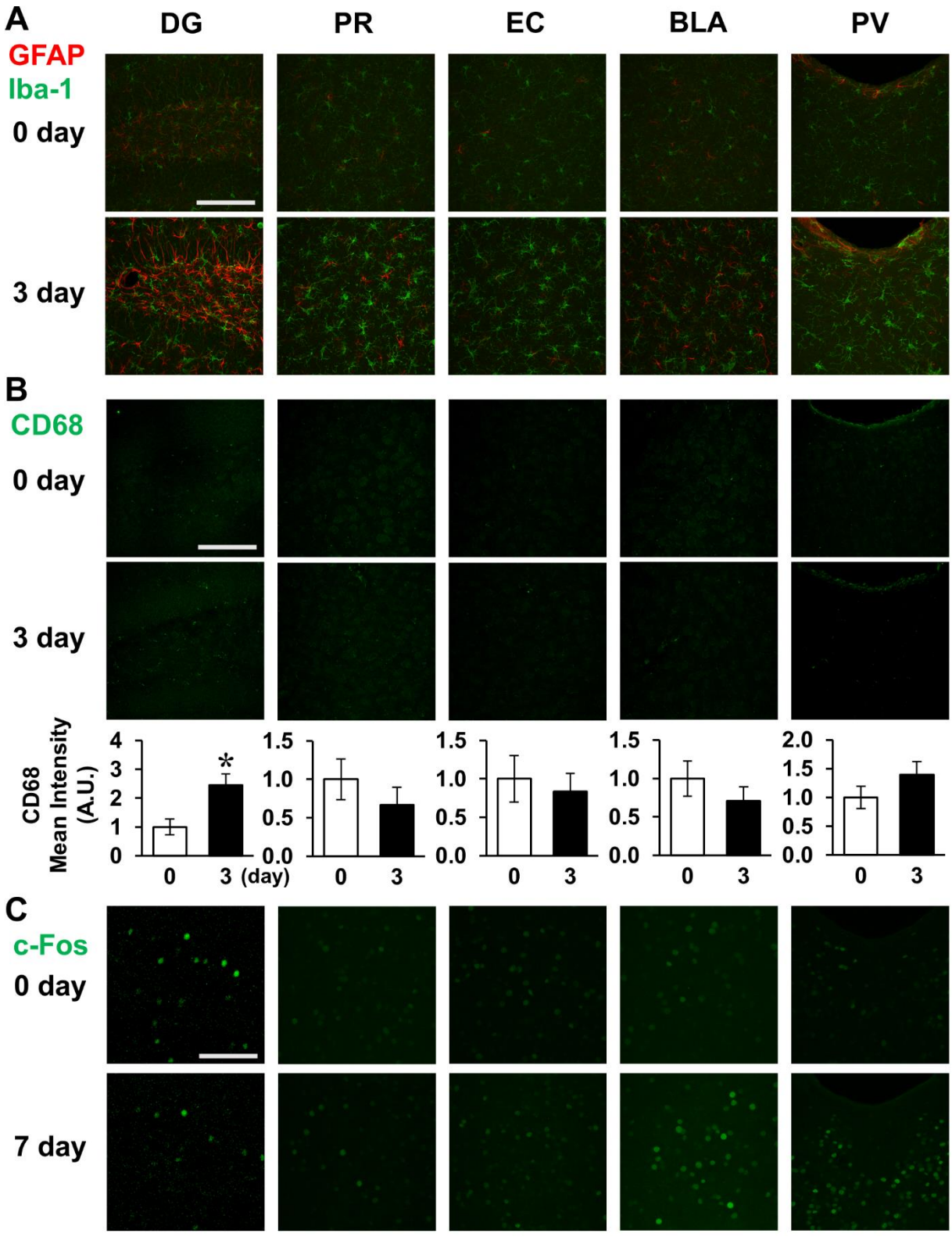

Figure 13. Effect of LPS on neuronal and glial activation in different brain regions.

(A-C) Representative GFAP and Iba-1 (A), CD68 (B), and c-Fos (C) images in the dentate gyrus (DG), perirhinal cortex (PR), entorhinal cortex (EC), basolateral amygdala (BLA), and paraventricular hypothalamic nucleus (PV) of mice 0 and 3 (A, B) or 7 (C) days after LPS injection (3 mg/kg, *i.p.*, single dose). (B) Mean fluorescence intensity of CD68 (A.U.) in each brain region of mice 0 and 3 days after LPS injection (3 mg/kg, *i.p.*, single dose). n = 5 mice/group. $*p < 0.05$ (unpaired Student's t-test). All data are expressed as means ± S.E.M.

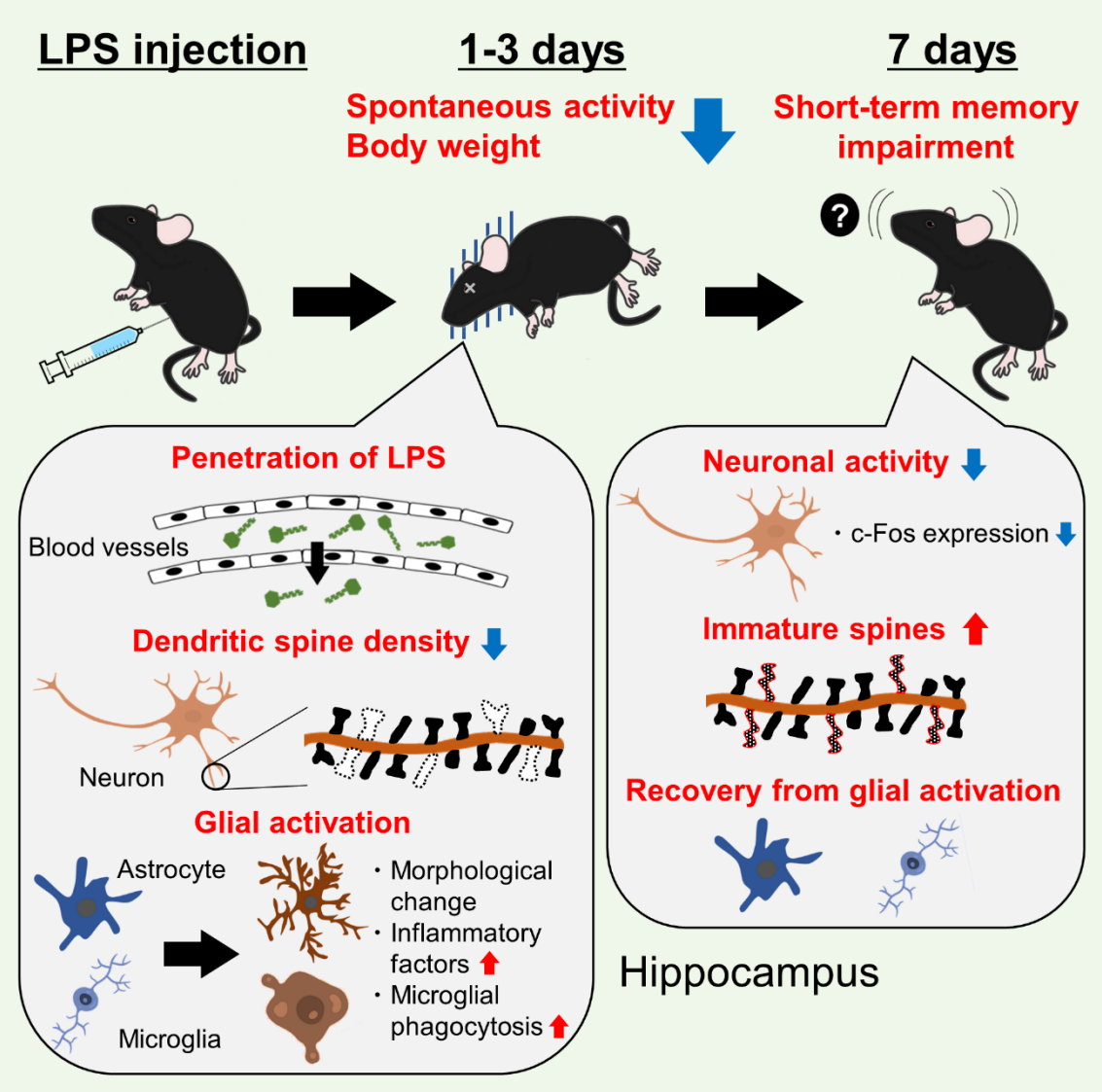

Figure 14. Graphical abstract in Chapter 1.

Chapter II:
Catecholamine regulates astrocytic IL-6 expression and process formation via dopamine receptors and adrenoceptors

II-1 Introduction

Astrocytic cytokine production and the morphology of astrocytic processes are closely related to the physiological functions of the central nervous system (CNS). Proinflammatory cytokines affect neuronal functions besides enhancing inflammation. IL-6 released from astrocytes suppresses neuronal cell death (Day *et al.*, 2014) and acts as a neurotrophic factor (Wagner, 1996). Astrocytic processes contact neurons, forming the "tripartite synapse" that regulates synaptic function (Allen and Eroglu, 2017).

Furthermore, astrocytes transform into reactive astrocytes in response to a wide range of neurodegenerative diseases (Pekny and Nilsson, 2005; Hart and Karimi-Abdolrezaee, 2021). Reactive astrocytes are characterized by upregulated IL-6 and GFAP expression and distinct morphological changes (John *et al.*, 2003; Sofroniew, 2009; Escartin *et al.*, 2021), and regarded as reflections of a detrimental astrocyte phenotype, which contribute to various pathogeneses (Escartin *et al.*, 2021). Specifically, chronic IL-6 overexpression in astrocytes induces an inflammatory response (Penkowa *et al.*, 2003). Impaired astrocytic morphogenesis links to diminished function of excitatory synapses (Stogsdill *et al.*, 2017). In Chapter I, consistent with these reports, LPS *i.p.* injection promoted GFAP expression and morphological change in astrocytes and expression of multiple proinflammatory cytokines, therefore, reactive astrocytes may be involved in the pathogenesis of mental disorder. However, the mechanisms that control these reactive states of astrocytes complexly involve a variety of factors, and have not been completely understood.

In Chapter II, I focused on catecholamines, such as dopamine and noradrenalin, as the regulator of neuroinflammation. Dopamine or noradrenaline levels in the CNS change under pathological conditions with neuroinflammation, such as Alzheimer's disease, Parkinson's disease, Huntington's disease, and ischemic stroke (Globus *et al.*, 1989; Hoogendijk *et al.*, 1999; Klein *et al.*, 2019). In addition, mice treated intraperitoneally with LPS have increased levels of catecholamines in the brain (Mori *et al.*, 2003; Sekio and Seki, 2015). Catecholamines are released not only from synapses but also from varicosities (Fuxe *et al.*, 2015), and thus act on astrocytes surrounding neurons. Especially, the activation of astrocytic dopamine receptors regulates neuroinflammation

(Zhu *et al.*, 2018; Montoya *et al.*, 2019) and depresses excitatory synaptic transmission (Corkrum *et al.*, 2020). These reports suggest that catecholamines are involved in the pathogenesis of CNS diseases with neuroinflammation via their action on astrocytes.

Astrocytes express catecholamine receptors, *i.e.* D1-like (D_1, D_5) and D2-like (D_2-D_4) receptors, and α_1-, α_2- and ß-ARs. Noradrenaline acts on astrocytic ß-ARs to enhance IL-6 transcription and change cell morphology (Day *et al.*, 2014; Kitano *et al.*, 2021). However, it remains unknown whether other adrenoceptors or dopamine receptors affect astrocytic IL-6 production or morphology and, if so, which receptors and intracellular pathways are involved. Such knowledge could enhance our understanding of the role that catecholamines play in astrocytic functions and the pathogenesis of neurodegenerative diseases caused by abnormal catecholamine signalings. Therefore, I aimed to comprehensively identify IL-6 expression and morphological changes in response to catecholamines, as a phenotype of reactive astrocytes. In this study, I identified dopamine receptor- and adrenoceptor-subtypes that participate in the IL-6 expression and morphological changes, and investigated the intracellular signaling following the activation of each receptor in rat cultured astrocytes and acute brain slices.

II-2 Materials and methods

2.1 Materials

The following reagents were used: atenolol, atipamezole hydrochloride, dexmedetomidine hydrochloride, 2-bromo-α-ergocryptine methanesulfonate salt (bromocriptine), and isoproterenol hydrochloride (all from Sigma-Aldrich); phenylephrine hydrochloride, propranolol hydrochloride, forskolin, U0126, SP600125, histamine dihydrochloride, and L(+)-ascorbic acid (all from FUJIFILM Wako Pure Chemical); 1-phenyl-2,3,4,5-tetrahydro-1H-3-benzazepine hydrochloride (SCH23390), (±)-6-chloro-2,3,4,5-tetrahydro-1-phenyl-1H-3-benzazepine hydrobromide (SKF81297), 6-chloro-2,3,4,5-tetrahydro-1-(3-methylphenyl)-3-(2-propenyl)-1H-3-benzazepine-7,8-diol hydrobromide (SKF83822), and 6-chloro-2,3,4,5-tetrahydro-3-methyl-1-(3-methylphenyl)-1H-3-benzazepine-7,8-diol (SKF83959) (all from Tocris Bioscience, Bristol, UK); L-noradrenaline bitartrate monohydrate, prazosin hydrochloride, and 3-hydroxytyramine hydrochloride (dopamine) (all from Tokyo Chemical Industry, Tokyo, Japan); ICI118551 hydrochloride and SR59230A (both from MedChemExpress, Monmouth Junction, NJ, USA); H89 and bisindolylmaleimide II (BIM) (both from Cayman Chemical, Ann Arbor, MI, USA); haloperidol (Pfizer); and 5-hydroxytryptamine hydrochloride (5-HT) (Nacalai Tesque, Kyoto, Japan).

2.2 Animals

Prior to initiating studies, all animal care and experimental protocols were approved by the Committee on Animal Experimentation, Graduate School of Veterinary Medicine, Hokkaido University (No. 19-0009), which was awarded the Accreditation Status by the Association for Assessment and Accreditation of Laboratory Animal Care International. Animal studies were performed in compliance with ARRIVE guidelines (Percie du Sert *et al.*, 2020). Wistar rats were obtained from CLEA Japan and were bred to obtain pups. The rats were fed ad libitum and kept a 12/12 hour light/dark cycle at 22 ± 4 °C. Male and female pups (3–5 days old) were used for primary astrocyte cultures, and male pups (14–16 days old) were used for acute brain slice experiments.

2.3 Primary cultured astrocytes

Primary cultured astrocytes were obtained as previously described (Kitano *et al.*, 2021). In brief, the cerebral cortex, hippocampus, and spinal cords were isolated from rat pups (3–5 days old), minced, and incubated with papain (10 U/mL) and DNase (0.1

mg/mL). Dissociated cells were suspended in Dulbecco's modified Eagle's medium/Ham's F-12 (#048-29785, FUJIFILM Wako Pure Chemical) containing 10% fetal bovine serum, 100 U/mL penicillin, and 0.1 mg/mL streptomycin. The cell suspension was seeded onto a poly-l-lysine-coated T75 flask. After 7–8 days, the flask was shaken at 250 rpm at 37 °C for at least 12 hours to remove all cells except astrocytes. Adherent cells were detached with trypsin and re-seeded onto poly-l-lysine-coated 12-well plates or coverslips at a density of 8.0×10^3 cells/cm^2. After 3 days, the cell culture reached confluence, and the medium was changed to serum-free medium. Cell cultures were first treated with antagonists immediately after the medium exchange and were then treated with dopamine, noradrenaline, and other agonists 1 hour after the medium exchange. After a certain amount of time (detailed in the figure legends and results section), the cell culture was used for experiments. The concentrations of dopamine used in this study were determined based on the previous reports (Cragg and Rice, 2004; Koppel *et al.*, 2018). Agonists and antagonists were used at concentrations specific to the target receptors, based on the database ("IUPHAR/BPS Guide to PHARMACOLOGY" https://www.guidetopharmac). The purity of astrocyte cultures was evaluated by immunostaining for the astrocytic marker GFAP. At least 300 cells in 12 randomly selected images were evaluated, and all cells I evaluated were positive for GFAP.

2.4 RNA extraction and real-time PCR analyses

Total RNA was extracted from cultured astrocytes using RNAiso Plus. To remove genomic DNA and synthesize cDNA, the RNA sample was then incubated with qPCR RT Master Mix with gDNA Remover. Real-time PCR was performed using Thunderbird SYBR qPCR Mix, each primer, and the cDNA reaction solution. The primer sequences are provided in Table 3. Thermal cycles were performed using the Eco Real-Time PCR System (Illumina). Cycling conditions were 95 °C for 1 minute (for initial denaturation), followed by 40 cycles of denaturation (95 °C, 15 seconds), annealing, and extension (temperature: Tables 3 and 45 seconds). RNAs without reverse transcription were used as a negative control to examine DNA contamination and were not amplified by real-time PCR. Melt curve analysis confirmed that the obtained amplicon was only the one expected in each reaction. The expression levels of IL-6 relative to GAPDH were calculated using the ΔΔCq method and were normalized to the control, which was arbitrarily set to a value of "1.0".

2.5 Non-quantitative PCR

Non-quantitative PCR was performed using KOD FX Neo (TOYOBO), each primer, and the cDNA reaction solution obtained by the above method. The primer sequences and product sizes are provided in Table 4. Thermal cycles were performed using a PC320 system (ASTEC, Fukuoka, Japan). Cycling conditions were 94 °C for 1 minute (for initial denaturation), followed by 40 cycles of denaturation (98 °C, 10 seconds), annealing (temperature: Tables 4 and 10 seconds), and extension (68 °C, 30 seconds). RNAs without reverse transcription were used as a negative control to examine DNA contamination. PCR products and a 100 bp DNA ladder (Takara Bio) were separated on a 3% agarose gel and visualized with ethidium bromide under UV illumination (Mupid-Scope WD, Mupid, Tokyo, Japan).

2.6 Western blotting

Astrocytes were lysed in RIPA buffer containing a protease inhibitor cocktail (Nacalai Tesque). The samples were separated by 10% SDS-PAGE and transferred to polyvinylidene difluoride membranes (Millipore, CA, USA). The membranes were blocked with 5% skimmed milk and then incubated with primary antibodies (Table 5) at 4 °C for at least 12 hours. Thereafter, the membranes were incubated for 1 hour at RT with a horseradish peroxidase-conjugated secondary antibody (#NA931 or #NA934, 1:3000, GE Healthcare, Little Chalfont, UK). Antibody binding was visualized by ECL Prime (GE Healthcare). Band intensities were measured using Fiji-ImageJ software (National Institutes of Health) and normalized to the control, which was arbitrarily set to a value of “1.0”.

2.7 Enzyme-linked immunosorbent assay (ELISA)

I measured the IL-6 protein levels using IL-6 ELISA Kit (#437107, Biolegend, San Diego, CA, USA). The medium of cultured astrocyte treated with each drug for 6 h was collected. Thereafter, the medium was centrifuged at 1000 × g for 10 minutes to remove dead cells and debris, and the supernatant was used for ELISA. The experiment was performed according to the manufacturer's instructions and the ELISA plates were read with an SH-1000 lab fluorescent microplate reader (Corona Electric Co.) and analyzed using SF6 software (Corona Electric Co.). Quantification of astrocyte total protein was performed for cells in each cultured well using the DC™ Protein Assay reagent (Bio-Rad, Hercules, CA, USA). The IL-6 level was normalized by calculating the IL-6 protein content per astrocyte total protein content (pg/mg).

2.8 Preparation and treatments of astrocyte conditioned medium

Agonists or antagonists were treated to the primary cultures of astrocytes in the manner described above. Following agonist treatments for 30 minutes, cells were refreshed with serum-free medium. After 24-hour incubation, the medium was collected from each treated well. RNA extraction was performed at the same time as the medium was collected. The medium was centrifuged at 300 × g to remove dead cells and the supernatant was used as astrocyte conditioned medium (ACM). The drug-treated astrocytes to produce ACM were defined as ACM-donor cells. The ACM was transferred to another primary culture of astrocytes, which was defined as ACM-recipient cells. The ACM-recipient cells were incubated for 3 hours followed by RNA extraction.

2.9 Phalloidin staining and evaluation of astrocytic morphology *in vitro*

Phalloidin staining and evaluation of astrocytic morphology were conducted as previously described (Kitano *et al.*, 2021). Astrocytes cultured on coverslips were fixed with 4% PFA for 20 minutes at RT and then permeabilized with PBS containing 0.1% Triton X-100 at RT for 5 minutes. To stain filamentous actin (F-actin), cells were incubated with Phalloidin-iFluor 488 reagent (#ab176753, 1:1000, Abcam, Cambridge, UK) in PBS containing 1% bovine serum albumin at RT for 1 hour. Coverslips were mounted onto glass slides with DAPI-Fluoromount G (SouthernBiotech). Fluorescence images were obtained with a fluorescence microscope (BZ-9000, KEYENCE) using a 20 × lens objective. Astrocytes with process formation were defined as cells that had one or more processes longer than the width of their cell bodies. The number of astrocytes with process formation was visually counted using Fiji-ImageJ software. The mean percentage from more than 200 cells from three random images was used as one independent measurement.

2.10 Preparation of acute hippocampal slices

Male pups (14–16 days old) were anesthetized with isoflurane (Pfizer) inhalation and rapidly decapitated. The brains were then quickly detached and transferred into ice-cold artificial cerebrospinal fluid (ACSF) and constantly oxygenated with 95% O_2 and 5% CO_2. The composition of ACSF was as follows (mM): 125 NaCl, 2.5 KCl, 2.0 $CaCl_2$, 1.0 $MgCl_2$, 26 $NaHCO_3$, 1.25 NaH_2PO_4, and 25 glucose (pH 7.3–7.4). The brain was glued to a slicer stage (LinearSlicer Pro7, Dosaka EM), flooded in oxygenated cold ACSF, and cut into 300 μm-thick coronal slices. The slices were incubated for 30 minutes at 22–24 °C in continuously oxygenated ACSF. Afterward, the slices, in

continuously oxygenated ACSF containing L(+)-ascorbic acid (200 μM), were incubated for 30 minutes and treated with isoproterenol, dopamine, or SKF81297 for 90 minutes at 34 °C.

2.11 Immunohistochemistry

The slices obtained by the above method were fixed with 4% PFA for 12 hours at 4 °C and then blocked for 6 hours with a blocking buffer composed of 10% goat serum, 0.5% Triton X-100, and 0.05% sodium azide in PBS. The slices were then incubated with an anti-GFAP primary antibody at 4 °C for at least 12 hours and incubated with an Alexa Fluor 555-conjugated goat anti-mouse antibody (#A21422, 1:500, Thermo Fisher Scientific) for 2 hours at RT. The slices were mounted onto glass slides with DAPI-Fluoromount G, and images were observed with a laser scanning confocal microscope (LSM 700, Carl Zeiss) using a 40 × lens objective. The CA1 areas of the hippocampus were used to measure the fluorescence intensity. The images (shown in Figure 25A) were used for the fluorescence intensity measurements and were composed of 15 μm Z-stacks consisting of 16 optical slices of 1 μm thickness by maximum intensity projection. The mean grey intensity in the area excluding the neuronal layer was measured using Fiji-ImageJ. The results were expressed as arbitrary units.

2.12 Morphological analysis of astrocytes in hippocampal slices

Morphological features of astrocytes in the CA1 area of the hippocampus were assessed using the confocal Z-stack images obtained by immunohistochemistry. For analysis, I applied Simple Neurite Tracer, a free software plugin distributed by Fiji-ImageJ and available at (https://imagej.net/plugins/snt/), as previously described (Tavares *et al.*, 2017). The morphological parameters assessed by Simple Neurite Tracer were the total branch length, number of branches, and average branch length. Additionally, I performed Sholl analysis, which measures the number of intersections at concentric spheres (at 4 μm intervals) originating from the soma. The mean value of 10 cells in one immunohistochemistry image was used as one independent measurement.

2.13 Data and statistical analysis

All the studies were designed to generate groups of equal size, using randomization and blinded analysis. Data are expressed as means ± S.E.M (n = number of independent measurements) of at least five independent experiments (biological replicates). After confirming that the data were normally distributed, the following tests

were performed. Statistical comparisons between the two groups were made using the unpaired Student's t-test. For all multiple comparisons, the Dunnett's test or Tukey's test was used. The Dunnett's test or Tukey's test was performed only if F achieved $p < 0.05$ and there was no significant inhomogeneity of variance by one-way ANOVA. A value of $p < 0.05$ was considered statistically significant. All statistical analysis was performed using the statistical analysis software JMP® 14 (SAS Institute, Inc., Cary, NC, USA).

II-3 Results

3.1 Dopamine increases IL-6 mRNA levels in cultured astrocytes

First, I confirmed the mRNA expression of dopamine receptor and α- and ß-AR subtypes in cultured astrocytes, bands of all receptor subtypes were detected (Figure 15). Next, I examined the effects of monoamines (dopamine, serotonin, histamine) on the mRNA levels of cytokines (*Il6, Il1b, Tnf*) and growth factors (*Fgf2, Bdnf, Ngf*). Treatment with dopamine for 1 hour (but not 3 hours) increased IL-6 mRNA levels in cultured astrocytes (Figure 16A). Conversely, serotonin and histamine (10 μM) did not affect the mRNA levels of any of the factors (Figure 16A-F) and dopamine (10 μM) did not affect the mRNA levels of any of the factors except IL-6 (Figure 16B-F).

3.2 Dopamine at low and high concentrations increases IL-6 mRNA levels and release via D1-like receptors and ß-adrenoceptors, respectively

I investigated which receptors are involved in the dopamine-induced increase in IL-6 mRNA levels. High dopamine concentrations also act on ß-ARs (Koppel *et al.*, 2018). Therefore, the concentration-response relationships between dopamine and IL-6 mRNA levels in the presence of the ß-AR antagonist propranolol were investigated. Treatment of cultured astrocytes with dopamine (1 nM–100 μM) increased IL-6 mRNA levels in a concentration-dependent manner (Figure 17A). Propranolol (10 μM) inhibited the increase in IL-6 mRNA levels induced by a high concentration of dopamine (100 μM) but not that induced by a low concentration of dopamine (1 μM). Dopamine (1 μM) significantly increased the IL-6 mRNA levels (Figure 17B). In the following experiments, 1 μM dopamine was used as the lowest concentration that significantly increased IL-6 mRNA levels, while 100 μM dopamine was used as the high concentration of dopamine that was significantly inhibited by propranolol. The D1-like receptor antagonist SCH23390 (10 μM) but not the D2-like receptor antagonist haloperidol (10 μM) inhibited the increase in IL-6 mRNA levels at 1 μM dopamine (Figure 17B). The increase in IL-6 mRNA levels at 100 μM dopamine was not inhibited by SCH23390, was enhanced by haloperidol (Figure 17C), and was partially inhibited by the $ß_1$-AR antagonist atenolol (10 μM), the $ß_2$-AR antagonist ICI118551 (1 μM), and the $ß_3$-AR antagonist SR59230A (1 μM) (Figure 17D). In the presence of a mixture of atenolol, ICI1118551, and SR59230A, dopamine (100 μM) failed to increase IL-6 mRNA levels. None of the antagonists alone exerted any effect on IL-6 mRNA levels (Figure 17E). Activation of D1-like receptors stimulates adenylate cyclase and phospholipase C (Lee *et al.*, 2004). IL-6 mRNA levels

were increased by the D1-like receptor full agonist SKF81297 (10 μM) and the D1-like receptor adenylyl cyclase agonist SKF83822 (10 μM), but not by the D1-like receptor phospholipase C agonist SKF83959 (10 μM) or the D2-like receptor agonist bromocriptine (10 μM) (Figure 17F). Next, the protein levels of IL-6 released into the culture medium were measured by ELISA. Similar to the effects of dopamine on the IL-6 mRNA levels, the low (1 μM) and high (100 μM) concentrations of dopamine increased the release of IL-6, which were inhibited by SCH23390 and propranolol, respectively (Figure 17G, H). In addition, the release of IL-6 by dopamine (100 μM) was enhanced by haloperidol. These results suggest that a low concentration of dopamine increased IL-6 expression via D1-like receptors, and a high concentration of dopamine regulated that via ß-ARs and D2-like receptors.

3.3 Dopamine promotes CREB phosphorylation via D1-like receptors and ß-adrenoceptors

Transcription of IL-6 is promoted by binding of transcription factors, such as mitogen-activated protein kinase (MAPKs), cAMP response element binding protein (CREB), and signal transducer and activator of transcription 3 (STAT3), to specific DNA sequences and p300/CBP (Karin *et al.*, 1997; Berghe *et al.*, 2000; Du *et al.*, 2020). Here, I investigated whether low and high dopamine concentrations regulate the phosphorylation of proteins involved in transcription. Dopamine (1 μM for 30 minutes) promoted CREB phosphorylation, which was inhibited by SCH23390 but not by haloperidol or propranolol (Figure 18A). Dopamine (100 μM for 30 minutes) also promoted CREB phosphorylation, which was inhibited by SCH23390, haloperidol, and propranolol (Figure 18B). SKF81297, the ß-AR agonist isoproterenol, and the adenylyl cyclase activator forskolin promoted CREB phosphorylation (Figure 18C). Dopamine exerted no effect on STAT3 or MAPKs; namely extracellular signal-regulated kinase (ERK), c-Jun N-terminal kinase (JNK), and p38 phosphorylation at low or high concentrations (Figure 18D-G). These results suggest that low and high concentrations of dopamine increased IL-6 mRNA levels by CREB phosphorylation following D1-like receptors and ß-ARs activation, respectively.

3.4 Activation of α_1- and ß-adrenoceptors increases IL-6 mRNA levels

I next examined the effects of adrenoceptor subtypes, since dopamine increased IL-6 mRNA levels via ß-ARs. Treatment of either noradrenaline or isoproterenol for 3 hours increased IL-6 mRNA levels in a concentration-dependent manner (Figure 19A).

The maximum increase in the IL-6 mRNA levels was higher in response to noradrenaline than that it was to isoproterenol. The noradrenaline-induced increase in the IL-6 mRNA levels was inhibited by the α_1-antagonist prazosin (1 μM), the α_2-antagonist atipamezole (10 μM), and propranolol (10 μM) (Figure 19B). Co-treatment with prazosin and propranolol abolished the noradrenaline-induced increase in the IL-6 mRNA levels. Additional treatment with atipamezole did not cause further inhibition. None of the antagonists alone had any effect on IL-6 mRNA levels (Figure 19C). In addition to isoproterenol (1 μM), the IL-6 mRNA levels were increased by the α_1-agonist phenylephrine (1 μM) but not by the α_2-agonist dexmedetomidine (1 μM) (Figure 19D). These results suggest that α_1- and ß-ARs activation increased IL-6 mRNA levels.

3.5 Activation of ß-adrenoceptors increases IL-6 mRNA levels via cAMP/PKA/CREB pathway

In general, ß-ARs coupled to Gs proteins activate the cAMP/protein kinase A (PKA) pathway. The isoproterenol-induced increase in the IL-6 mRNA level was inhibited by the PKA inhibitor H89 (5 μM), but not by the protein kinase C (PKC) inhibitor BIM (5 μM) (Figure 20A). Forskolin (10 μM) also increased the IL-6 mRNA level (Figure 20B). PKA activates CREB, which regulates the expression of a variety of genes (Berghe *et al.*, 2000). Isoproterenol increased CREB phosphorylation 30 minutes after treatment (Figure 20C). In the presence of propranolol or H89, isoproterenol did not increase CREB phosphorylation. Forskolin also increased CREB phosphorylation. Isoproterenol decreased ERK phosphorylation, which was blocked by propranolol (Figure 20D). On the other hand, isoproterenol did not affect JNK, p38, and STAT3 phosphorylation (Figure 20E-G). Like isoproterenol, forskolin (10 μM) and the MEK/ERK inhibitor U0126 (10 μM) also decreased ERK phosphorylation (Figure 20D). U0126 alone did not affect IL-6 mRNA levels (Figure 21C). These results suggest that the cAMP/PKA/CREB pathway was involved in the increase in IL-6 mRNA level following ß-AR activation.

3.6 Activation of α_1-adrenoceptors increases IL-6 mRNA levels via PKC/ERK pathway

α_1-ARs coupled to Gq proteins activate the Ca^{2+}/PKC pathway, which increases MAPKs phosphorylation (Naor *et al.*, 2000). Therefore, I investigated whether PKC and/or MAPKs regulate IL-6 mRNA levels following α_1-AR activation. The phenylephrine-induced increase in the IL-6 mRNA level was inhibited by BIM, but not

by H89 (Figure 21A). Phenylephrine did not affect CREB phosphorylation (Figure 21B). U0126 (10 μM) abolished the phenylephrine-induced increase in the IL-6 mRNA level (Figure 21C). Phenylephrine increased ERK phosphorylation (Figure 21D). In the presence of prazosin, BIM, or U0126, phenylephrine did not increase ERK phosphorylation. On the other hand, phenylephrine did not affect JNK, p38, and STAT3 phosphorylation (Figure 20G, 21E, F). These results suggest that the PKC/ERK pathway was involved in the increase in IL-6 mRNA level following α_1-AR activation.

3.7 Noradrenaline increases IL-6 mRNA levels via MAPKs and PKA

Noradrenaline increased ERK and JNK phosphorylation but not p38, and these increases were inhibited by prazosin (Figure 21D-F). Therefore, I investigated whether ERK or JNK phosphorylation affects the noradrenaline-induced increase in the IL-6 mRNA levels. U0126 and the JNK inhibitor SP600125 (10 μM) suppressed the noradrenaline-induced ERK and JNK phosphorylation (Figure 22A, B). Furthermore, U0126 and SP600125 abolished the noradrenaline-induced IL-6 increase (Figure 22C). SP600125 alone did not have any effect on IL-6 mRNA level (Figure 22D). Moreover, H89 abolished the noradrenaline-induced IL-6 increase (Figure 22E). These results suggest that both cAMP/PKA and ERK and/or JNK pathways were involved in the noradrenaline-induced increase in the IL-6 mRNA levels.

3.8 Astrocyte conditioned medium increases IL-6 mRNA levels via α_2-adrenoceptors

Next, the long-term or indirect effects on IL-6 mRNA levels following adrenoceptor-activation were examined. The treatment of noradrenaline or adrenoceptor-agonists for 24 hours did not have any effect on IL-6 mRNA levels (Figure 23A). Then, I examined whether some factors released by adrenoceptor activation are involved in IL-6 mRNA levels. The 3-hour treatment of ACM, derived from the ACM-donor cells treated with noradrenaline or dexmedetomidine but not phenylephrine and isoproterenol, increased IL-6 mRNA levels in the ACM-recipient cells (Figure 23B, C). The effect of dexmedetomidine was abolished by the treatment of atipamezole for the ACM-donor cells (Figure 23D). However, there were no changes in IL-6 mRNA levels in the ACM-donor cells (Figure 23E). These results suggest that α_2-AR activation increased IL-6 mRNA levels via some factors released into the extracellular medium.

3.9 High dopamine concentrations regulate process formation via D2-

like receptors and β- and α_2-adrenoceptors

Next, I investigated the effects of dopamine on astrocytic process formation. Dopamine at 1 μM had no effect on process formation (Figure 24A), whereas dopamine at 100 μM induced process formation (Figure 24B). This effect was inhibited by propranolol but not by SCH23390. Haloperidol and atipamezole (10 μM) enhanced dopamine-induced process formation. The effect of dopamine (100 μM) was partially inhibited by atenolol, ICI118551, and SR59230A (Figure 24C). SKF81297, SKF83822, isoproterenol, and forskolin, but not SKF83959 and bromocriptine, induced process formation (Figure 24D, E). These results suggest that D1-like receptor and β-AR activation induced process formation while D2-like receptor and α_2-AR activation inhibited that.

3.10 D1-like receptor and β-adrenoceptor agonists increase GFAP expression and change astrocytic morphology in acute hippocampal slices

I investigated whether activating dopamine receptors affects astrocytic morphology in acute hippocampal slices in addition to cultured astrocytes. Dopamine, SKF81297, and isoproterenol (10 μM for 90 minutes) increased the mean intensity of GFAP expression (Figure 25A, B). Astrocytes treated with these drugs displayed increases in the total branch length and the number of branches, but not the average branch length (Figure 25C-E). In addition, the Sholl analysis showed increases in intersections and shifts in the curve to the right, which indicates an enhanced complexity of astrocytic processes (Figure 25F). Dopamine changed morphology in astrocytes of slice tissue as well as in cultured astrocytes via β- and D1-like receptors.

II-4 Discussion

In Chapter II, I found that D1- and D2-like receptors and α_1-AR, in addition to ß-ARs, regulate IL-6 expression, which involves CREB and ERK phosphorylation, in cultured astrocytes. Furthermore, D1- and D2-like receptors and α_2-AR, in addition to ß-ARs, regulate astrocytic morphology. Especially, the high concentrations of dopamine regulate these effects via α- and ß-ARs in addition to dopamine receptors. Furthermore, bidirectional regulation was observed, *i.e.*, the effects of D1-like receptors and ß-ARs were negatively regulated by D2-like receptors and α_2-ARs (Figure 26).

Concentrations of monoamines *in vivo*

It is likely that the concentrations of dopamine (1–100 μM) and noradrenaline (100 nM–1 μM), which increased in IL-6 mRNA levels in this study, and of dopamine (100 μM), which induced process formation, could be reached, at least transiently, under physiological and pathological *in vivo* conditions. The concentration of dopamine in human cerebrospinal fluid *in vivo* has been reported to be 39.5 ± 19.8 nM (Strittmatter *et al.*, 1997), while the concentration of dopamine in the synaptic gap reaches 10–100 μM (Cragg and Rice, 2004; Koppel *et al.*, 2018). The physiological concentration of noradrenaline in cerebrospinal fluid is 1 nM to 100 nM (Globus *et al.*, 1989). Under pathological conditions, such as acute stress and ischemic conditions dopamine and noradrenaline concentrations increase (Globus *et al.*, 1989; Baker *et al.*, 1991; Chang *et al.*, 1993; Pascucci *et al.*, 2007). Furthermore, dopamine and noradrenaline levels in the brain are increased several-fold in mice with LPS *i.p.* injection (Mori *et al.*, 2003; Sekio and Seki, 2015).

Effects of monoamines on IL-6 expression

Dopamine at low and high concentrations transiently increased IL-6 mRNA levels in a concentration-dependent manner. Dopamine-induced increases in IL-6 mRNA levels were accompanied by CREB phosphorylation, which was abolished by the D1-like receptor antagonist (when 1 μM dopamine was used) and the ß-antagonist (when 100 μM dopamine was used). Furthermore, the D1-like receptor adenylyl cyclase agonist SKF83822, but not the D1-like receptor phospholipase C agonist SKF83959, increased IL-6 mRNA levels. The ß-agonist and the adenylyl cyclase activator also increased IL-6 mRNA levels. These results suggest that low dopamine concentrations act via the D1-like receptor/cAMP/CREB pathway, whereas high dopamine concentrations act via the

ß-AR/cAMP/CREB pathway to activate IL-6 transcription. In contrast, under some antagonist treatment conditions, IL-6 mRNA levels did not correlate with CREB phosphorylation. Although the D1-like receptor antagonist partially decreased dopamine (100 μM)-induced CREB phosphorylation, it had no effect on IL-6 mRNA levels. These effects are likely due to the potent effect of dopamine via ß-ARs, and CREB phosphorylation above a certain level may not contribute to the increase in IL-6 mRNA levels. Furthermore, the D2-like receptor antagonists further enhanced dopamine (100 μM)-induced IL-6 mRNA increases, suggesting that D2-like receptors exert a suppressive effect on IL-6 transcription in the presence of high dopamine concentrations. Contrary to this result, D2-like receptor antagonists suppressed dopamine (100 μM)-induced CREB phosphorylation. Therefore, other pathways are likely to be involved in this suppressive effect.

The D2-like receptor antagonist had no effects on IL-6 mRNA levels stimulated by a low concentration of dopamine, not by a high concentration. D2-like receptors have a higher affinity for dopamine (Seeman and Grigoriadis, 1987); however, D2-like receptor expression is lower than D1-like receptor expression in at least 21 brain regions (Richfield *et al.*, 1989). In a simulation with model parameters for dopamine receptors in striatal neurons, the amount of dopamine binding to D2-like receptors was approximately 10 times lower than that to D1-like receptors in the presence of 1 μM dopamine (Hunger *et al.*, 2020). The D2-like receptor antagonist may not have exerted any effect because of the low numbers of D2-like receptors available for dopamine binding.

The maximum effect of noradrenaline on IL-6 mRNA transcription was higher than that of isoproterenol. Noradrenaline has a higher affinity for α-ARs than ß-ARs (Arnsten, 2000). The effect of noradrenaline on IL-6 transcription was suppressed by both α_1- and ß-antagonists, and the α_1-agonist phenylephrine also activated the IL-6 transcription. These results indicate that α_1-ARs are involved in the transcriptional activation of IL-6 in astrocytes. Phenylephrine activated ERK and IL-6 transcription, both of which were suppressed by the PKC and ERK inhibitors. Phenylephrine also did not affect CREB, JNK, and p38 phosphorylation. These results indicate that α_1-ARs activate IL-6 transcription via the PKC/ERK pathway in astrocytes. Meanwhile, isoproterenol activated CREB and IL-6 transcription, both of which were suppressed by the PKA inhibitor. The adenylate cyclase activator forskolin mimicked the action of isoproterenol. These results indicate that ß-ARs activate IL-6 transcription via the cAMP/PKA/CREB pathway. Moreover, the noradrenaline-activated transcription of IL-6

was inhibited by both the ERK inhibitor and the JNK inhibitor. The phosphorylation of ERK or JNK activates common factors, such as c-jun and Elk (Shaulian and Karin, 2001), which may be also involved in IL-6 transcription. Noradrenaline-activated transcription of IL-6 was also inhibited by the PKA inhibitor. Therefore, the pathway of noradrenaline-activated IL-6 transcription is likely to include the pathways activated by phenylephrine and isoproterenol. Furthermore, in contrast to this study, it has been shown that isoproterenol suppresses LPS-induced IL-6 promoter activities via β_2-ARs in astrocytes (Nakamura *et al.*, 1998). LPS-induced IL-6 transcriptional activation is mediated via the TLR4-nuclear factor-kappa B (NF-κB) pathway (Hung *et al.*, 2016; Zhang *et al.*, 2016), and the activation of β-ARs attenuates NF-κB activity by increasing IκBα gene expression and protein levels (Gavrilyuk *et al.*, 2002). In the presence of LPS, β-ARs may suppress IL-6 transcription by potent suppressing NF-κB. Therefore, it is likely that the activation of β-ARs shows bidirectional effects on IL-6 transcription via the CREB and NF-κB pathways.

The α_2-antagonist atipamezole suppressed the effect of noradrenaline on IL-6, whereas the treatment of the α_2-agonist dexmedetomidine showed no effect. Furthermore, the effect of noradrenaline on IL-6 transcription was completely suppressed by co-treatment with α_1- and β-AR antagonists, indicating that noradrenaline activates IL-6 transcription mainly via α_1- and β-ARs. One of the possible explanations for this discrepancy between the agonist's and antagonist's effects is that the mechanisms involved in the activation of one receptor subtype by a specific agonist are different from the mechanisms involved in the activation of multiple receptor subtypes by noradrenaline. For example, β_1- and α_{2A}, or α_{1A}- and α_{1B}-ARs form receptor-heterodimers (Stanasila *et al.*, 2003; Xu *et al.*, 2003). When only one receptor from the heterodimer is activated, the intracellular signaling of the heterodimer is different to the signaling seen when both receptors in the heterodimer are activated (Jordan and Devi, 1999; Jordan *et al.*, 2003). This could provide an explanation for why noradrenaline-increased JNK phosphorylation was suppressed by prazosin, while exerting no effect of phenylephrine on the JNK phosphorylation. Further investigations are needed to reveal these mechanisms.

ACM derived from noradrenaline- or dexmedetomidine-treated astrocytes increased IL-6 mRNA levels in the ACM-recipient cells. It is possible that factor(s), released into the extracellular medium by activation of α_2-ARs, may promote IL-6 transcription in neighboring and distant astrocytes. Activation of astrocytic α_2-ARs increases accumulation of glutamine, as a precursor of neurotoxic glutamate (Huang and

Hertz, 2000), and activation of metabotropic glutamate receptors enhances the release or transcription of IL-6 in astrocytes (Aronica *et al.*, 2005; Shah *et al.*, 2012). In addition, the effect of released factor(s) may disappear within a few hours, because there were no changes in IL-6 mRNA levels in the ACM-donor cells. Further studies are needed to elucidate the indirect pathway of IL-6 transcriptional activation via the α_2-ARs.

Effects of monoamines on astrocytic process formation

Dopamine (100 μM) induced astrocytic process formation, which was abolished by a β-antagonist. Conversely, an α_2-antagonist enhanced dopamine-induced process formation. The activation of β-ARs induces astrocytic process formation via cAMP signaling (Kitano *et al.*, 2021), and the dephosphorylation of myosin light chains by down-regulation of the Rho pathway is involved in the mechanism of intracellular cAMP-induced process formation (Rodnight and Gottfried, 2013). Meanwhile, the activation of α_2-ARs inhibits both cAMP-dependent and -independent astrocytic process formation (Kitano *et al.*, 2021). Furthermore, I found that dopamine or the D1-like receptor agonist changed astrocytic morphology and upregulated GFAP expression in acute hippocampal slices, suggesting that dopamine receptors are involved in modulating astrocytic morphology *in vivo* not only *in vitro*. IL-6 upregulation may contribute to dopamine-induced morphological changes in astrocytes. However, it has been reported that the morphology of astrocytes in GFAP-IL6 transgenic mice does not differ from that in normal mice, even though GFAP-IL6 transgenic mice exhibit high IL-6 expression in astrocytes (Penkowa *et al.*, 2003). Therefore, IL-6 is not likely to exert effects on astrocytic morphology.

Dopamine receptors and adrenoceptors can form homodimers and heterodimers (Franco *et al.*, 2000). As discussed above, the dimerization may lead to different properties from the monomers. For example, D2-like receptors and β_2-ARs form homodimers, which transduce enhanced signals compared to monomers (Hebert *et al.*, 1996; Wouters *et al.*, 2019). Furthermore, D2-like receptors form heterodimers with β_2-ARs and enhance adenylate cyclase activity when stimulated by dopamine (Watts and Neve, 1997; Rebois *et al.*, 2012). A dopamine D_2 receptor antagonist decreases the level of D2-like receptor dimer formation (Wouters *et al.*, 2019). In addition, an adenosine A_1 receptor antagonist enhances the activation of the dopamine D_1 receptor coupled with the A_1 receptor (Franco *et al.*, 2000). Therefore, the antagonists used in this study may affect not only monomeric receptors but also receptor complexes. Further studies are needed to address this issue.

Role of monoamines in diseases

In the present study and the previous report (Kitano *et al.*, 2021), the concentrations of dopamine and noradrenaline that induced astrocytic process formation were about 10 times higher than those that increased IL-6 expression. The effect of monoamines on the pathophysiology may be different depending on their concentrations. IL-6 has been widely reported to play a beneficial role in brain function, e.g., by acting as a neurotrophic factor (Wagner, 1996), suppressing neuronal cell death (Day *et al.*, 2014), and improving learning and memory impairment after traumatic brain injury (Willis *et al.*, 2020). The D1-like agonist SKF83959 is suggested to protect nigral neurons from MPTP neurotoxicity via astrocytic D1-like receptors (Zhang *et al.*, 2009). The activation of astrocytic D1-like receptors enhances the recovery of brain function after experimental stroke (Kuric *et al.*, 2013). In addition, astrocytic β_2-ARs mediate hippocampal long-term memory consolidation (Gao *et al.*, 2016). As IL-6 and these monoamine receptors appear to contribute to recovery from various diseases, the effects of low dopamine and noradrenaline concentrations on IL-6 expression may be beneficial. Conversely, high dopamine and noradrenaline concentrations are likely to cause CNS inflammation and induce reactive astrocytes. In this study, dopamine (100 μM) and a β-agonist induced morphological changes in astrocytic cultures and acute brain slices, and increased GFAP expression in astrocytes in acute brain slices. These characteristics are consistent with those of reactive astrocytes in CNS inflammation, including elongated and complex processes and increased GFAP expression (Pekny and Pekna, 2014). These monoamine and IL-6 levels increase under ischemic conditions (Baker *et al.*, 1991; Chang *et al.*, 1993; Clark *et al.*, 1999). In addition, astrocytes upregulate β-ARs and downregulate α_2-ARs in neurodegenerative diseases (Shao and Sutin, 1992; Mantyh *et al.*, 1995). Thus, the inhibitory role of D2-like receptors and α_2-ARs in astrocytes under extremely elevated dopamine and noradrenaline levels may contribute to improving such pathological conditions. Further studies are needed to reveal whether astrocytic dopamine receptors and adrenoceptors regulate IL-6 expression *in vivo* and how the astrocytic process and IL-6 act under physiological and pathological conditions.

II-5 Summary

Catecholamines, such as dopamine and noradrenaline, levels in the CNS change under pathological conditions such as Parkinson's disease, Alzheimer's disease, and ischemia. In addition, mice treated intraperitoneally with LPS have increased levels of catecholamines in the brain. Under those pathological conditions, astrocytes become reactive astrocytes characterized by morphological changes and the release of proinflammatory cytokines involved in pathogenesis. However, it remains unclear whether catecholamines regulate astrocytic morphology and cytokine production via catecholamine receptors other than ß-ARs. In Chapter II, I investigated the effects of dopamine and noradrenaline on IL-6 expression and process formation and their intracellular mechanisms in rat primary cultured astrocytes. Dopamine increased IL-6 expression in a concentration-dependent manner, and this was accompanied by CREB phosphorylation. The effects of a low dopamine concentration (1 μM) were inhibited by a D1-like receptor antagonist, whereas the effects of a high dopamine concentration (100 μM) were inhibited by a ß-antagonist and enhanced by a D2-like receptor antagonist. The α_1-agonist phenylephrine, and the ß-agonist isoproterenol increased IL-6 mRNA levels. The phenylephrine-induced IL-6 increase was accompanied by an increase in ERK phosphorylation, and these effects were blocked by inhibitors of PKC and ERK. The isoproterenol-induced IL-6 increase was accompanied by an increase in CREB phosphorylation, and these effects were blocked by a PKA inhibitor. These results indicate that low and high concentrations of dopamine increased IL-6 mRNA levels by CREB phosphorylation following D1-like receptors and ß-ARs activation, respectively. In addition, IL-6 increases by α_1- and ß-ARs were mediated via the PKC/ERK and cAMP/PKA/CREB pathways, respectively. Furthermore, dopamine (100 μM) and the D1-like receptor agonist promoted process formation, which was inhibited by a ß-antagonist and enhanced by both an α_2-antagonist and the D2-like receptor antagonist. These results indicated that D1- and D2-like receptors and α_2-AR, in addition to ß-ARs, regulate astrocytic morphology. In conclusion, high dopamine concentrations regulate these effects via α- and ß-ARs in addition to dopamine receptors. Furthermore, I observed bidirectional regulation, *i.e.*, the effects of D1-like receptors and ß-ARs were negatively regulated by D2-like receptors and α_2-ARs. These findings will help us to understand the pathogenesis of neurodegenerative diseases caused by abnormal signaling via catecholamine receptors.

II-6 Figures and tables

Table 3. Primer sequences used for quantitative PCR.

Gene name	Gene symbol	Product size (bp)	Annealing temperature (°C)	Sequence (5'->3') (upper: forward; lower: reverse)
interleukin 6	*Il6*	145	61	GATTGTATGAACAGCGATGATGC AGAAACGGAACTCCAGAAGACC
interleukin 1beta	*Il1b*	150	63	TTGCTTCCAAGCCCTTGACT CTCCACGGGCAAGACATAGG
tumor necrosis factor	*Tnf*	125	63	CATGAGCACGGAAAGCATGA CCACGAGCAGGAATGAGAAGA
brain-derived neurotrophic factor	*Bdnf*	55	63	GGCCCAACGAAGAAAACCAT AGCATCACCCGGGAAGTGT
nerve growth factor	*Ngf*	115	61	CAACAGGACTCACAGGAGCA GTCCGTGGCTGTGGTCTTAT
fibroblast growth factor 2	*Fgf2*	165	63	ATCACTTCGCTTCCCGCA TTTGACGTGTGGGTCGCT
glyceraldehyde-3-phosphate dehydrogenase	*Gapdh*	74	61	GCAAGAGAGAGGCCCTCAG TGTGAGGGAGATGCTCAGTG

Table 4. Primer sequences used for non-quantitative PCR.

Gene nama	Gene symbol	Product size (bp)	Annealing temperature (°C)	Sequence (5'->3') (upper: forward; lower: reverse)
adrenoceptor alpha 1A	*Adra1a*	104	60	AGAAGAAAGCTGCCAAGACG GAAATCCGGGAAGAAAGACC
adrenoceptor alpha 1B	*Adra1b*	138	60	TCTTATGTTGGCTCCCCTTC ACGGGTAGATGATGGGATTG
adrenoceptor alpha 1D	*Adra1d*	165	60	TGAGGCTGCTCAAGTTTTCC GCCAGAAGATGACCTTGAAGAC
adrenoceptor alpha 2A	*Adra2a*	176	60	TTCCTGAGAGGGAAGGGATT AGTTACTGGGGCAAGTGGTG
adrenoceptor alpha 2B	*Adra2b*	147	60	AATTCTCTGAACCCCCAAGC CAAGTTGGGAAGACAACCAG
adrenoceptor alpha 2C	*Adra2c*	150	60	GGTTTCCTCATCGTTTTCA GAAAAGGGCATGACCAGTGT
adrenoceptor beta 1	*Adrb1*	248	60	GCTCTGGACTTCGGTAGACG ACTTGGGGTCGTTGTAGCAG
adrenoceptor beta 2	*Adrb2*	208	60	AGCCACCTACGGTCTCTGAA GTCCCGTTCCTGAGTGATGT
adrenoceptor beta 3	*Adrb3*	150	60	TCGTCTTCTGTGCAGCTACG ATGGTCCTTCATGTGGGAAA
dopamine receptor D1	*Drd1*	136	68	GTCTGTCCTTATATCCTTCATCCC ATACGTCCTGCTCAACCTTG
dopamine receptor D2	*Drd2*	141	64	TGCCATTGTTCTCGGTGTGTTC TTGACGGCACTGTTGACATAGC
dopamine receptor D3	*Drd3*	270	68	TCTGCTCCATCTCCAACCCTGA TGTGCTCCATTTGTCCTGTGGC
dopamine receptor D4	*Drd4*	151	68	GGTGCTGGTGTTGCCTCTCTTTG AGCCACAAACCTGTCCACGCTG
dopamine receptor D5	*Drd5*	192	68	CGTGGAGCCTATGAACCTGACC GCTGACACAAGGGAAGCCAGTC
beta-actin	*Actb*	280	60	TGTCACCAACTGGGACGATA ACCCTCATAGATGGGCACAG
glyceraldehyde-3-phosphate dehydrogenase	*Gapdh*	74	61	GCAAGAGAGAGGCCCTCAG TGTGAGGGAGATGCTCAGTG

Table 5. Antibodies used for western blotting.

Target protein	Dilution	Host animal	Catalog number	Supplier
ERK 1/2	1:2500	Rabbit	4695S	Cell Signaling Technology, Danvers, MA, USA
phospho-ERK 1/2	1:2500	Rabbit	9101S	Cell Signaling Technology
p38	1:2000	Rabbit	9212S	Cell Signaling Technology
phospho-p38	1:1000	Rabbit	9211S	Cell Signaling Technology
SAPK/JNK	1:2500	Rabbit	9252S	Cell Signaling Technology
phospho-SAPK/JNK	1:1500	Rabbit	9251S	Cell Signaling Technology
STAT3	1:4000	Rabbit	4904S	Cell Signaling Technology
phospho-STAT3	1:2000	Rabbit	9145S	Cell Signaling Technology
CREB	1:500	Mouse	sc-377154	Santa Cruz Biotechnology, Santa Cruz, CA, USA
phospho-CREB	1:250	Mouse	sc-81486	Santa Cruz Biotechnology
GAPDH	1:50000	Mouse (peroxidase conjugate)	G9295	Sigma–Aldrich, St. Louis, MO, USA

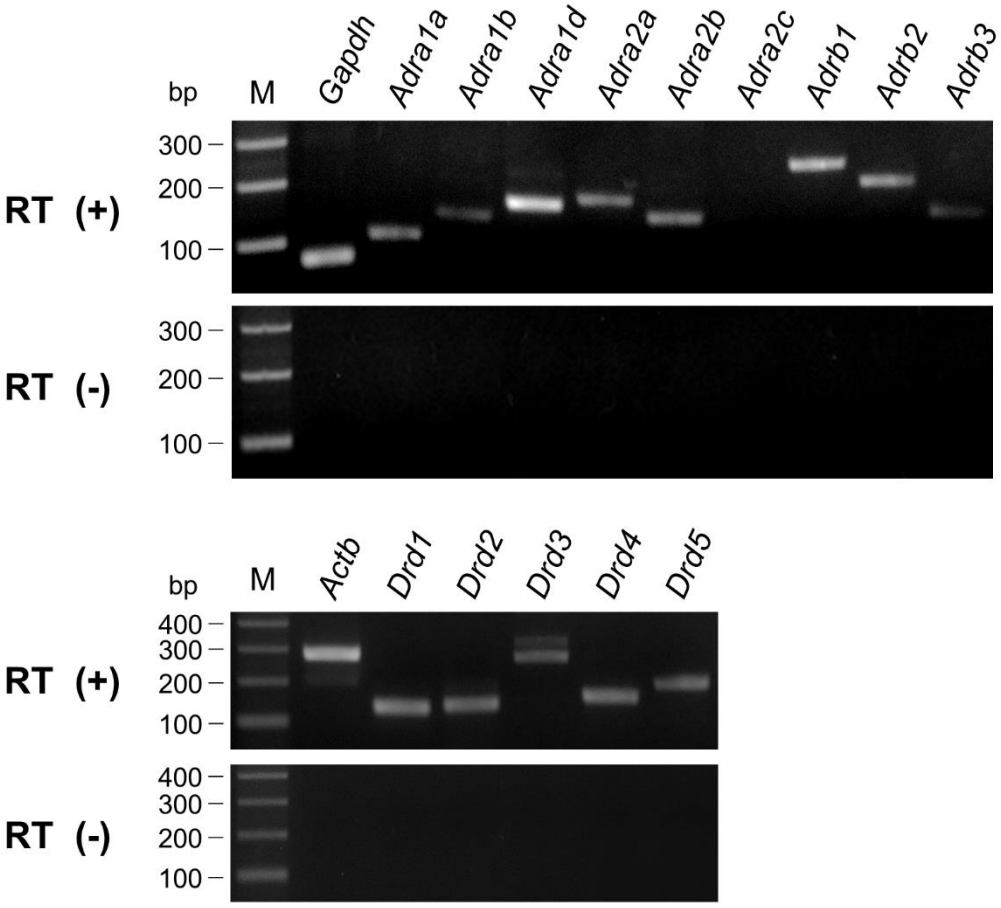

Figure 15. Adrenoceptor and dopamine receptor subtype mRNA expression in the cultured astrocytes.

Bands for all adrenoceptor and dopamine receptor subtypes were detected in the cultured astrocytes. RT (+) and (–) indicates samples reverse-transcribed (+) or not (–), respectively.

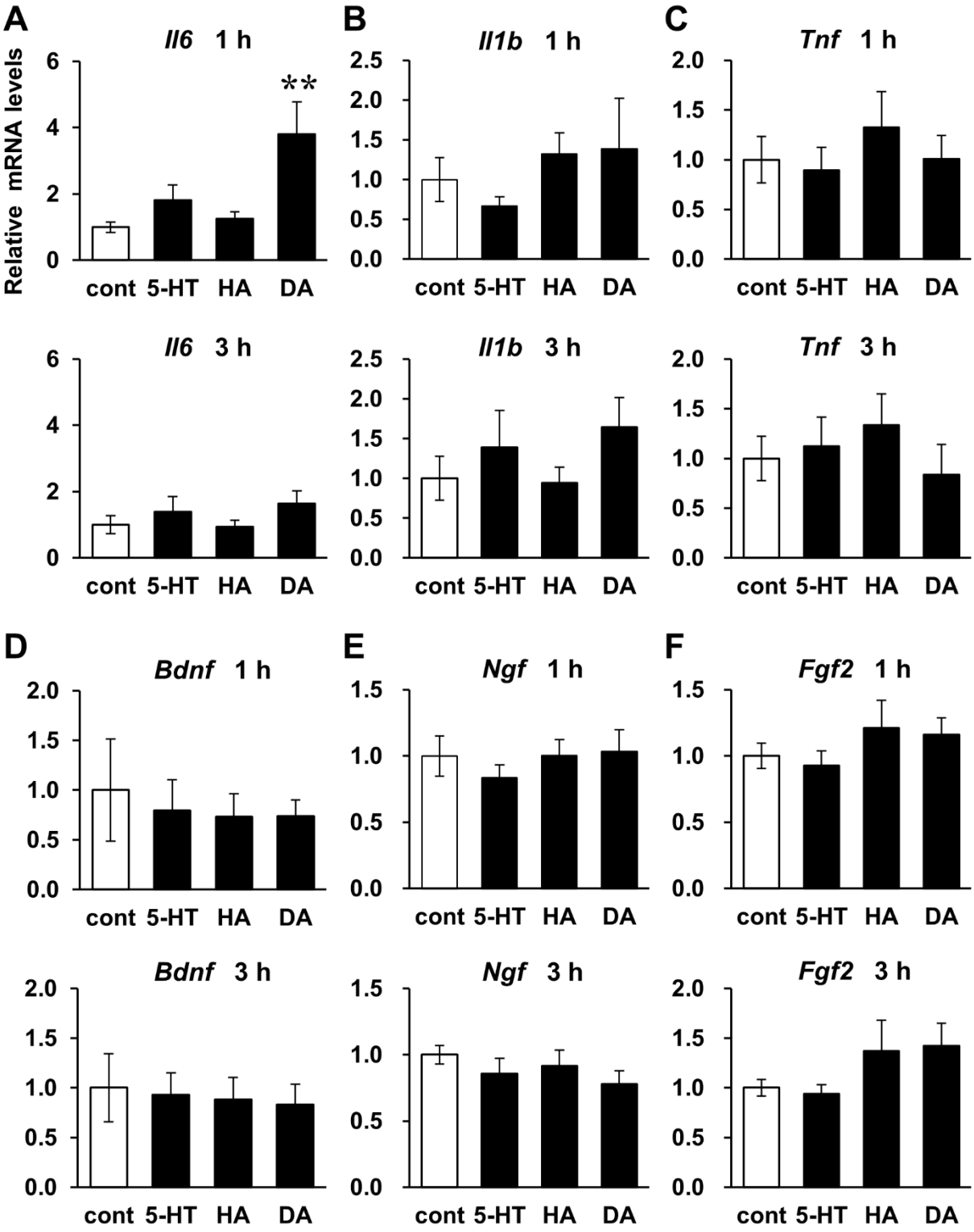

Figure 16. Effects of monoamines on mRNA levels of multiple factors.

(A–F) The mRNA levels of *Il6* (A), *Il1b* (B), *Tnf* (C), *Bdnf* (D), *Ngf* (E), and *Fgf2* (F) in astrocytes treated with serotonin (5-HT, 10 μM), histamine (HA, 10 μM), and dopamine (DA, 10 μM) for 1 and 3 h. The mRNA levels of each factor were normalized to the control level, which was arbitrarily set to a value of "1.0". cont: control. n = 6. $^{**}p < 0.01$ vs. control (Dunnett's test). All data are presented as means ± S.E.M.

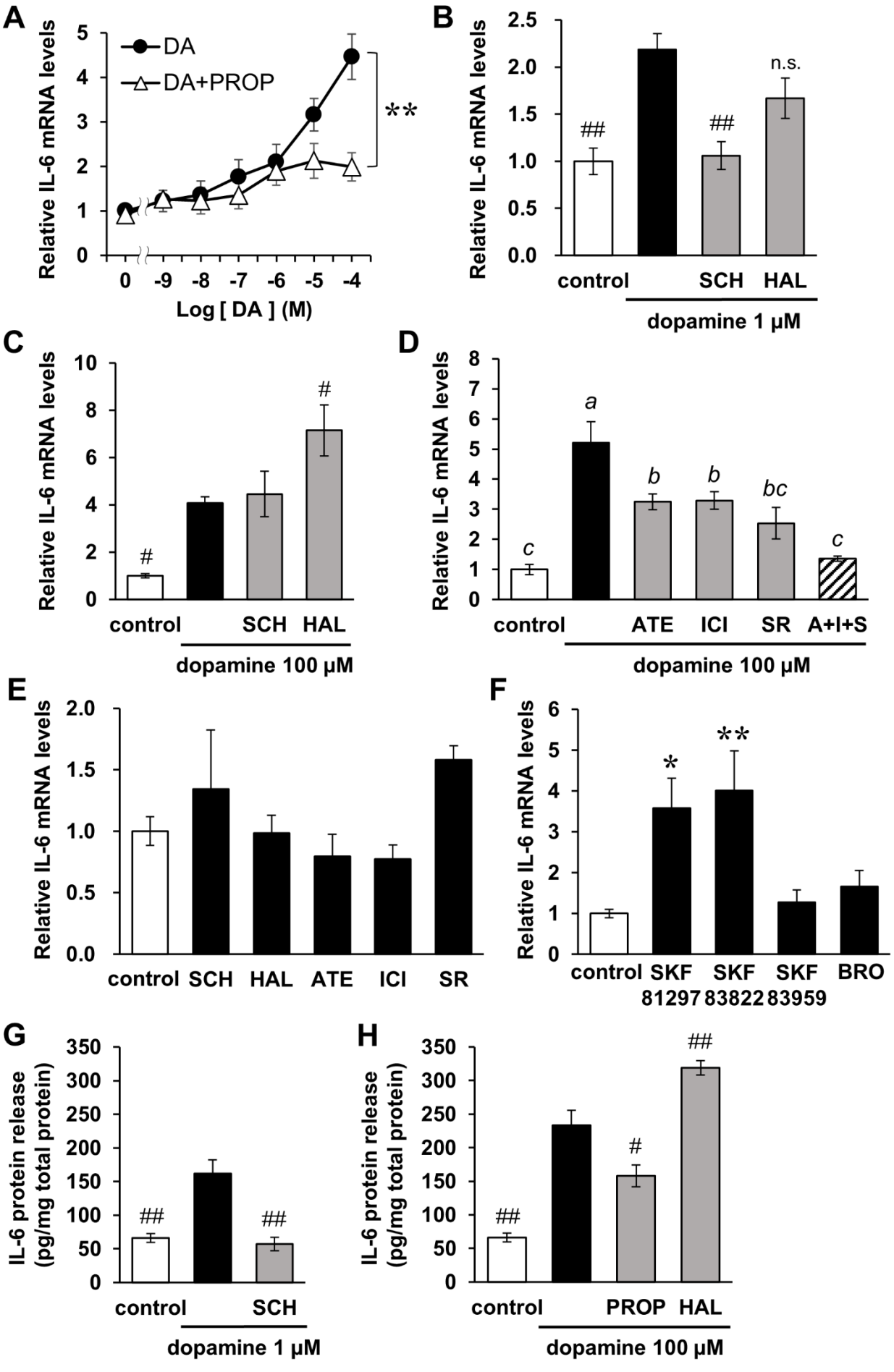
A
Relative IL-6 mRNA levels
DA
DA+PROP
**
Log [DA] (M)
B
Relative IL-6 mRNA levels
n.s.
control
SCH
HAL
dopamine 1 μM
C
Relative IL-6 mRNA levels
control
SCH
HAL
dopamine 100 μM
D
Relative IL-6 mRNA levels
control
ATE
ICI
SR
A+I+S
dopamine 100 μM
E
Relative IL-6 mRNA levels
control
SCH
HAL
ATE
ICI
SR
F
Relative IL-6 mRNA levels
control
SKF 81297
SKF 83822
SKF 83959
BRO
G
IL-6 protein release (pg/mg total protein)
control
SCH
dopamine 1 μM
H
IL-6 protein release (pg/mg total protein)
control
PROP
HAL
dopamine 100 μM

Figure 17. Effects of dopamine receptor and adrenoceptor agonists or antagonists on IL-6 mRNA levels.

(A) IL-6 mRNA levels in astrocytes treated with dopamine (DA, 1 nM to 100 μM) in the presence or absence of the ß-antagonist propranolol (PROP, 10 μM) for 1 h. n = 6. $^{**}p < 0.01$ (unpaired Student's t-test). (B–D) IL-6 mRNA levels in astrocytes treated with DA (B: 1 μM, C, D: 100 μM) in the presence or absence of the D1-like receptor antagonist SCH23390 (SCH, 10 μM), D2-like receptor antagonist haloperidol (HAL, 10 μM), PROP (10 μM), $ß_1$-adrenoceptor antagonist atenolol (ATE, 10 μM), $ß_2$-adrenoceptor antagonist ICI118551 (ICI, 1 μM), and $ß_3$-adrenoceptor antagonist SR59230A (SR, 1 μM) for 1 h. n = 6. n.s.: not significant, $\#p < 0.05$, $\#\#p < 0.01$ vs. DA alone (B, C, Dunnett's test), means with the different letter are significantly different and with the same letter are not significantly different from each other (D, Tukey's t-test). (E) IL-6 mRNA levels in astrocytes treated with SCH, HAL, ATE, ICI, and SR for 2 h. n = 6. vs. control (Dunnett's test). (F) IL-6 mRNA levels in astrocytes treated with the D1-like receptor full agonist SKF81297 (10 μM), D1-like receptor adenylyl cyclase agonist SKF83822 (10 μM), D1-like receptor phospholipase C agonist SKF83959 (10 μM), D2-like receptor agonist bromocriptine (BRO, 10 μM) for 1 h. n = 6. $^{*}p < 0.05$, $^{**}p < 0.01$ vs. control (Dunnett's test). (G, H) IL-6 protein levels of the medium were measured by ELISA. Astrocyte was treated with each drug for 6 h. IL-6 levels were normalized by astrocyte total protein. n = 5. $\#p < 0.05$, $\#\#p < 0.01$ vs. DA alone (Dunnett's test). All data are presented as means ± S.E.M.

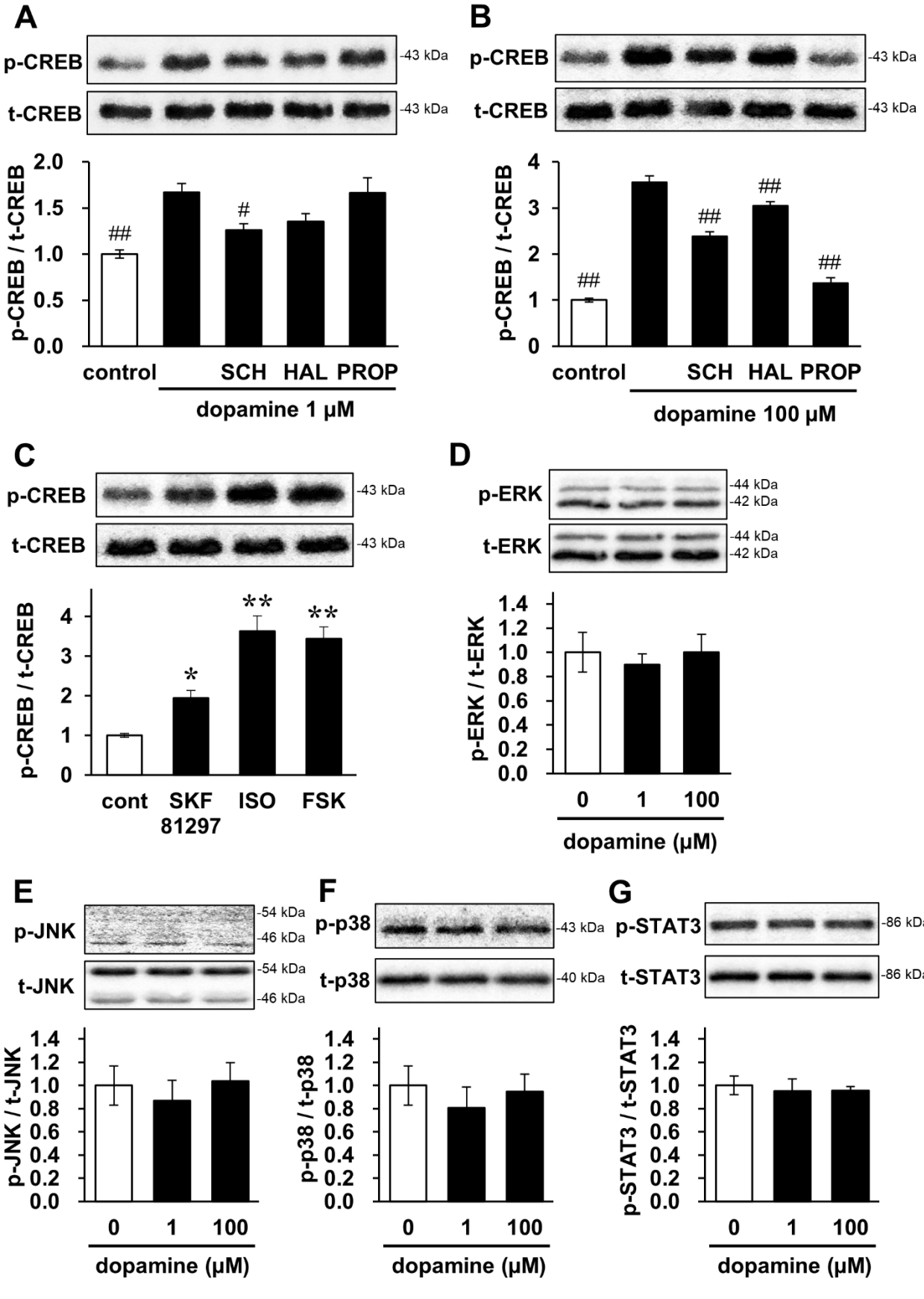
A
p-CREB
t-CREB
-43 kDa
-43 kDa
p-CREB / t-CREB
2.0
1.5
1.0
0.5
0.0
##
#
control
SCH
HAL
PROP
dopamine 1 μM
B
p-CREB
t-CREB
-43 kDa
-43 kDa
p-CREB / t-CREB
4
3
2
1
0
##
##
##
##
control
SCH
HAL
PROP
dopamine 100 μM
C
p-CREB
t-CREB
-43 kDa
-43 kDa
p-CREB / t-CREB
4
3
2
1
0
*
**
**
cont
SKF 81297
ISO
FSK
D
p-ERK
t-ERK
-44 kDa
-42 kDa
-44 kDa
-42 kDa
p-ERK / t-ERK
1.4
1.2
1.0
0.8
0.6
0.4
0.2
0.0
0
1
100
dopamine (μM)
E
p-JNK
t-JNK
-54 kDa
-46 kDa
-54 kDa
-46 kDa
p-JNK / t-JNK
1.4
1.2
1.0
0.8
0.6
0.4
0.2
0.0
0
1
100
dopamine (μM)
F
p-p38
t-p38
-43 kDa
-40 kDa
p-p38 / t-p38
1.4
1.2
1.0
0.8
0.6
0.4
0.2
0.0
0
1
100
dopamine (μM)
G
p-STAT3
t-STAT3
-86 kDa
-86 kDa
p-STAT3 / t-STAT3
1.4
1.2
1.0
0.8
0.6
0.4
0.2
0.0
0
1
100
dopamine (μM)

Figure 18. Effects of dopamine receptor and adrenoceptor agonists/antagonists on CREB, MAPKs, and STAT3 phosphorylation.

(A–C) The protein expression levels of phosphorylated and total CREB were quantified, and representative blots are shown. Astrocytes were treated with dopamine (A: 1 μM, B: 100 μM), D1-like receptor full agonist SKF81297 (10 μM), ß-agonist isoproterenol (ISO, 1 μM), and adenylate cyclase activator forskolin (FSK, 10 μM) in the presence or absence of the D1-like receptor antagonist SCH23390 (SCH, 10 μM), D2-like receptor antagonist haloperidol (HAL, 10 μM), and ß-antagonist propranolol (PROP, 10 μM) for 30 min. cont: control. n = 6. #$p < 0.05$, ##$p < 0.01$ vs. DA alone (A, B, Dunnett's test), *$p < 0.05$, **$p < 0.01$ vs. control (C, Dunnett's test). (D–G) The protein expression levels of phosphorylated and total ERK (D), JNK (E), p38 (F), and STAT3 (G) were quantified, and representative blots are shown. Astrocytes were treated with dopamine (1 or 100 μM) for 10 min (D-F) or 30 min (G). cont: control. n = 6. All data are presented as means ± S.E.M.

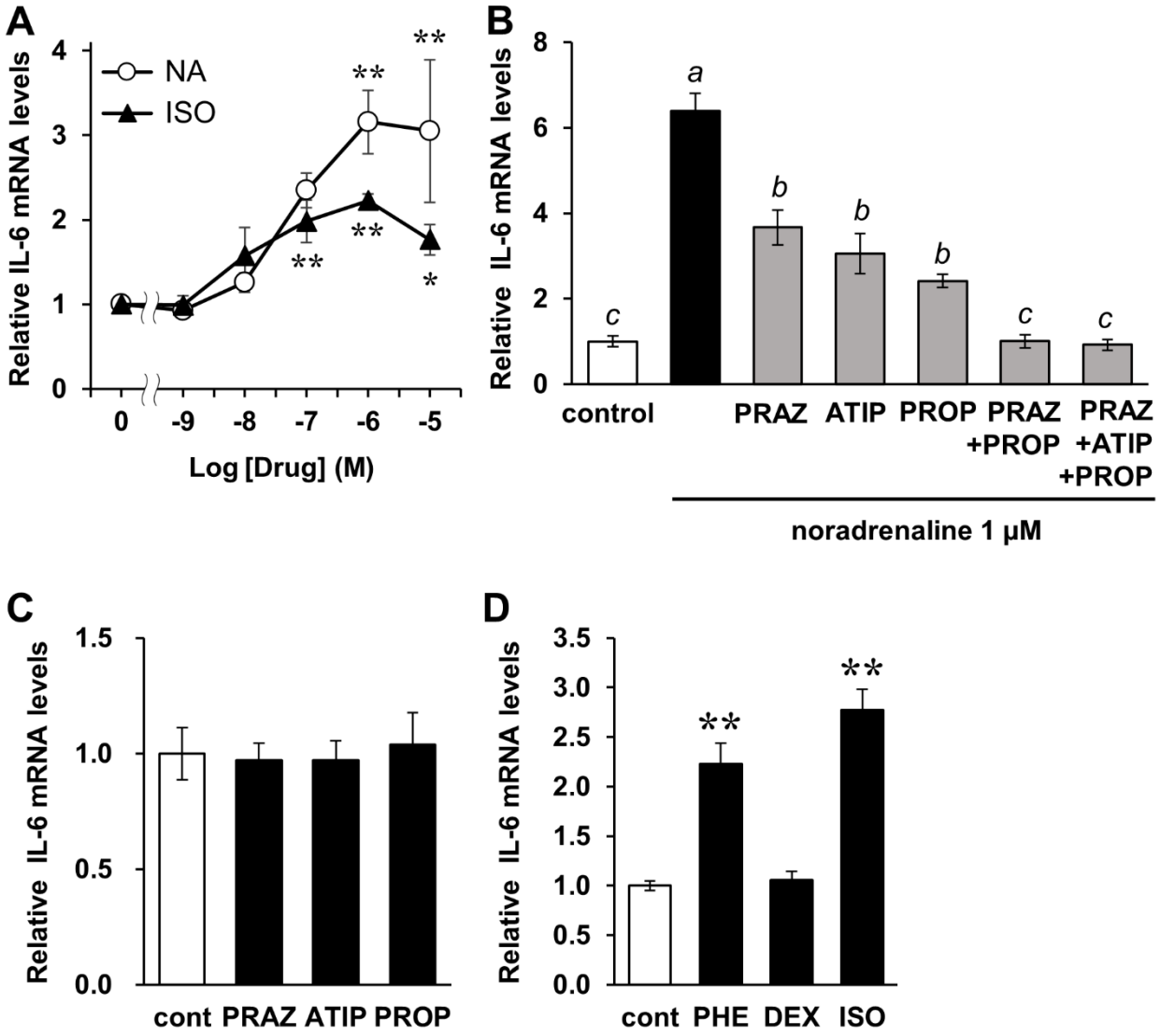

Figure 19. Effects of noradrenaline and adrenoceptor agonists/antagonists on IL-6 mRNA levels.

(A) IL-6 mRNA levels in astrocytes treated with noradrenaline (NA) or the ß-agonist isoproterenol (ISO) (1 nM-10 μM) for 3 h. n = 6. *$p < 0.05$, **$p < 0.01$ vs. control (Dunnett's test). (B) IL-6 mRNA levels in astrocytes treated with NA (1 μM) in the presence or absence of the α_1-antagonist prazosin (PRAZ, 1 μM), the α_2-antagonist atipamezole (ATIP, 10 μM), and the ß-antagonist propranolol (PROP, 10 μM) for 3 h. n = 6. Means with the different letter are significantly different and with the same letter are not significantly different from each other (Tukey's test). (C) IL-6 mRNA levels in astrocytes treated with PRAZ, ATIP, and PROP for 4 h. n = 6. (D) IL-6 mRNA levels in astrocytes treated with the α_1-agonist phenylephrine (PHE, 1 μM), the α_2-agonist dexmedetomidine (DEX, 1 μM), and ISO (1 μM) for 3 h. n = 6. cont: control. **$p < 0.01$ vs. control (Dunnett's test). All data are presented as means ± S.E.M.

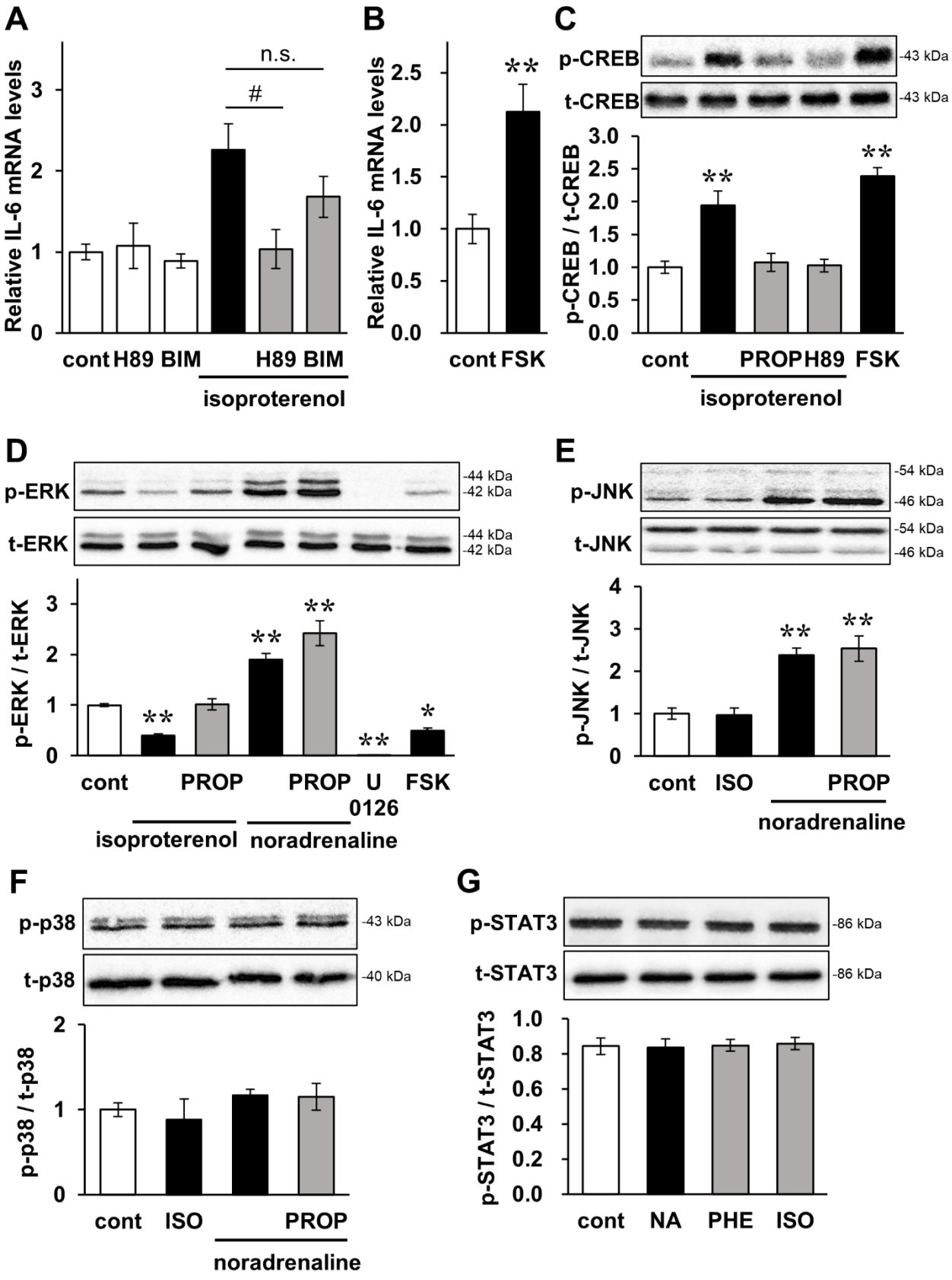
A
Relative IL-6 mRNA levels
n.s.
#
cont H89 BIM H89 BIM
isoproterenol
B
Relative IL-6 mRNA levels
**
cont FSK
C
p-CREB
t-CREB
-43 kDa
-43 kDa
p-CREB / t-CREB
**
**
cont PROP H89 FSK
isoproterenol
D
p-ERK
t-ERK
-44 kDa
-42 kDa
-44 kDa
-42 kDa
p-ERK / t-ERK
cont PROP PROP U 0126 FSK
isoproterenol
noradrenaline
E
p-JNK
t-JNK
-54 kDa
-46 kDa
-54 kDa
-46 kDa
p-JNK / t-JNK
cont ISO PROP
noradrenaline
F
p-p38
t-p38
-43 kDa
-40 kDa
p-p38 / t-p38
cont ISO PROP
noradrenaline
G
p-STAT3
t-STAT3
-86 kDa
-86 kDa
p-STAT3 / t-STAT3
cont NA PHE ISO

Figure 20. Intracellular mechanisms of transcriptional activation of IL-6 via ß-adrenoceptors.

(A, B) IL-6 mRNA levels in astrocytes treated with the ß-agonist isoproterenol (1 μM), the adenylyl cyclase activator forskolin (FSK, 10 μM) in the presence or absence of the PKA inhibitor H89 (5 μM) and the PKC inhibitor BIM (5 μM) for 3 h. cont: control. n.s.: not significant. n = 6. #$p < 0.05$ vs. isoproterenol alone (A, Dunnett's test), **$p < 0.01$ (B, unpaired Student's t-test). (C-G) The protein expression levels of phosphorylated and total CREB (C), ERK (D), JNK (E), p38 (F), STAT3 (G) were quantified, and representative blots are shown. GAPDH was used as a loading control. Astrocytes were treated with α_1-agonist phenylephrine (PHE, 1 μM), the α_2-agonist dexmedetomidine (DEX, 1 μM), isoproterenol (ISO), FSK, or noradrenaline (1 μM) in the presence or absence of the ß-antagonist propranolol (PROP, 10 μM), H89 and the MEK/ERK inhibitor U0126 (10 μM) for 30 min (C, G) or 10 min (D-F). n = 6. *$p < 0.05$, **$p < 0.01$ vs. control (Dunnett's test). All data are presented as means ± S.E.M.

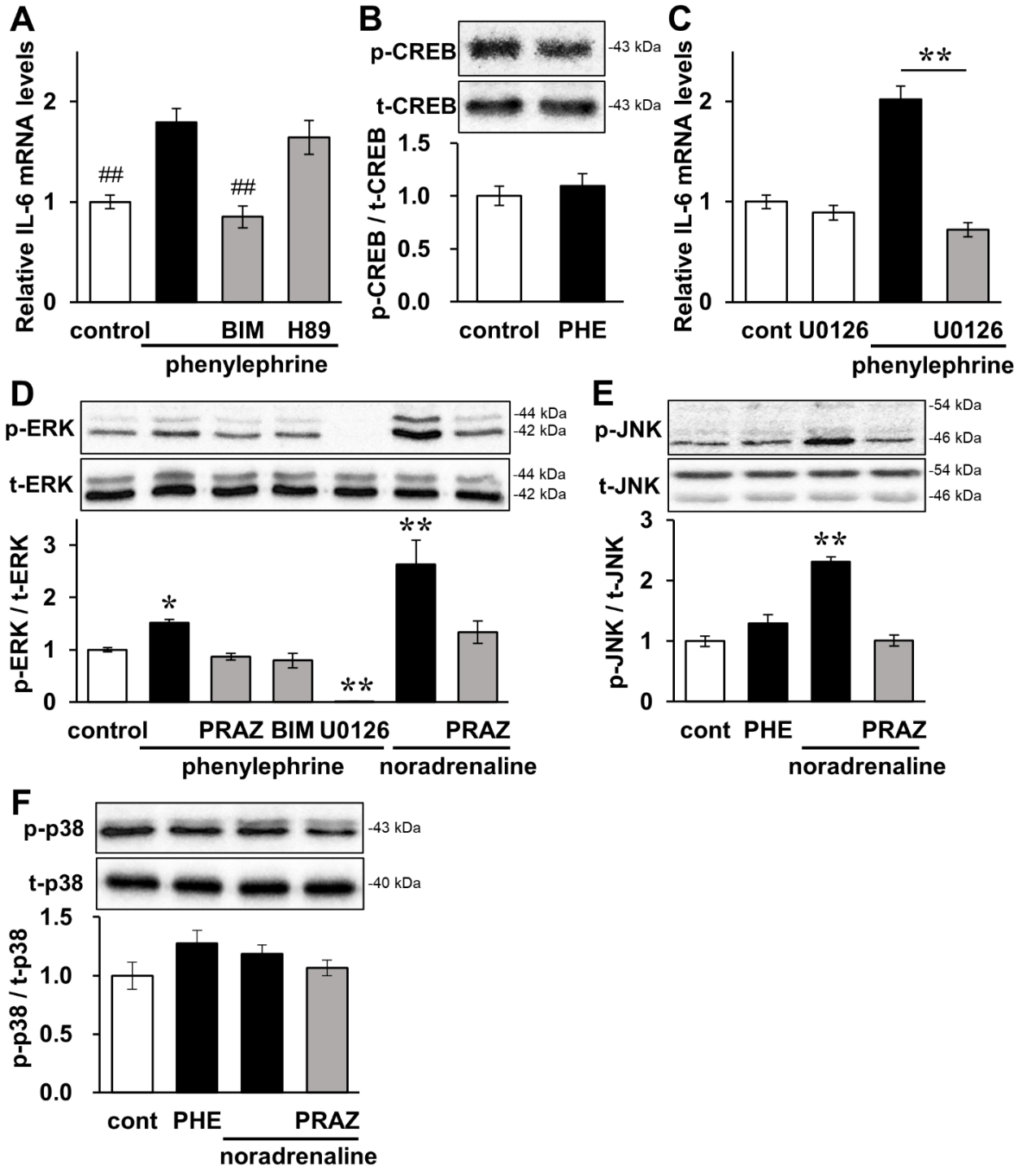
A
Relative IL-6 mRNA levels
0
1
2
##
##
control
BIM
H89
phenylephrine
B
p-CREB
t-CREB
-43 kDa
-43 kDa
p-CREB / t-CREB
0.0
0.5
1.0
1.5
control
PHE
C
Relative IL-6 mRNA levels
0
1
2
**
cont
U0126
U0126
phenylephrine
D
p-ERK
t-ERK
-44 kDa
-42 kDa
-44 kDa
-42 kDa
p-ERK / t-ERK
0
1
2
3
*
**
**
control
PRAZ
BIM
U0126
PRAZ
phenylephrine
noradrenaline
E
p-JNK
t-JNK
-54 kDa
-46 kDa
-54 kDa
-46 kDa
p-JNK / t-JNK
0
1
2
3
**
cont
PHE
PRAZ
noradrenaline
F
p-p38
t-p38
-43 kDa
-40 kDa
p-p38 / t-p38
0.0
0.5
1.0
1.5
cont
PHE
PRAZ
noradrenaline

Figure 21. Intracellular mechanisms of IL-6 transcriptional activation via α_1-adrenoceptors.

(A, C) IL-6 mRNA levels in astrocytes treated with the α_1-agonist phenylephrine (PHE, 1 μM) in the presence or absence of the PKC inhibitor BIM (5 μM), the PKA inhibitor H89 (5 μM), and the MEK/ERK inhibitor U0126 (10 μM) for 3 h. cont: control. n = 6. ##$p < 0.01$ vs. PHE alone (A, Dunnett's test), **$p < 0.01$ (C, unpaired Student's t-test). (B, D-F) The protein expression levels of phosphorylated and total CREB (B), ERK (D), JNK (E), and p38 (F) were quantified and representative blots are shown. GAPDH was used as a loading control. Astrocytes were treated with PHE, or noradrenaline (1 μM) in the presence or absence of the α_1-antagonist prazosin (PRAZ, 1 μM), BIM and U0126 for 30 min (B) or 10 min (D-F). n = 6. *$p < 0.05$, **$p < 0.01$ vs. control (Dunnett's test). All data are presented as means ± S.E.M.

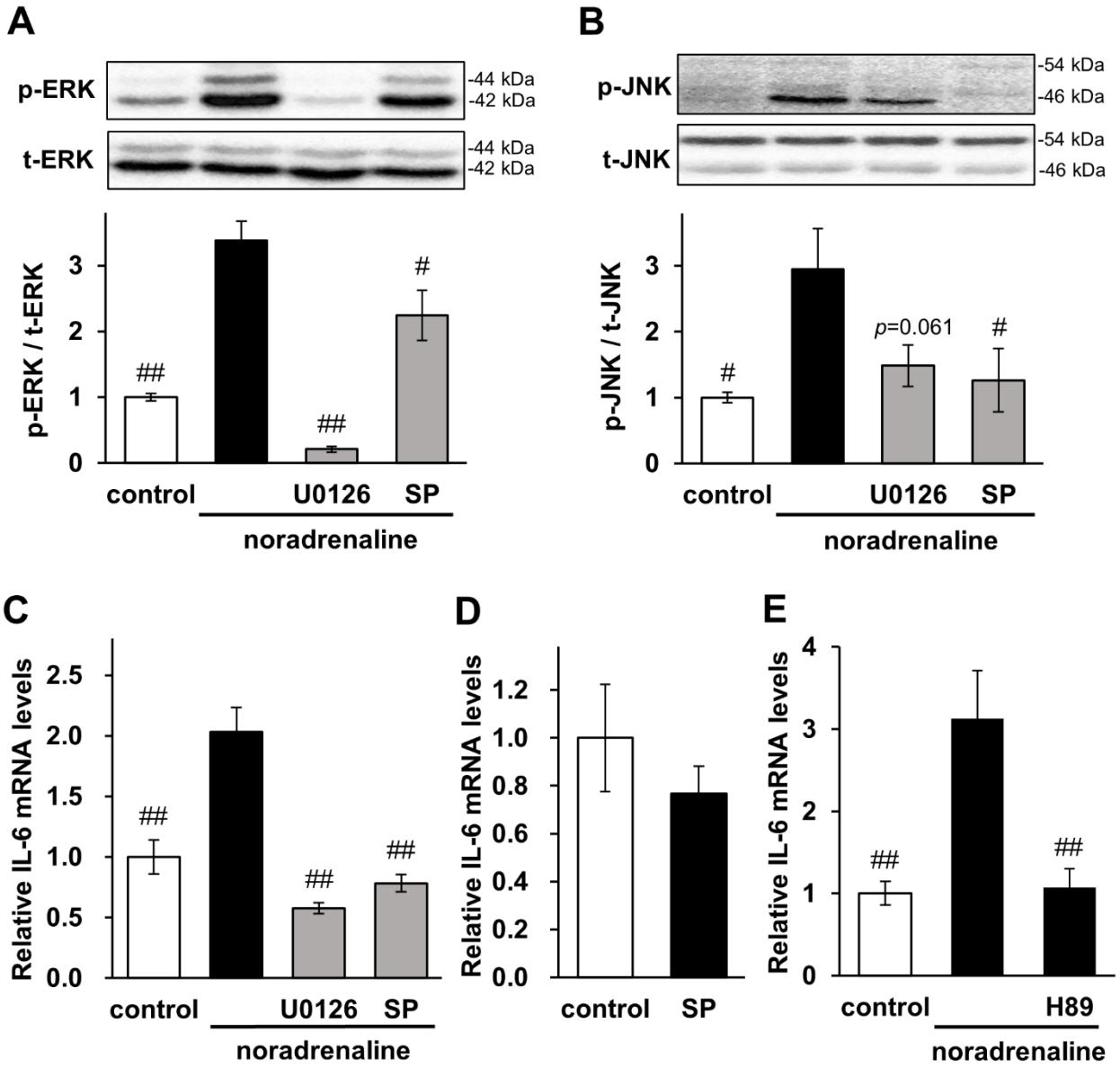

Figure 22. Effects of ERK, JNK, and PKA inhibitor on noradrenaline-induced transcriptional activation of IL-6.

(A, B) The protein expression levels of phosphorylated and total ERK (A) and JNK (B) were quantified, and representative blots are shown. Astrocytes were treated with noradrenaline (1 μM) in the presence or absence of the MEK/ERK inhibitor U0126 (10 μM) and the JNK inhibitor SP600125 (SP, 10 μM) for 10 min. n = 6. #$p < 0.05$, ##$p < 0.01$ vs. noradrenaline alone (Dunnett's test). (C, E) IL-6 mRNA levels in astrocytes treated with noradrenaline in the presence or absence of U0126, SP and the PKA inhibitor H89 (5 μM) for 3 h. n = 6. ##$p < 0.01$ vs. noradrenaline alone (Dunnett's test). (D) IL-6 mRNA levels in astrocytes treated with SP600125 for 4 h. n = 6. All data are presented as means ± S.E.M.

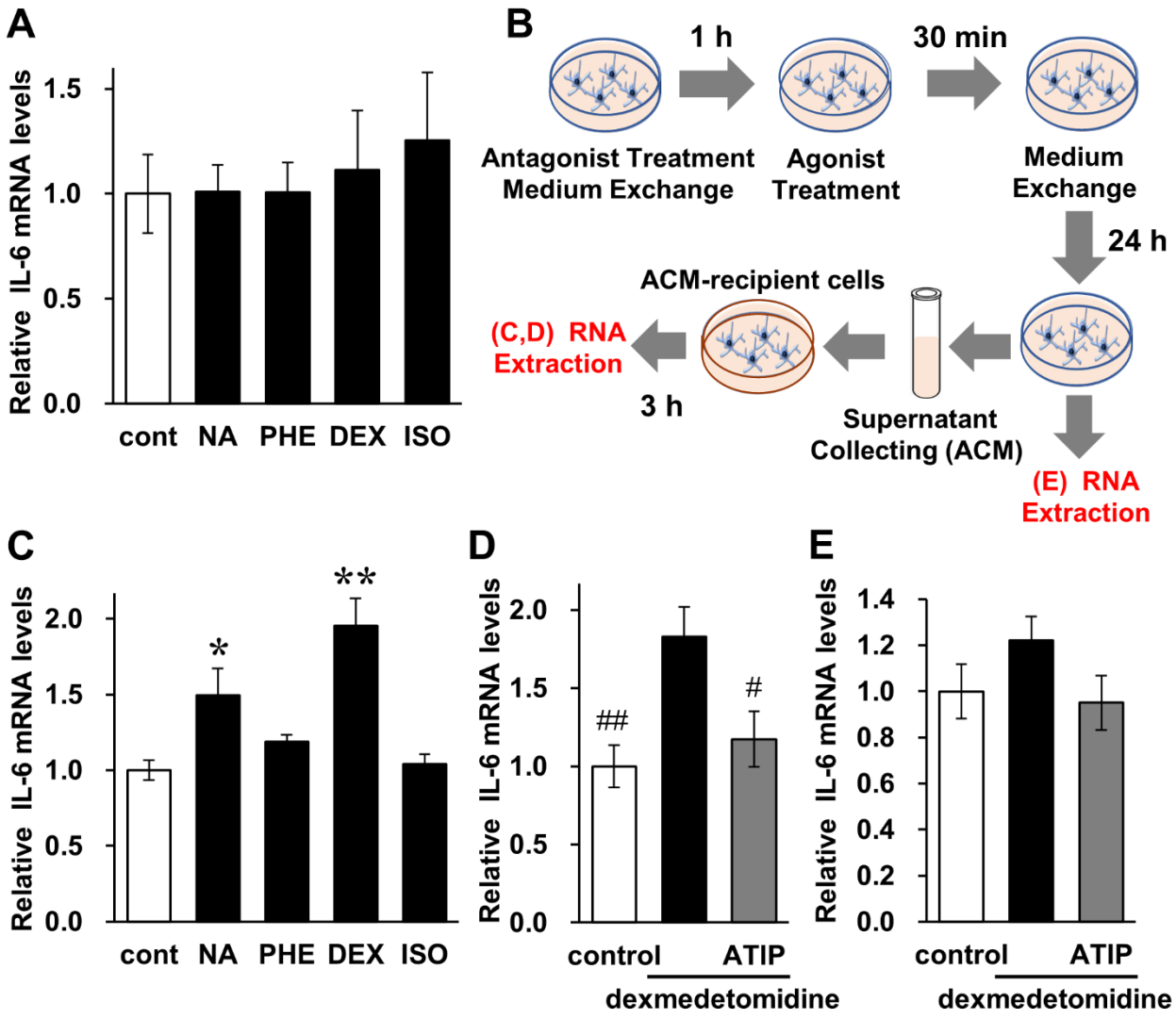

Figure 23. Effects of adrenoceptor-agonists on IL-6 mRNA levels via astrocyte conditioned medium.

(A) IL-6 mRNA levels in astrocytes treated with noradrenaline (NA, 1 μM), the α_1-agonist phenylephrine (PHE, 1 μM), the α_2-agonist dexmedetomidine (DEX, 1 μM), and the ß-agonist isoproterenol (ISO, 1 μM) for 24 h. cont: control. n = 6. (B) Schematic depiction of astrocyte conditioned medium (ACM) transfer experiment. (C, D) IL-6 mRNA levels in astrocytes incubated with ACM derived from astrocytes treated with NA, PHE, DEX and ISO in the presence or absence of α_2-antagonist atipamezole (ATIP, 1 μM) for 3 h. n = 6. *$p < 0.05$, **$p < 0.01$ vs. control (C, Dunnett's test), #$p < 0.05$, ##$p < 0.01$ vs. DEX alone (D, Dunnett's test). (E) IL-6 mRNA levels in astrocytes treated with DEX in the presence or absence of ATIP for 30 min and incubated for 24 h following medium exchange. n = 6. All data are presented as means ± S.E.M.

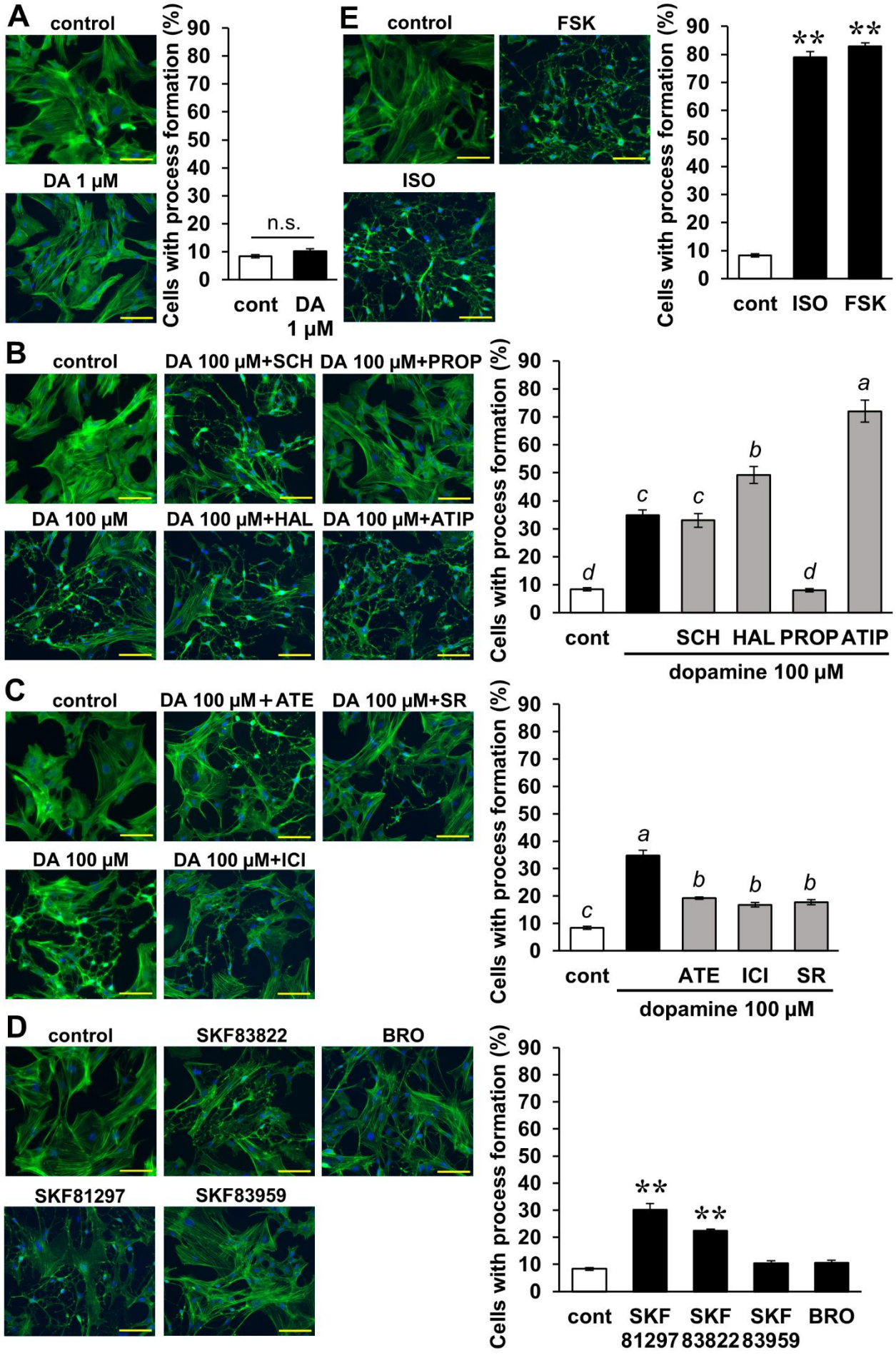
A
control
DA 1 μM
Cells with process formation (%)
n.s.
cont
DA 1 μM
E
control
FSK
ISO
**
**
cont
ISO
FSK
B
control
DA 100 μM+SCH
DA 100 μM+PROP
DA 100 μM
DA 100 μM+HAL
DA 100 μM+ATIP
a
b
c
c
d
d
cont
SCH
HAL
PROP
ATIP
dopamine 100 μM
C
control
DA 100 μM + ATE
DA 100 μM+SR
DA 100 μM
DA 100 μM+ICI
a
b
b
b
c
cont
ATE
ICI
SR
dopamine 100 μM
D
control
SKF83822
BRO
SKF81297
SKF83959
**
**
cont
SKF 81297
SKF 83822
SKF 83959
BRO

Figure 24. Effects of dopamine receptor and adrenoceptor agonists/antagonists on astrocytic process formation.

(A-E) Representative images of F-actin (green) and DAPI (blue) in astrocytes treated with dopamine (DA, A: 1 μM, B, C: 100 μM), D1-like receptor full agonist SKF81297 (10 μM), D1-like receptor adenylyl cyclase agonist SKF83822 (10 μM), D1-like receptor phospholipase C agonist SKF83959 (10 μM), D2-like receptor agonist bromocriptine (BRO, 10 μM), ß-agonist isoproterenol (ISO, 1 μM), and adenylate cyclase activator forskolin (FSK, 10 μM) in the presence or absence of the D1-like receptor antagonist SCH23390 (SCH, 10 μM), D2-like receptor antagonist haloperidol (HAL, 10 μM), ß-adrenoceptor antagonist (PROP, 10 μM), α_2-adrenoceptor antagonist atipamezole (ATIP, 10 μM), $ß_1$-adrenoceptor antagonist atenolol (ATE, 10 μM), $ß_2$-adrenoceptor antagonist ICI118551 (ICI, 1 μM), and $ß_3$-adrenoceptor antagonist SR59230A (SR, 1 μM) for 3 h. Scale bars = 100 μm. The graphs express the percentage of cells with process formation. More than 200 cells in three random fields were counted. cont: control. n = 6. n.s.: not significant (A, unpaired Student's t-test), means with the different letter are significantly different and with the same letter are not significantly different from each other (B, C, Tukey's t-test), $^{**}p < 0.01$ vs. control (D, E, Dunnett's test). All data are presented as means ± S.E.M.

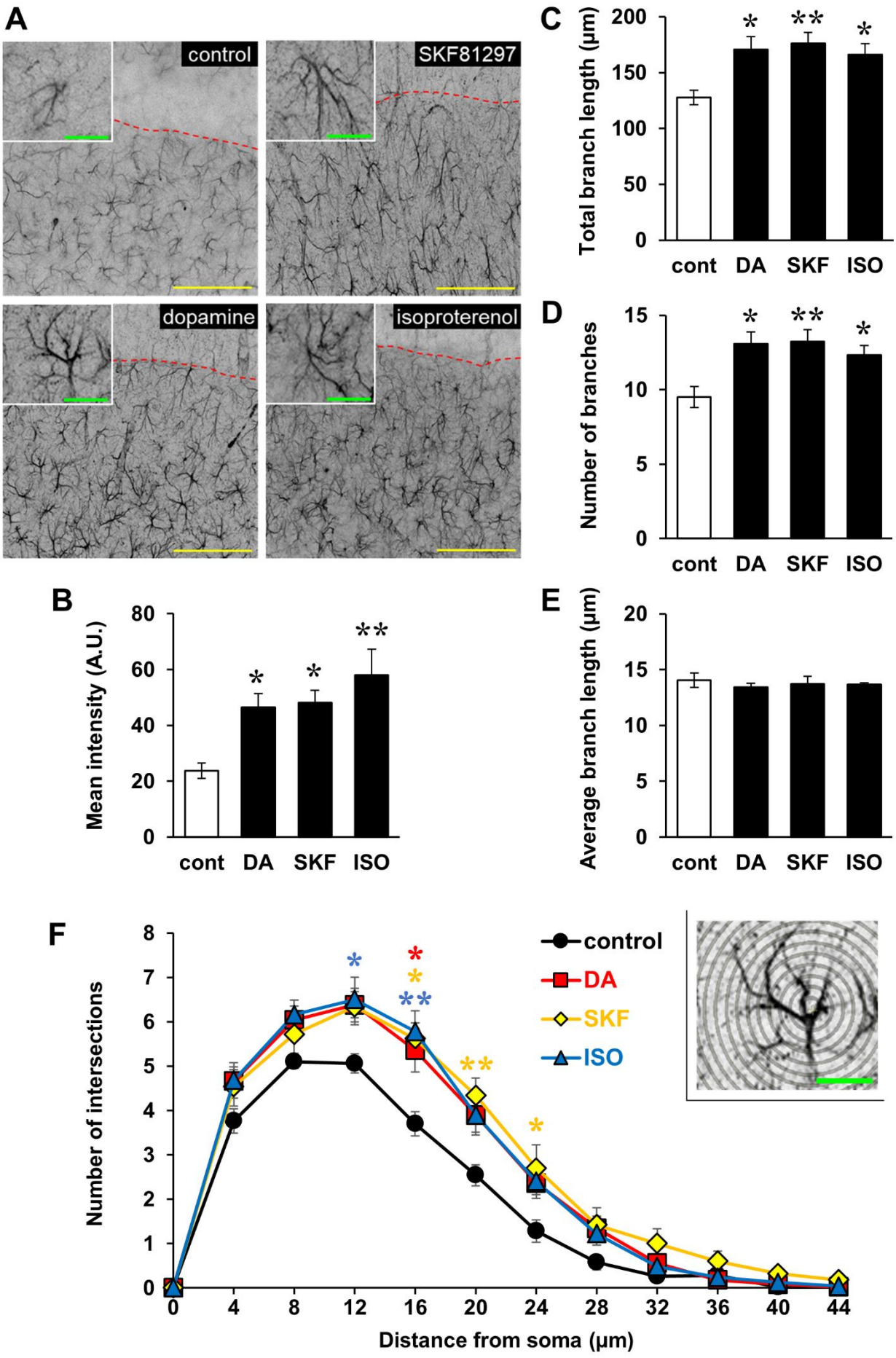
A
control
SKF81297
dopamine
isoproterenol
C
Total branch length (μm)
200
150
100
50
0
cont
DA
SKF
ISO
D
Number of branches
15
10
5
0
B
Mean intensity (A.U.)
80
60
40
20
E
Average branch length (μm)
20
15
10
5
F
Number of intersections
8
7
6
5
4
3
2
1
0
4
8
12
16
20
24
28
32
36
40
44
Distance from soma (μm)
control
DA
SKF
ISO

Figure 25. Effects of dopamine receptor and adrenoceptor agonists on GFAP expression in acute hippocampal slices.

(A) Representative GFAP-stained images of the CA1 areas in acute hippocampal slices treated with dopamine (DA, 10 μM), D1-like receptor full agonist SKF81297 (SKF, 10 μM), and ß-agonist isoproterenol (ISO, 10 μM) for 90 min (Upper left panel: high magnification of the representative astrocyte). Yellow scale bars = 100 μm, green scale bars = 20 μm. (B) The mean grey intensity of GFAP was qualified. The results are expressed as arbitrary units (A.U.). (C–F) The morphology of GFAP-stained astrocytes in the CA1 areas was analyzed using the Fiji-ImageJ Simple Neurite Tracer plugin. The morphological parameters assessed were the total branch length (C), number of branches (D), and average branch length (E); Sholl analysis was also performed (F), which measures the number of intersections at concentric spheres (at 4 μm intervals) originating from the soma (upper right panel). Scale bars = 20 μm. cont: control. n = 5. $*p < 0.05$, $**p < 0.01$ vs. control (Dunnett's test). All data are presented as means ± S.E.M.

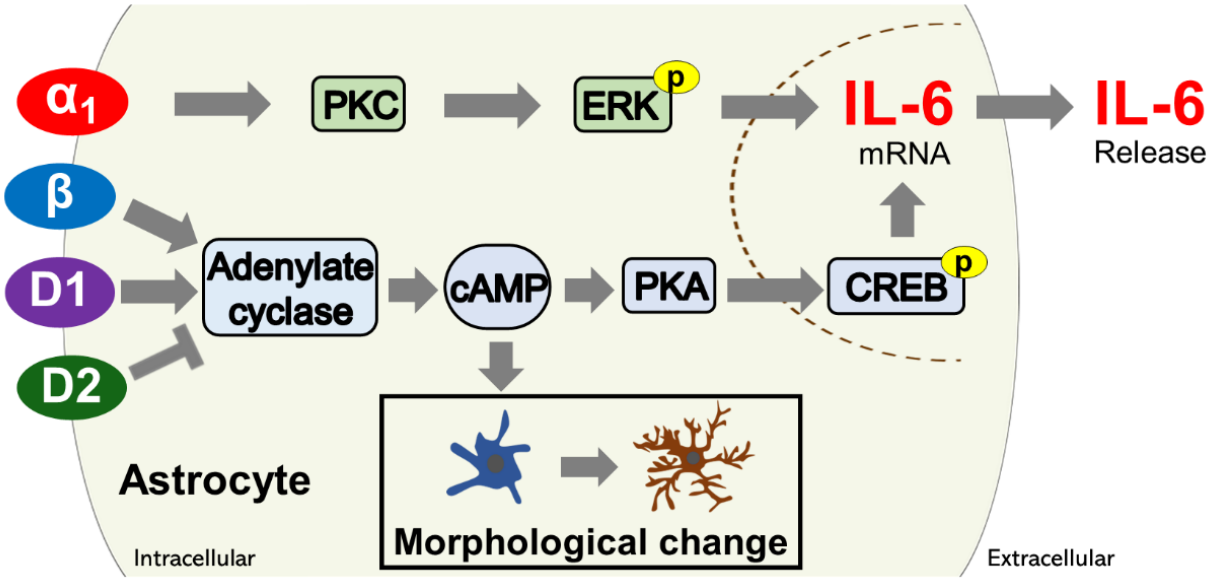

Figure 26. Graphical abstract in Chapter 2.

Conclusion

In the present study, I investigated the changes in glial cell cytokine expression and morphology under pathological conditions and the mechanisms of their regulation. In Chapter I, I showed that glial cells were transiently activated with increased cytokine expression and morphological changes, and microglial phagocytosis of dendritic spines was likely to lead to short-term memory impairment after the recovery of systemic symptoms in LPS-injected mouse models. In Chapter II, I also showed that monoamines, especially dopamine and noradrenaline, regulated IL-6 expression and process morphology in cultured astrocytes by multiple intracellular pathways. Taken together, monoamines may be involved in the pathogenesis of mental disorders by regulating inflammatory conditions such as cytokine production and morphology in glial cells under neuroinflammatory conditions. The present study shows novel pathology in which behavioral abnormalities occur even after recovery from glial cell activation, although many studies using LPS models have focused on acute symptoms. I also provide a novel concept that monoamines regulate neuroinflammation via multiple intracellular pathways in astrocytes. These findings will be useful for the development of mouse models with neuroinflammation and help to elucidate the pathophysiology of mental disorders caused by neuroinflammation.

There are several issues and subjects for future investigation in the present study. As the issue connecting Chapters I and II, it is necessary to investigate the degree to which monoamine regulates cytokine productions and morphological changes in glial cells and affects them at what stage of the pathological process in LPS model mice. Monoamines may be involved in early inflammatory response, since monoamines transiently increase about 1 hour after LPS administration in the brain (Sekio and Seki, 2015), and their effects on IL-6 expression and morphology in cultured astrocytes also transiently occurred 1-3 hours after treatment. In addition, LPS administration *in vivo* increases IL-6 expression several dozen-fold (Liu *et al.*, 2016), whereas dopamine and noradrenaline increased it several-fold in cultured astrocytes in the present study, which was mild compared to LPS *in vivo*. Taken together, inhibiting monoamine receptors in the early inflammatory process may partially reduce neuroinflammation, although the other effects of LPS are likely to contribute significantly to it.

It is important to note that proinflammatory cytokines have a dual function: beneficial and detrimental effects. In particular, some proinflammatory cytokines, such as IL-6, IL-1β, and TNF-α, enhance inflammatory responses at high doses and act as

neuroprotective/trophic factors at low doses, which maintain cognitive and learning functions via complex signaling pathways in the CNS (Bourgognon and Cavanagh, 2020). Therefore, it is likely to be important to control cytokine levels appropriately under neuroinflammation, rather than to suppress cytokine upregulation completely. However, it is a challenge to determine the threshold between physiologically and pathologically active levels and to identify and inhibit only the detrimental signaling pathways.

I focused mainly on astrocytes and microglia to evaluate the pathogenesis In the present study. Since astrocytes and microglia are the main cells in the CNS, both in terms of number and area of dominance, they are thought to be the main cells involved in the neuroinflammatory response. On the other hand, the involvement of the other cells needs to be taken into account. DAMPs released from neurons serve as the initiators of neuroinflammation and exacerbate the condition of brain sterile inflammation (Chang *et al.*, 2023). Furthermore, neuroinflammation is exacerbated by humoral factors and microRNAs released from brain endothelial cells (Ludewig *et al.*, 2019; Slota and Booth, 2019). The brain was considered "immune privilege" with little infiltration of peripheral immune cells, but recent reports indicate that peripheral blood leukocytes infiltrate the brain by transcytosis under physiological and pathological conditions (Louveau *et al.*, 2015; Pulgar, 2019). Cells other than glial cells may be involved in neuroinflammation through complex regulation, and further investigations are needed, including whether LPS-induced neuroinflammation initially originates from local brain responses or circulating factors.

It is important to focus on long-term changes in the properties of glial cells caused by transient stimulation of LPS or monoamines. In many mental disorders, their symptoms are chronic or prolonged. In addition, glial cell activation is maintained in mice treated with high doses of LPS or mice under chronic stress, even after the removal of these stimulating factors (Qin *et al.*, 2007; Rodríguez-Arias *et al.*, 2018). These suggest that the information of inflammation is memorized in glial cells, which may lead to long-term neuroinflammation. In general, several mechanisms by which information is stored in cells have been reported. For example, transcriptional regulation via intracellular phosphatases and epigenetic modulation is involved in the information storage of extracellular stimuli in neurons and innate lymphocytes, as is currently known. (Ma *et al.*, 2023; Santosa and Sun, 2023). In addition, microglial epigenetic regulation is altered in mice treated with LPS (Zhang *et al.*, 2022). On the other hand, the brain has plasticity, i.e., acquired memories are attenuated without continuous input of external stimuli. Therefore, I propose that the mechanism underlying the maintenance of long-term

inflammation in mental illness requires two factors: a mechanism of memory acquisition in glial cells and an external factor that maintains it.

I focused on the relationship between the monoamine and neuroinflammation hypothesis in the present study. Meanwhile, various pathways and factors have been proposed to be involved in the pathogenesis of mental disorders, such as the neurotrophic and cortisol hypothesis (Lang *et al.*, 2004; Qin *et al.*, 2016). A neurotrophin BDNF and cortisol increase with LPS-injected mice (Vakharia and Hinson, 2005; Guan and Fang, 2006), suggesting crosstalk among multiple hypotheses. Therefore, it is necessary to investigate the pathogenesis comprehensively and continuously, as well as focus on specific factors or phases for elucidating the etiology of mental disorders caused by inflammation.

Acknowledgment

I would like to acknowledge Dr. Ken-ichi Otsuguro (Professor, Laboratory of Pharmacology) for his preserving support and supervision during the course of my study. I would like to express my deepest gratitude to Dr. Takashi Kimura (Professor, Laboratory of Comparative Pathology), Dr. Osamu Ichii (Associate Professor, Laboratory of Anatomy), and Dr. Ryota Eguchi (Assistant Professor, Laboratory of Pharmacology), whose insightful guidance and valuable suggestions were instrumental in shaping this research. I am also indebted to the members of Laboratory of Pharmacology for their unwavering support and constructive feedback throughout this study. I am also grateful to my family and friends for their constant encouragement and understanding during this endeavor. Additionally, this work was supported by JSPS KAKENHI Grant Numbers JP21J20879, JP21K05950, and JP19K23701, and the World-leading Innovative and Smart Education (WISE) Program (1801) from the Ministry of Education, Culture, Sports, Science, and Technology, Japan. Finally, I sincerely express my deepest gratitude and sorrow to all animals supporting this study.

References

Afridi R., and Suk K. (2023). Microglial responses to stress-induced depression: Causes and consequences. *Cells*, **12**: 1521.

Ahn M.Y., Hwang J.S., Lee S.B., Ham S.A., Hur J., Kim J.T., and Seo H.G. (2017). Curcumin longa extract-loaded nanoemulsion improves the survival of endotoxemic mice by inhibiting nitric oxide-dependent HMGB1 release. *PeerJ*, **5**: 3808.

Allen N.J., and Eroglu C. (2017). Cell biology of astrocyte-synapse interactions. *Neuron*, **96**: 697–708.

Almeida P.G.C., Nani J.V., Oses J.P., Brietzke E., and Hayashi M.A.F. (2020). Neuroinflammation and glial cell activation in mental disorders. *Brain, Behavior, and Immunity - Health*, **2**: 100034.

Araki R., Nishida S., Hiraki Y., Li F., Matsumoto K., and Yabe T. (2016). Kamikihito Ameliorates lipopolysaccharide-induced sickness behavior via attenuating neural activation, but not inflammation, in the hypothalamic paraventricular nucleus and central nucleus of the amygdala in mice. *Biological and pharmaceutical bulletin*, **39**: 289–294.

Arias I., Sorlozano A., Villegas E., Luna J. de D., McKenney K., Cervilla J., Gutierrez B., and Gutierrez J. (2012). Infectious agents associated with schizophrenia: A meta-analysis. *Schizophrenia Research*, **136**: 128–136.

Arnsten A.F.T. (2000). Through the looking glass: Differential noradenergic modulation of prefrontal cortical function. *Neural Plasticity*, **7**: 133–146.

Aronica E., Gorter J.A., Rozemuller A.J., Yankaya B., and Troost D. (2005). Activation of metabotropic glutamate receptor 3 enhances interleukin (IL)-1ß-stimulated release of IL-6 in cultured human astrocytes. *Neuroscience*, **130**: 927–933.

Augusto-Oliveira M., Arrifano G.P., Lopes-Araújo A., Santos-Sacramento L., Takeda P.Y., Anthony D.C., Malva J.O., and Crespo-Lopez M.E. (2019). What do microglia really do in healthy adult brain? *Cells*, **8**: 1293.

Baker A.J., Zornow M.H., Scheller M.S., Yaksh T.L., Skilling S.R., Smullin D.H., Larson

A.A., and Kuczenski R. (1991). Changes in extracellular concentrations of glutamate, aspartate, glycine, dopamine, serotonin, and dopamine metabolites after transient global ischemia in the rabbit brain. *Journal of Neurochemistry*, **57**: 1370–1379.

Bambico F.R., Bregman T., Diwan M., Li J., Darvish-Ghane S., Li Z., Laver B., Amorim B.O., Covolan L., Nobrega J.N., and Hamani C. (2015). Neuroplasticity-dependent and -independent mechanisms of chronic deep brain stimulation in stressed rats. *Translational Psychiatry*, **5**: 674.

Banks W.A., and Robinson S.M. (2010). Minimal penetration of lipopolysaccharide across the murine blood-brain barrier. *Brain, Behavior, and Immunity*, **24**: 102–109.

Barker G.R.I., and Warburton E.C. (2011). When is the hippocampus involved in recognition memory? *Journal of Neuroscience*, **31**: 10721–10731.

Bartsch T., and Wulff P. (2015). The hippocampus in aging and disease: From plasticity to vulnerability. *Neuroscience*, **309**: 1–16.

Basu S., and Lamprecht R. (2018). The role of actin cytoskeleton in dendritic spines in the maintenance of long-term memory. *Frontiers in Molecular Neuroscience*, **11**: 143.

Bayram-Weston Z., Olsen E., Harrison D.J., Dunnett S.B., and Brooks S.P. (2016). Optimising Golgi-Cox staining for use with perfusion-fixed brain tissue validated in the zQ175 mouse model of Huntington's disease. *Journal of Neuroscience Methods*, **265**: 81–88.

Bellavite P. (2023). Neuroprotective potentials of flavonoids: Experimental studies and mechanisms of action. *Antioxidants*, **12**: 280.

Bello-Arroyo E., Roque H., Marcos A., Orihuel J., Higuera-Matas A., Desco M., Caiolfa V.R., Ambrosio E., Lara-Pezzi E., and Gómez-Gaviro M.V. (2018). MouBeAT: A new and open toolbox for guided analysis of behavioral tests in mice. *Frontiers in Behavioral Neuroscience*, **12**: 201.

Bennett M.L., and Viaene A.N. (2021). What are activated and reactive glia and what is their role in neurodegeneration? *Neurobiology of Disease*, **148**: 105172.

Berghe W.V., Vermeulen L., Wilde G.D., Bosscher K.D., Boone E., and Haegeman G.

(2000). Signal transduction by tumor necrosis factor and gene regulation of the inflammatory cytokine interleukin-6. *Biochemical Pharmacology*. **60**: 1185-1195.

Boku S., Nakagawa S., Toda H., and Hishimoto A. (2018). Neural basis of major depressive disorder: Beyond monoamine hypothesis. *Psychiatry and Clinical Neurosciences*, **72**: 3–12.

Bourgognon J.M., and Cavanagh J. (2020). The role of cytokines in modulating learning and memory and brain plasticity. *Brain and Neuroscience Advances*, **4**: 2398212820979802.

Bowyer J.F., Sarkar S., Burks S.M., Hess J.N., Tolani S., O'Callaghan J.P., and Hanig J.P. (2020). Microglial activation and responses to vasculature that result from an acute LPS exposure. *NeuroToxicology*, **77**: 181–192.

Broadbent N.J., Gaskin S., Squire L.R., and Clark R.E. (2010). Object recognition memory and the rodent hippocampus. *Learning and Memory*, **17**: 5–11.

Cao P., Chen C., Liu A., Shan Q., Zhu X., Jia C., Peng X., Zhang M., Farzinpour Z., Zhou W., Wang H., Zhou J.N., Song X., Wang L., Tao W., Zheng C., Zhang Y., Ding Y.Q., Jin Y., Xu L., and Zhang Z. (2021). Early-life inflammation promotes depressive symptoms in adolescence via microglial engulfment of dendritic spines. *Neuron*, **109**: 2573–2589.

Casey L.C., Balk R.A., and Bone R.C. (1993). Plasma cytokine and endotoxin levels correlate with survival in patients with the sepsis syndrome. *Annals of Internal Medicine*, **119**: 771–778.

Chang C.J., Ishii H., Yamamoto H., Yamamoto T., and Spatz M. (1993). Effects of cerebral ischemia on regional dopamine release and D_1 and D_2 receptors. *Journal of Neurochemistry*, **60**: 1483–1490.

Chang N.P., DaPrano E.M., Evans W.R., Nissenbaum M., McCourt M., Alzate D., Lindman M., Chou T.W., Atkins C., Kusnecov A.W., Huda R., and Daniels B.P. (2023). Neuronal DAMPs exacerbate neurodegeneration via astrocytic RIPK3 signaling. *BioRxiv*, Preprint.

Chesworth R., Watt G., and Karl T. (2018). Cannabinoid modulation of object recognition and location memory—A preclinical assessment. *Handbook of Behavioral Neuroscience*,

27: 461–488.

Choi S., Kim K., Chang J., Kim S.M., Kim S.J., Cho H.J., and Park S.M. (2019). Association of chronic periodontitis on Alzheimer's disease or vascular dementia. *Journal of the American Geriatrics Society*, **67**: 1234–1239.

Cinalli D.A., Cohen S.J., Guthrie K., and Stackman R.W. (2020). Object recognition memory: Distinct yet complementary roles of the mouse CA1 and perirhinal cortex. *Frontiers in Molecular Neuroscience*, **13**: 527543.

Clark W.M., Rinker L.G., Lessov N.S., Hazel K., and Eckenstein F. (1999). Time course of IL-6 expression in experimental CNS ischemia. *Neurological Research*, **21**: 287–292.

Cohen S.J., and Stackman R.W. (2015). Assessing rodent hippocampal involvement in the novel object recognition task. A review. *Behavioural Brain Research*, **285**: 105–117.

Cope E.C., LaMarca E.A., Monari P.K., Olson L.B., Martinez S., Zych A.D., Katchur N.J., and Gould E. (2018). Microglia play an active role in obesity-associated cognitive decline. *Journal of Neuroscience*, **38**: 8889–8904.

Corkrum M., Covelo A., Lines J., Bellocchio L., Pisansky M., Loke K., Quintana R., Rothwell P.E., Lujan R., Marsicano G., Martin E.D., Thomas M.J., Kofuji P., and Araque A. (2020). Dopamine-evoked synaptic regulation in the nucleus accumbens requires astrocyte activity. *Neuron*, **105**: 1036-1047.

Cragg S.J., and Rice M.E. (2004). DAncing past the DAT at a DA synapse. *Trends in Neurosciences*, **27**: 270–277.

Davydow D.S., Hough C.L., Langa K.M., and Iwashyna T.J. (2013). Symptoms of depression in survivors of severe sepsis: A prospective cohort study of older Americans. *The American Journal of Geriatric Psychiatry*, **21**: 887–897.

Day J.S., O'Neill E., Cawley C., Aretz N.K., Kilroy D., Gibney S.M., Harkin A., and Connor T.J. (2014). Noradrenaline acting on astrocytic ß$_2$-adrenoceptors induces neurite outgrowth in primary cortical neurons. *Neuropharmacology*, **77**: 234–248.

Denninger J.K., Smith B.M., and Kirby E.D. (2018). Novel object recognition and object location behavioral testing in mice on a budget. *Journal of Visualized Experiments*, **141**:

58593.

Du L., Chang H., Xu W., Wei Y., Wang Y., Yin L., and Zhang X. (2020). Effect of NMO-IgG on the interleukin-6 cascade in astrocytes via activation of the JAK/STAT3 signaling pathway. *Life Sciences*, **258**: 118217.

Duan L., Zhang X. Di, Miao W.Y., Sun Y.J., Xiong G., Wu Q., Li G., Yang P., Yu H., Li H., Wang Y., Zhang M., Hu L.Y., Tong X., Zhou W.H., and Yu X. (2018). PDGFRβ cells rapidly relay inflammatory signal from the circulatory system to neurons via chemokine CCL2. *Neuron*, **100**: 183–200.

Dunn G.A., Loftis J.M., and Sullivan E.L. (2020). Neuroinflammation in psychiatric disorders: An introductory primer. *Pharmacology Biochemistry and Behavior*, **196**: 172981.

Escartin C., Galea E., Lakatos A., O'Callaghan J.P., Petzold G.C., Serrano-Pozo A., Steinhäuser C., Volterra A., Carmignoto G., Agarwal A., Allen N.J., Araque A., Barbeito L., Barzilai A., Bergles D.E., Bonvento G., Butt A.M., Chen W.T., Cohen-Salmon M., Cunningham C., Deneen B., De Strooper B., Díaz-Castro B., Farina C., Freeman M., Gallo V., Goldman J.E., Goldman S.A., Götz M., Gutiérrez A., Haydon P.G., Heiland D.H., Hol E.M., Holt M.G., Iino M., Kastanenka K.V., Kettenmann H., Khakh B.S., Koizumi S., Lee C.J., Liddelow S.A., MacVicar B.A., Magistretti P., Messing A., Mishra A., Molofsky A.V., Murai K.K., Norris C.M., Okada S., Oliet S.H.R., Oliveira J.F., Panatier A., Parpura V., Pekna M., Pekny M., Pellerin L., Perea G., Pérez-Nievas B.G., Pfrieger F.W., Poskanzer K.E., Quintana F.J., Ransohoff R.M., Riquelme-Perez M., Robel S., Rose C.R., Rothstein J.D., Rouach N., Rowitch D.H., Semyanov A., Sirko S., Sontheimer H., Swanson R.A., Vitorica J., Wanner I.B., Wood L.B., Wu J., Zheng B., Zimmer E.R., Zorec R., Sofroniew M.V., and Verkhratsky A. (2021). Reactive astrocyte nomenclature, definitions, and future directions. *Nature Neuroscience*, **24**: 312–325.

Franco R., Ferre S., Agnati L., Torvinen M., Gines S., Hillion J., Casado V., Lledo P.M., Zoli M., Lluis C., and Fuxe K. (2000). Evidence for adenosine/dopamine receptor interactions: Indications for heteromerization. *Neuropsychopharmacology*, **23**: 50–59.

Fricker M., Oliva-Martín M.J., and Brown G.C. (2012). Primary phagocytosis of viable neurons by microglia activated with LPS or Aβ is dependent on calreticulin/LRP phagocytic signalling. *Journal of Neuroinflammation*, **9**: 196.

Fuxe K., Agnati L.F., Marcoli M., and Borroto-Escuela D.O. (2015). Volume transmission in central dopamine and noradrenaline neurons and its astroglial targets. *Neurochemical Research*, **40**: 2600–2614.

Gao V., Suzuki A., Magistretti P.J., Lengacher S., Pollonini G., Steinman M.Q., and Alberini C.M. (2016). Astrocytic ß$_2$-adrenergic receptors mediate hippocampal long-term memory consolidation. *Proceedings of the National Academy of Sciences of the United States of America*, **113**: 8526–8531.

Gavrilyuk V., Russo C. Dello, Heneka M.T., Pelligrino D., Weinberg G., and Feinstein D.L. (2002). Norepinephrine increases IκBα expression in astrocytes. *Journal of Biological Chemistry*, **277**: 29662–29668.

Globus M.Y.T., Busto R., Dietrich W.D., Martinez E., Valdes I., and Ginsberg M.D. (1989). Direct evidence for acute and massive norepinephrine release in the Hippocampus during transient ischemia. *Journal of Cerebral Blood Flow and Metabolism,* **9**: 892–896.

Guan Z., and Fang J. (2006). Peripheral immune activation by lipopolysaccharide decreases neurotrophins in the cortex and hippocampus in rats. *Brain, Behavior, and Immunity*, **20**: 64–71.

Guo S., Wang H., and Yin Y. (2022). Microglia polarization from M1 to M2 in neurodegenerative Diseases. *Frontiers in Aging Neuroscience*, **14**: 815347.

Hart C.G., and Karimi-Abdolrezaee S. (2021). Recent insights on astrocyte mechanisms in CNS homeostasis, pathology, and repair. *Journal of Neuroscience Research*, **99**: 2427–2462.

Haskó G., Elenkov I.J., Kvetan V., and Vizi E.S. (1995). Differential effect of selective block of α$_2$-adrenoreceptors on plasma levels of tumour necrosis factor-α, interleukin-6 and corticosterone induced by bacterial lipopolysaccharide in mice. *Journal of Endocrinology*, **144**: 457–462.

He Q., Yu W., Wu J., Chen C., Lou Z., Zhang Q., Zhao J., Wang J., and Xiao B. (2013). Intranasal LPS-mediated Parkinson's model challenges the pathogenesis of nasal cavity and environmental toxins. *PLoS ONE*, **8**: 78418.

Hebert T.E., Moffett S., Morello J.P., Loisel T.P., Bichet D.G., Barret C., and Bouvier M.

(1996). A peptide derived from a ß2-adrenergic receptor transmembrane domain onhibits both receptor dimerization and activation. *Journal of Biological Chemistry*, **271**: 16384–16392.

Hernandez-Ruiz V., Letenneur L., Fülöp T., Helmer C., Roubaud-Baudron C., Avila-Funes J.A., and Amieva H. (2022). Infectious diseases and cognition: Do we have to worry? *Neurological Sciences*, **43**: 6215–6224.

Hindmarch I. (2002). Beyond the monoamine hypothesis: Mechanisms, molecules and methods. *European Psychiatry*, **17**: 294–299.

Hirschfeld R.M.A. (2000). History and evolution of the monoamine hypothesis of depression. *The Journal of Clinical Psychiatry*, **61**: 4–6.

Hoogendijk W.J.G., Feenstra M.G.P., Botterblom M.H.A., Gilhuis J., Sommer I.E.C., Kamphorst W., Eikelenboom P., and Swaab D.F. (1999). Increased activity of surviving locus ceruleus neurons in Alzheimer's disease. *Annals of Neurology*, **45**: 82–91.

Hoogland I.C.M., Houbolt C., van Westerloo D.J.,van Gool W.A., and Beek D.V.D. (2015). Systemic inflammation and microglial activation: Systematic review of animal experiments. *Journal of Neuroinflammation*, **12**: 114.

Hoshino K., Takeuchi O., Kawai T., Sanjo H., Ogawa T., Takeda Y., Takeda K., and Akira S. (1999). Cutting edge: Toll-like receptor 4 (TLR4)-deficient mice are hyporesponsive to lipopolysaccharide: Evidence for TLR4 as the *Lps* gene product. *The Journal of Immunology*, **162**: 3749–3752.

Huang R., and Hertz L. (2000). Receptor subtype and dose dependence of dexmedetomidine-induced accumulation of [14C]glutamine in astrocytes suggests glial involvement in its hypnotic-sedative and anesthetic-sparing effects. *Brain Research*, **873**: 297–301.

Hung C.C., Lin C.H., Chang H., Wang C.Y., Lin S.H., Hsu P.C., Sun Y.Y., Lin T.N., Shie F.S., Kao L. Sen, Chou C.M., and Lee Y.H. (2016). Astrocytic GAP43 induced by the TLR4/NF-κB/STAT3 axis attenuates astrogliosis-mediated microglial activation and neurotoxicity. *Journal of Neuroscience*, **36**: 2027–2043.

Hunger L., Kumar A., and Schmidt R. (2020). Abundance compensates kinetics: Similar

effect of dopamine signals on D1 and D2 receptor populations. *The Journal of Neuroscience*, **40**: 2868–2681.

Ikeshima-Kataoka H. (2016). Neuroimmunological implications of AQP4 in astrocytes. *International Journal of Molecular Sciences*, **17**: 1306.

Jellinger K.A. (2023). Depression in dementia with Lewy bodies: A critical update. *Journal of Neural Transmission*, **130**: 1207–1218.

Jiang J., Tang B., Wang L., Huo Q., Tan S., Misrani A., Han Y., Li H., Hu H., Wang J., Cheng T., Tabassum S., Chen M., Xie W., Long C., and Yang L. (2022). Systemic LPS-induced microglial activation results in increased GABAergic tone: A mechanism of protection against neuroinflammation in the medial prefrontal cortex in mice. *Brain, Behavior, and Immunity*, **99**: 53–69.

John G.R., Lee S.C., and Brosnan C.F. (2003). Cytokines: Powerful regulators of glial cell Activation. *The Neuroscientist*, **9**: 10–22.

Jordan B.A., and Devi L.A. (1999). G-protein-coupled receptor heterodimerization modulates receptor function. *Nature*, **399**: 697–700.

Jordan B.A., Gomes I., Rios C., Filipovska J., and Devi L.A. (2003). Functional Interactions between opioid and 2A-adrenergic receptors. *Molecular pharmacology*, 64, 1317–1324.

Josselyn S.A., and Tonegawa S. (2020). Memory engrams: Recalling the past and imagining the future. *Science*, **367**: 4325.

Jurga A.M., Paleczna M., and Kuter K.Z. (2020). Overview of general and discriminating markers of differential microglia phenotypes. *Frontiers in Cellular Neuroscience*, **14**: 198.

Karin M., Liu Z.G., and Zandi E. (1997). AP-1 function and regulation. *Current Opinion in Cell Biology*, **9**: 240–246.

Kikuchi D.S., Campos A.C.P., Qu H., Forrester S.J., Pagano R.L., Lassègue B., Sadikot R.T., Griendling K.K., and Hernandes M.S. (2019). Poldip2 mediates blood-brain barrier disruption in a model of sepsis-associated encephalopathy. *Journal of Neuroinflammation*, **16**: 241.

Kitano T., Eguchi R., Okamatsu-Ogura Y., Yamaguchi S., and Otsuguro K. (2021). Opposing functions of α- and ß-adrenoceptors in the formation of processes by cultured astrocytes. *Journal of Pharmacological Sciences*, **145**: 228–240.

Klein M.O., Battagello D.S., Cardoso A.R., Hauser D.N., Bittencourt J.C., and Correa R.G. (2019). Dopamine: Functions, signaling, and association with neurological diseases. *Cellular and Molecular Neurobiology*, **39**: 31–59.

Koppel I., Jaanson K., Klasche A., Tuvikene J., Tiirik T., Pärn A., and Timmusk T. (2018). Dopamine cross-reacts with adrenoreceptors in cortical astrocytes to induce BDNF expression, CREB signaling and morphological transformation. *Glia*, **66**: 206–216.

Kraeuter A.K., Guest P.C., and Sarnyai Z. (2019). The Y-maze for assessment of spatial working and reference memory in mice. *Methods in Molecular Biology*, **1916**: 105–111.

Kuric E., Wieloch T., and Ruscher K. (2013). Dopamine receptor activation increases glial cell line-derived neurotrophic factor in experimental stroke. *Experimental Neurology*, **247**: 202–208.

Lang U.E., Jockers-Scherübl M.C., and Hellweg R. (2004). State of the art of the neurotrophin hypothesis in psychiatric disorders: Implications and limitations. *Journal of Neural Transmission*, **111**: 387–411.

Lawrence J.M., Schardien K., Wigdahl B., and Nonnemacher M.R. (2023). Roles of neuropathology-associated reactive astrocytes: A systematic review. *Acta Neuropathologica Communications*, **11**: 42.

Lee S., Jeong J., Kwak Y., and Park S.K. (2010). Depression research: Where are we now? *Molecular Brain*, **3**: 8.

Lee S.P., So C.H., Rashid A.J., Varghese G., Cheng R., Lança A.J., O'Dowd B.F., and George S.R. (2004). Dopamine D1 and D2 receptor co-activation generates a novel phospholipase C-mediated calcium signal. *Journal of Biological Chemistry*, **279**: 35671–35678.

Leger M., Quiedeville A., Bouet V., Haelewyn B., Boulouard M., Schumann-Bard P., and Freret T. (2013). Object recognition test in mice. *Nature Protocols*, **8**: 2531–2537.

Li Y., Ji M., and Yang J. (2022). Current understanding of long-term cognitive impairment after sepsis. *Frontiers in Immunology*, **13**: 855006.

Liu M.Y., Yin C.Y., Zhu L.J., Zhu X.H., Xu C., Luo C.X., Chen H., Zhu D.Y., and Zhou Q.G. (2018). Sucrose preference test for measurement of stress-induced anhedonia in mice. *Nature Protocols*, **13**: 1686–1698.

Liu X., Nemeth D.P., Tarr A.J., Belevych N., Syed Z.W., Wang Y., Ismail A.S., Reed N.S., Sheridan J.F., Yajnik A.R., Disabato D.J., Zhu L., and Quan N. (2016). Euflammation attenuates peripheral inflammation-induced neuroinflammation and mitigates immune-to-brain signaling. *Brain, Behavior, and Immunity*, **54**: 140–148.

Lively S., and Schlichter L.C. (2018). Microglia responses to pro-inflammatory stimuli (LPS, IFNγ+TNFα) and reprogramming by resolving cytokines (IL-4, IL-10). *Frontiers in Cellular Neuroscience*, **12**: 215.

Louveau A., Harris T.H., and Kipnis J. (2015). Revisiting the mechanisms of CNS immune privilege. *Trends in Immunology*, **36**: 569–577.

Ludewig P., Winneberger J., and Magnus T. (2019). The cerebral endothelial cell as a key regulator of inflammatory processes in sterile inflammation. *Journal of Neuroimmunology*, **326**: 38–44.

Ma H., Khaled H.G., Wang X., Mandelberg N.J., Cohen S.M., He X., and Tsien R.W. (2023). Excitation–transcription coupling, neuronal gene expression and synaptic plasticity. *Nature Reviews Neuroscience*, **24**: 672–692.

Maes M., Planken M. Van Der, Stevens W.J., Peeters D., DeClerck L.S., Bridts C.H., Schotte C., and Cosyns P. (1992). Leukocytosis, monocytosis and neutrophilia: Hallmarks of severe depression. *Journal of Psychiatric Research*, **26**: 125–134.

Manaenko A., Chen H., Kammer J., Zhang J.H., and Tang J. (2011). Comparison Evans blue injection routes: Intravenous versus intraperitoneal, for measurement of blood–brain barrier in a mice hemorrhage model. *Journal of Neuroscience Methods*, **195**: 206–210.

Mantyh P.W., Rogers S.D., Allen C.J., Catton M.D., Ghilardi J.R., Levin L.A., Maggio J.E., and Vigna S.R. (1995). Beta 2-adrenergic receptors are expressed by glia in vivo in

the normal and injured central nervous system in the rat, rabbit, and human. *The Journal of Neuroscience*, **15**: 152–164.

Miedel C.J., Patton J.M., Miedel A.N., Miedel E.S., and Levenson J.M. (2017). Assessment of spontaneous alternation, novel object recognition and limb clasping in transgenic mouse models of amyloid-ß and tau neuropathology. *Journal of Visualized Experiments*, **123**: 55523.

Mihevc S.P., and Majdič G. (2019). Canine cognitive dysfunction and Alzheimer's disease – Two facets of the same disease? *Frontiers in Neuroscience*, **13**: 461729.

Montoya A., Elgueta D., Campos J., Chovar O., Falcón P., Matus S., Alfaro I., Bono M.R., and Pacheco R. (2019). Dopamine receptor D_3 signalling in astrocytes promotes neuroinflammation. *Journal of Neuroinflammation*, **16**: 258.

Moraes M.M.T., Galvão M.C., Cabral D., Coelho C.P., Queiroz-Hazarbassanov N., Martins M.F.M., Bondan E.F., Bernardi M.M., and Kirsten T.B. (2017). Propentofylline prevents sickness behavior and depressive-like behavior induced by lipopolysaccharide in rats via neuroinflammatory pathway. *PLoS ONE*, **12**: 0169446.

Mori K., Kaneko Y.S., Nakashima A., Fujiwara K., Nagatsu I., and Ota A. (2003). Effect of peripheral lipopolysaccharide injection on dopamine content in murine anterior olfactory nucleus. *Journal of Neural Transmission*, **110**: 31–50.

Murdaca G., Paladin F., Casciaro M., Vicario C.M., Gangemi S., and Martino G. (2022). Neuro-inflammaging and psychopathological distress. *Biomedicines*, **10**: 2133.

Na S.Y., and Krishnamoorthy G. (2021). Spontaneous mouse models of neuroinflammation. *Translational Methods for Multiple Sclerosis Research*, **166**: 89–107.

Nakamura A., Johns E.J., Imaizumi A., Abe T., and Kohsaka T. (1998). Regulation of tumour necrosis factor and interleukin-6 gene transcription by $ß_2$-adrenoceptor in the rat astrocytes. *Journal of Neuroimmunology*, **88**: 144–153.

Nakamura S. (2022). Integrated pathophysiology of schizophrenia, major depression, and bipolar disorder as monoamine axon disorder. *Frontiers in Bioscience*, **14**: 4.

Naor Z., Benard O., and Seger R. (2000). Activation of MAPK cascades by G-protein-

coupled receptors: The case of gonadotropin-releasing hormone receptor. *Trends in Endocrinology and Metabolism*, **11**: 91–99.

Nazem A., Sankowski R., Bacher M., and Al-Abed Y. (2015). Rodent models of neuroinflammation for Alzheimer's disease. *Journal of Neuroinflammation*, **12**: 74.

O'Connor T.G., Moynihan J.A., and Caserta M.T. (2014). Annual research review: The neuroinflammation hypothesis for stress and psychopathology in children – developmental psychoneuroimmunology. *Journal of Child Psychology and Psychiatry*, **55**: 615–631.

Pascual O., Achour S. Ben, Rostaing P., Triller A., and Bessis A. (2012). Microglia activation triggers astrocyte-mediated modulation of excitatory neurotransmission. *Proceedings of the National Academy of Sciences of the United States of America*, **109**: 197–205.

Pascucci T., Ventura R., Latagliata E.C., Cabib S., and Puglisi-Allegra S. (2007). The medial prefrontal cortex determines the accumbens dopamine response to stress through the opposing influences of norepinephrine and dopamine. *Cerebral Cortex*, **17**: 2796–2804.

Patel V., Saxena S., Lund C., Thornicroft G., Baingana F., Bolton P., Chisholm D., Collins P.Y., Cooper J.L., Eaton J., Herrman H., Herzallah M.M., Huang Y., Jordans M.J.D., Kleinman A., Medina-Mora M.E., Morgan E., Niaz U., Omigbodun O., Prince M., Rahman A., Saraceno B., Sarkar B.K., De Silva M., Singh I., Stein D.J., Sunkel C., UnÜtzer J. (2018). The Lancet Commission on global mental health and sustainable development. *The Lancet*, **392**: 1553–1598.

Pekny M., and Nilsson M. (2005). Astrocyte activation and reactive gliosis. *Glia*, **50**: 427–434.

Pekny M., and Pekna M. (2014). Astrocyte reactivity and reactive astrogliosis: Costs and benefits. *Physiological Reviews*, **94**: 1077–1098.

Peng X., Luo Z., He S., Zhang L., and Li Y. (2021). Blood-brain barrier disruption by lipopolysaccharide and sepsis-associated encephalopathy. *Frontiers in Cellular and Infection Microbiology*, **11**: 768108.

Penkowa M., Giralt M., Lago N., Camats J., Carrasco J., Hernández J., Molinero A., Campbell I.L., and Hidalgo J. (2003). Astrocyte-targeted expression of IL-6 protects the CNS against a focal brain injury. *Experimental Neurology*, **181**: 130–148.

Percie du Sert N., Hurst V., Ahluwalia A., Alam S., Avey M.T., Baker M., Browne W.J., Clark A., Cuthill I.C., Dirnagl U., Emerson M., Garner P., Holgate S.T., Howells D.W., Karp N.A., Lazic S.E., Lidster K., MacCallum C.J., Macleod M., Pearl E.J., Petersen O.H., Rawle F., Reynolds P., Rooney K., Sena E.S., Silberberg S.D., Steckler T., and Würbel H. (2020). The ARRIVE guidelines 2.0: Updated guidelines for reporting animal research. *BMC Veterinary Research*, **4**: 100115.

Piotti P., Pierantoni L., Albertini M., and Pirrone F. (2023). Inflammation and behavior changes in dogs and cats. *Veterinary Clinics of North America: Small Animal Practice*, **54**: 1–16.

Pulgar V.M. (2019). Transcytosis to cross the blood brain barrier, new advancements and challenges. *Frontiers in Neuroscience*, **12**: 1019.

Qin D., Rizak J., Feng X., Yang S., Lü L., Pan L., Yin Y., and Hu X. (2016). Prolonged secretion of cortisol as a possible mechanism underlying stress and depressive behaviour. *Scientific Reports*, **6**: 30187.

Qin L., Wu X., Block M.L., Liu Y., Breese G.R., Hong J.S., Knapp D.J., and Crews F.T. (2007). Systemic LPS causes chronic neuroinflammation and progressive neurodegeneration. *Glia*, **55**: 453–462.

Qu D., Ye Z., Zhang W., Dai B., Chen G., Wang L., Shao X., Xiang A., Lu Z., and Shi J. (2022). Cyanidin chloride improves LPS-induced depression-like behavior in mice by ameliorating hippocampal inflammation and excitotoxicity. *ACS Chemical Neuroscience*, **13**: 3023–3033.

Rebois R.V., Maki K., Meeks J.A., Fishman P.H., Hébert T.E., and Northup J.K. (2012). D2-like dopamine and ß-adrenergic receptors form a signaling complex that integrates Gs- and Gi-mediated regulation of adenylyl cyclase. *Cellular Signalling*, **24**: 2051–2060.

Richfield E.K., Penney J.B., and Young A.B. (1989). Anatomical and affinity state comparisons between dopamine D_1 and D_2 receptors in the rat central nervous system. *Neuroscience*, **30**: 767–777.

Risher W.C., Ustunkaya T., Alvarado J.S., and Eroglu C. (2014). Rapid golgi analysis method for efficient and unbiased classification of dendritic spines. *PLoS ONE*, **9**: 107591.

Rodnight R.B., and Gottfried C. (2013). Morphological plasticity of rodent astroglia. *Journal of Neurochemistry*, **124**: 263–275.

Rodríguez-Arias M., Montagud-Romero S., Carrión A.M.G., Ferrer-Pérez C., Pérez-Villalba A., Marco E., López Gallardo M., Viveros M.P., and Miñarro J. (2018). Social stress during adolescence activates long-term microglia inflammation insult in reward processing nuclei. *PLoS ONE*, **13**: 0206421.

Roohi E., Jaafari N., and Hashemian F. (2021). On inflammatory hypothesis of depression: What is the role of IL-6 in the middle of the chaos? *Journal of Neuroinflammation*, **18**: 45.

Runge K., Cardoso C., and de Chevigny A. (2020). Dendritic spine plasticity: Function and mechanisms. *Frontiers in Synaptic Neuroscience*, **12**: 36.

Sancho L., Contreras M., and Allen N.J. (2021). Glia as sculptors of synaptic plasticity. *Neuroscience Research*, **167**: 17–29.

Santosa E.K., and Sun J.C. (2023). Cardinal features of immune memory in innate lymphocytes. *Nature Immunology*, **24**: 1803–1812.

Seeman P., and Grigoriadis D. (1987). Dopamine receptors in brain and periphery. *Neurochemistry International*, **10**: 1–25.

Sekio M., and Seki K. (2015). Lipopolysaccharide-induced depressive-like behavior is associated with α_1-adrenoceptor dependent downregulation of the membrane GluR1 subunit in the mouse medial prefrontal cortex and ventral tegmental area. *International Journal of Neuropsychopharmacology*, **18**: 5.

Sestakova N., Puzserova A., Kluknavsky M., and Bernatova I. (2013). Determination of motor activity and anxiety-related behaviour in rodents: Methodological aspects and role of nitric oxide. *Interdisciplinary Toxicology*, **6**: 126–135.

Sethi P., Virmani G., Gupta K., Thumu S.C.R., Ramanan N., and Marathe S. (2021). Automated morphometric analysis with SMorph software reveals plasticity induced by

antidepressant therapy in hippocampal astrocytes. *Journal of Cell Science*, **134**: 258430.

Shah A., Silverstein P.S., Singh D.P., and Kumar A. (2012). Involvement of metabotropic glutamate receptor 5, AKT/PI3K Signaling and NF-κB pathway in methamphetamine-mediated increase in IL-6 and IL-8 expression in astrocytes. *Journal of Neuroinflammation*, **9**: 52.

Shao Y., and Sutin J. (1992). Expression of adrenergic receptors in individual astrocytes and motor neurons isolated from the adult rat brain. *Glia*, **6**: 108–117.

Sharma N., Dhiman S., Bodh V., Sharma D., Sharma R., Sharma S., and Sharma B. (2021). Cognitive dysfunction in ulcerative colitis patients in remission and its comparison with patients with irritable bowel syndrome and healthy controls. *Indian Journal of Gastroenterology*, **40**: 169–175.

Shaulian E., and Karin M. (2001). AP-1 in cell proliferation and survival. *Oncogene*, **20**: 2390–2400.

Slota J.A., and Booth S.A. (2019). MicroRNAs in neuroinflammation: Implications in disease pathogenesis, biomarker discovery and therapeutic applications. *Non-Coding RNA*, **5**: 35.

Sofroniew M. V. (2009). Molecular dissection of reactive astrogliosis and glial scar formation. *Trends in Neurosciences*, **32**: 638–647.

Song C., and Wang H. (2011). Cytokines mediated inflammation and decreased neurogenesis in animal models of depression. *Progress in Neuro-Psychopharmacology and Biological Psychiatry*, **35**: 760–768.

Song J.J., Li H., Wang N., Zhou X.Y., Liu Y., Zhang Z., Feng Q., Chen Y.L., Liu D., Liang J., Ma X.Y., Wen X.R., and Fu Y.Y. (2022). Gastrodin ameliorates the lipopolysaccharide-induced neuroinflammation in mice by downregulating miR-107-3p. *Frontiers in Pharmacology*, **13**: 1044375.

Sordo L., and Gunn-Moore D.A. (2021). Cognitive dysfunction in cats: Update on neuropathological and behavioural changes plus clinical management. *Veterinary Record,* **188**: 3.

Stanasila L., Perez J.B., Vogel H., and Cotecchia S. (2003). Oligomerization of the α_{1a}- and α_{1b}-adrenergic receptor subtypes: Potential implications in receptor internalization. *Journal of Biological Chemistry*, **278**: 40239–40251.

Stein I.S., and Zito K. (2019). Dendritic spine elimination: Molecular mechanisms and implications. *Neuroscientist*, **25**: 27–47.

Stogsdill J.A., Ramirez J., Liu D., Kim Y.H., Baldwin K.T., Enustun E., Ejikeme T., Ji R.R., and Eroglu C. (2017). Astrocytic neuroligins control astrocyte morphogenesis and synaptogenesis. *Nature*, **551**: 192–197.

Strittmatter M., Grauer M., Isenberg E., Hamann G., Fischer C., Hoffmann K.H., Biaes F., and Schimrigk K. (1997). Cerebrospinal fluid neuropeptides and monoaminergic transmitters in patients with Trigeminal Neuralgia. *Headache: The Journal of Head and Face Pain*, **37**: 211–216.

Sun Y., Koyama Y., and Shimada S. (2022). Inflammation from peripheral organs to the brain: How does systemic inflammation cause neuroinflammation? *Frontiers in Aging Neuroscience*, **14**: 903455.

Tamura Y., Yamato M., and Kataoka Y. (2022). Animal models for neuroinflammation and potential treatment methods. *Frontiers in Neurology*, **13**: 890217.

Tavares G., Martins M., Correia J.S., Sardinha V.M., Guerra-Gomes S., Neves S.P. das, Marques F., Sousa N., and Oliveira J.F. (2017). Employing an open-source tool to assess astrocyte tridimensional structure. *Brain Structure and Function*, **222**: 1989–1999.

Vakharia K., and Hinson J.P. (2005). Lipopolysaccharide directly stimulates cortisol secretion by human adrenal cells by a cyclooxygenase-dependent mechanism. *Endocrinology*, **146**: 1398–1402.

Vargas-Caraveo A., Sayd A., Maus S.R., Caso J.R., Madrigal J.L.M., García-Bueno B., and Leza J.C. (2017). Lipopolysaccharide enters the rat brain by a lipoprotein-mediated transport mechanism in physiological conditions. *Scientific Reports*, **7**: 13113.

Wagner J.A. (1996). Is IL-6 both a cytokine and a neurotrophic factor? *Journal of Experimental Medicine*, **183**: 2417–2419.

Watts V.J., and Neve K.A. (1997). Activation of type II adenylate cyclase by D_2 and D_4 but not D_3 dopamine receptors. *Molecular Pharmacology*, **52**: 181–186.

Willis E.F., MacDonald K.P.A., Nguyen Q.H., Garrido A.L., Gillespie E.R., Harley S.B.R., Bartlett P.F., Schroder W.A., Yates A.G., Anthony D.C., Rose-John S., Ruitenberg M.J., and Vukovic J. (2020). Repopulating microglia promote brain repair in an IL-6-dependent manner. *Cell*, **180**: 833–846.

Woodburn S.C., Bollinger J.L., and Wohleb E.S. (2021). The semantics of microglia activation: Neuroinflammation, homeostasis, and stress. *Journal of Neuroinflammation*, **18**: 258.

Wouters E., Marín A.R., Dalton J.A.R., Giraldo J., and Stove C. (2019). Distinct dopamine D_2 receptor antagonists differentially impact D_2 receptor oligomerization. *International Journal of Molecular Sciences*, **20**: 1686.

Xu J., He J., Castleberry A.M., Balasubramanian S., Lau A.G., and Halls R.A. (2003). Heterodimerization of α_{2A}- and β_1-adrenergic receptors. *Journal of Biological Chemistry*, **278**: 10770–10777.

Yankelevitch-Yahav R., Franko M., Huly A., and Doron R. (2015). The forced swim test as a model of depressive-like behavior. *Journal of Visualized Experiments*, **97**: 52587.

Yin R., Zhang K., Li Y., Tang Z., Zheng R., Ma Y., Chen Z., Lei N., Xiong L., Guo P., Li G., and Xie Y. (2023). Lipopolysaccharide-induced depression-like model in mice: Meta-analysis and systematic evaluation. *Frontiers in Immunology*, **14**: 1181973.

Young K., and Morrison H. (2018). Quantifying microglia morphology from photomicrographs of immunohistochemistry prepared tissue using imageJ. *Journal of Visualized Experiments*, **136**: 57648.

Yu Z., Lin Y.T., and Chen J.C. (2021). Knockout of NPFFR2 prevents LPS-induced depressive-like responses in mice. *International Journal of Molecular Sciences*, **22**: 7611.

Yuan N., Chen Y., Xia Y., Dai J., and Liu C. (2019). Inflammation-related biomarkers in major psychiatric disorders: A cross-disorder assessment of reproducibility and specificity in 43 meta-analyses. *Translational Psychiatry*, **9**: 233.

Zhang P., Guo Z.F., Xu Y.M., Li Y.S., and Song J.G. (2016). N-Butylphthalide (NBP) ameliorated cerebral ischemia reperfusion-induced brain injury via HGF-regulated TLR4/NF-κB signaling pathway. *Biomedicine and Pharmacotherapy*, **83**: 658–666.

Zhang X., Kracht L., Lerario A.M., Dubbelaar M.L., Brouwer N., Wesseling E.M., Boddeke E.W.G.M., Eggen B.J.L., and Kooistra S.M. (2022). Epigenetic regulation of innate immune memory in microglia. *Journal of Neuroinflammation*, **19**: 111.

Zhang X., Zhou Z., Wang D., Li A., Yin Y., Gu X., Ding F., Zhen X., and Zhou J. (2009). Activation of phosphatidylinositol-linked D1-like receptor modulates FGF-2 expression in astrocytes via IP3-dependent Ca^{2+} signaling. *The Journal of Neuroscience*, **29**: 7766–7775.

Zhu J., Hu Z., Han X., Wang D., Jiang Q., Ding J., Xiao M., Wang C., Lu M., and Hu G. (2018). Dopamine D_2 receptor restricts astrocytic NLRP3 inflammasome activation via enhancing the interaction of ß-arrestin2 and NLRP3. *Cell Death & Differentiation*, **25**: 2037–2049.

Zorec R., Horvat A., Vardjan N., and Verkhratsky A. (2015). Memory formation shaped by astroglia. *Frontiers in Integrative Neuroscience*, **9**: 168809.